

Study of exclusive Upsilon (Υ) photo-production in ultra-peripheral pPb collisions at $\sqrt{s_{NN}} = 8.16$ TeV with the CMS experiment at the LHC

Submitted in partial fulfillment of the requirements
of the degree of

Doctor of Philosophy

by

Kousik Naskar
(Roll No. 154123004)

Supervisors:

Prof. Pradeep Sarin
Prof. Dipanwita Dutta



DEPARTMENT OF PHYSICS
INDIAN INSTITUTE OF TECHNOLOGY BOMBAY
2021

Dedicated to my beloved parents.

Thesis Approval

This thesis entitled **Study of exclusive Upsilon (Υ) photo-production in ultra-peripheral pPb collisions at $\sqrt{s_{NN}} = 8.16$ TeV with the CMS experiment at the LHC** by **Kousik Naskar** is approved for the degree of **Doctor of Philosophy**.

Examiners:

PROF. S. UMA SANKAR *S. UmaSankar*

PROF. PRASHANT MUKHERJEE *Prashant-*

PROF. D. MAITI

Chairperson:

[Signature] CHEMISTRY, IIT BOMBAY

Supervisor:

[Signature] **PRADEEP SARIN**

Date: **12/08/2022**

Place: **PHY. SEMINAR HAN**
202

Declaration

I declare that this written submission represents my ideas in my own words and where others ideas or words have been included, I have adequately cited and referenced the original sources. I also declare that I have adhered to all principles of academic honesty and integrity and have not misrepresented or fabricated or falsified any idea/data/fact/source in my submission. I understand that any violation of the above will be cause for disciplinary action by the Institute and can also evoke penal action from the sources which have thus not been properly cited or from whom proper permission has not been taken when needed.

Date: 17/08/2022

Kousik Naskar

Kousik Naskar

Roll No. 154123004

Abstract

The aim of this study is to measure exclusive photo-production of three resonant particles, $\Upsilon(1S)$, $\Upsilon(2S)$ and $\Upsilon(3S)$ mesons, in their $\mu^+\mu^-$ decay modes, in ultra-peripheral pPb collisions. We perform our study using data collected by the Compact Muon Solenoid (CMS) experiment at the Large Hadron Collider(LHC). It is advantageous to look for the dimuon decay channel of $\Upsilon(nS)$ as the CMS detector identifies and reconstructs muons very accurately.

Exclusive vector meson photo-production can probe the gluon distribution of nuclei as it is related to the slope parameter- b of the differential cross-section ($\frac{d\sigma}{dp_T^2} \propto e^{-bp_T^2}$) of this process. Therefore it provides information about the initial state of relativistic heavy-ion collisions. Recent comparisons of HERA and LHC data have been used to determine the gluon distribution function in the target proton, but this function is poorly known at low Bjorken- x .

In this thesis, we present estimation and exclusion of different background contributions such as QED and proton dissociation in the signal region ($\gamma + p \rightarrow \Upsilon(1S) + p$). We measure the slope of the squared transverse momentum (p_T^2)-dependent differential cross-section and determine the size of the production region. The $\Upsilon(1S)$ photo-production cross-section is measured, over the rapidity range $|y| < 2.2$, as a function of the photon-proton center-of-mass energy, $W_{\gamma p}$, which provides valuable information of the gluon distribution at small values of parton fractional momenta $x \approx 10^{-4} - 10^{-2}$.

To summarize, we compare our results to other measurements and theoretical predictions.

Contents

Abstract	i
List of Tables	vi
List of Figures	viii
1 Introduction	1
1.1 Why do we study elementary particles and their interactions?	1
1.2 The Standard Model	2
1.2.1 The $\Upsilon(1S,2S,3S)$	3
1.2.2 Standard Model interactions	4
1.2.3 A Brief Introduction to Quantum Field Theory	5
1.2.4 Quantum electrodynamics	5
1.2.5 Quantum Chromodynamics	7
1.2.6 Quark-Gluon Plasma (QGP)	9
1.2.7 Parton distribution function	13
1.2.8 Insufficiency of the Standard Model	13
1.3 Motivation for this study	15
1.4 Thesis outline	16
2 Ultra-peripheral collisions and photo-production	17
2.1 Ultra-peripheral collisions of heavy-ions	17
2.2 Vector meson photo-production	19
3 Experimental techniques of particle detection	23
3.1 Particle interactions with matter	23

3.1.1	Ionization energy losses	23
3.1.2	Bremsstrahlung energy loss	26
3.1.3	Čerenkov radiation	28
3.2	Particle detectors	30
3.2.1	Gas detectors	30
3.2.2	Semiconductor detectors	32
3.2.3	Scintillation detectors	33
3.2.4	Calorimeters	35
3.3	The Large Hadron Collider	35
3.4	LHC Luminosity	38
3.5	The Compact Muon Solenoid	39
3.5.1	CMS Coordinate System	40
3.5.2	CMS Tracker System	41
3.5.3	Electromagnetic Calorimeter	42
3.5.4	Hadronic Calorimeter	43
3.5.5	Magnet	45
3.5.6	Muon System	46
3.5.7	CASTOR	48
3.5.8	Trigger	49
4	CMS data and MC simulation	50
4.1	Dataset	50
4.2	Monte Carlo Samples	51
5	Event Selection	59
5.1	Trigger	59
5.2	Muon selection	60
5.3	Selection of exclusive Upsilon candidates	61
5.4	Noise study	62
6	Muon efficiency using Tag and Probe method	68
6.1	Trigger efficiency	70
6.2	Muon ID efficiency	71

6.3	Tracking efficiency	73
6.4	Acceptance and efficiency	76
7	Invariant mass fitting	79
8	Background estimation and extraction of cross-sections	87
8.1	QED background	87
8.2	γ Pb background	90
8.3	Non-exclusive background	90
8.4	Feed-down background	93
8.5	Background subtraction	94
8.6	Extraction of cross-sections	94
9	Systematic uncertainties	97
10	Results	100
10.1	Differential cross-section as a function of $ t $ and y	100
10.2	Cross-section as a function of $W_{\gamma p}$	102
11	Summary	106
.1	Appendix 1	108
Acknowledgments		121

List of Tables

1.1	The strength of different forces, name, and mass of force carrier is listed in this table [6].	4
3.1	Summary of variables used in equation 3.1.	25
4.1	Cross-sections for Upsilon photo-production in pPb collisions at $\sqrt{s} = 8.16$ TeV from STARLIGHT.	52
5.1	Statistics after each event selection cut for pPb and Ppb collisions at $\sqrt{s} = 8.16$ TeV	64
5.2	Thresholds in each sub-detector.	65
6.1	Acceptance \times Efficiency of $\Upsilon(1S)$ from STARLIGHT MC.	78
7.1	Summary of different fitting of invariant mass distribution of muon pairs from STARLIGHT MC.	85
7.2	Summary of different fitting of invariant mass distribution of data.	86
8.1	QED cross-section from Data and MC in the dimuon rapidity region $ y < 2.2$. .	90
8.2	Proton-dissociation contribution in signal region	91
8.3	Number of events in $p_T^2(\mu^+\mu^-)$ bins for data and all backgrounds	94
8.4	Number of events in rapidity bins for data and all backgrounds	94
9.1	Relative systematic uncertainties in the measurements of $\mathcal{B}_{\Upsilon(1S) \rightarrow \mu^+ \mu^-} d\sigma_{\Upsilon(1S)} / d t $, the exponential b slope of the $ t $ spectrum, $d\sigma_{\Upsilon(1S)} / dy$, and $\sigma_{\gamma p \rightarrow \Upsilon(1S)p}$. Individual contributions, as well as total systematic uncertainties added in quadrature, are presented. For the $ t $ - and y -differential cross-sections, the values averaged over all bins are shown.	99

9.2	Relative systematic uncertainties in the measurements of $\mathcal{B}_{\Upsilon(1S) \rightarrow \mu^+ \mu^-} d\sigma_{\Upsilon(1S)} / d t $, the exponential b slope of the $ t $ spectrum, $d\sigma_{\Upsilon(1S)} / dy$, and $\sigma_{\gamma p \rightarrow \Upsilon(1S)p}$. Minimum and maximum systematic error per source	99
10.1	Differential exclusive $\Upsilon(1S) \rightarrow \mu^+ \mu^-$ photo-production cross-sections in four $ t $ and y bins. The first and second uncertainties correspond to statistical and systematic components, respectively.	102
10.2	Values of the $\Upsilon(1S)$ photo-production cross-section in four rapidity y bins, corresponding to four photon-proton $W_{\gamma p}$ centre-of-mass energy ranges (with central W_0 value obtained following [88]), in pPb collisions at $\sqrt{s_{\text{NN}}} = 8.16 \text{ TeV}$. The symbols $N_{\Upsilon(1S)}^{\text{back-sub}}$, and $N_{\Upsilon(1S)}^{\text{exc}}$ represent the numbers of $N_{\Upsilon(1S)}$ candidates after background subtraction, and Acceptance \times Efficiency corrected factor, respectively; $N_{\Upsilon(1S)}$ is the extracted number of $\Upsilon(1S)$ mesons, and Φ is the theoretical effective photon flux (see text). The first (second, if given) uncertainty quoted corresponds to the statistical (systematic) component.	104

List of Figures

1.1	The elementary particles in the standard model of particle physics. The fermions are shown on the left, with the quarks on top and leptons below. The gauge and Higgs bosons are shown on the right [1].	2
1.2	QED coupling strength α as a function of four-momentum transfer Q^2 [11].	7
1.3	QCD coupling constant $\alpha_s(Q)$ as a function of energy scale Q [12].	9
1.4	The QCD phase diagram [14].	10
1.5	Measurements of the nuclear modification factor (R_{AA}) in central heavy-ion collisions at three different $\sqrt{S_{NN}}$ energies, as a function of p_T , for charged hadrons (h^\pm), neutral pions (π^0), and charged particles. Also, a comparison with several theoretical predictions is shown here [15].	11
1.6	Elliptic flow (v_2) of average D mesons as a function of p_T in Pb-Pb collisions at center-of-mass energy 2.76 TeV [17].	12
1.7	Parton distribution function in proton from HERA data and theoretical prediction [19].	14
2.1	Schematic diagram of electric field and photon radiation from relativistic heavy-ions.	18
2.2	Diagrams representing (a) exclusive Υ photo-production, (b) exclusive dimuon QED continuum production, and (c) proton dissociation background in pPb collisions.	20
2.3	Event display of a typical exclusive Υ photo-production in pPb collisions.	21
3.1	Mean energy loss $-\langle \frac{dE}{dx} \rangle$ for positive muons in copper as a function of $\beta\gamma$ (Particle Data Group, 2018).	24

3.2	Mean ionization energy loss $-\langle \frac{dE}{dx} \rangle$ curves for a singly charged particle in various materials as a function of $\beta\gamma$ (Particle Data Group, 2018)	25
3.3	$-dE/dx$ curves as a function of different projectiles (electrons, muons, protons, kaons, and pions) momentum [fig courtesy BaBar experiment at SLAC]	26
3.4	The bremsstrahlung process $e^- + N(Z,A) \rightarrow e^- + \gamma + N(Z,A)$. N is a nucleus of charge $+Ze$ [6]	27
3.5	Collision-ionization energy loss, radiation energy loss, and total energy loss for an electron in copper [53].	28
3.6	The geometry of Čerenkov radiation emitted by a charged particle travelling with velocity v greater than the speed of light (c/n) in the dispersive medium [6].	29
3.7	A schematic diagram of a gas-filled detector showing how gaseous ionization detectors work [55].	30
3.8	Number of collected ions as a function of voltage with different characteristic modes of operation of a single wire gas chamber [56].	31
3.9	Cylindrical ionization detector [53].	31
3.10	Schematic diagram of silicon tracking detector [6].	33
3.11	Schematic diagram of a scintillator with photomultiplier tube (PMT) [60].	34
3.12	A schematic view of the CERN accelerator complex.	36
3.13	The structure of the LHC layout.	37
3.14	The cumulative delivered and recorded luminosity versus day for pPb, 2016 run.	39
3.15	A schematic view of the CMS detector [63].	40
3.16	A schematic view of the CMS coordinate system [63, 64].	40
3.17	A schematic overview of the CMS tracker system.	41
3.18	A view of ECAL detector in CMS and η coverage of ECAL components.	43
3.19	ECAL energy resolution (σ/E) as a function of the electron energy [65].	44
3.20	Longitudinal view of the CMS HCAL detector [65].	44
3.21	An artistic view of CMS superconducting magnet having 5 modules [65].	46
3.22	A schematic view of a quadrant of muon system [66].	47
3.23	A schematic view of a drift tube [65].	47
3.24	View of the CASTOR calorimeter [67].	48

4.1	Generated and reconstructed distributions of muon p_T^μ for $\gamma p \rightarrow \Upsilon(nS)p$ (upper panel), $\gamma Pb \rightarrow \Upsilon(nS)Pb$ (middle panel), signal: sum of $\gamma p \rightarrow \Upsilon(nS)p$ and $\gamma Pb \rightarrow \Upsilon(nS)Pb$ (left figure of lower panel), QED: $\gamma\gamma \rightarrow \mu^+\mu^-$ (middle figure of lower panel) and sum of signal+QED (right figure of lower panel) processes within invariant mass range $8 < m_{\mu^+\mu^-} < 12$ GeV. Red and blue dots represent generated and reconstructed distributions, respectively.	53
4.2	Generated and reconstructed distributions of muon η_μ for $\gamma p \rightarrow \Upsilon(nS)p$ (upper panel), $\gamma Pb \rightarrow \Upsilon(nS)Pb$ (middle panel), signal: sum of $\gamma p \rightarrow \Upsilon(nS)p$ and $\gamma Pb \rightarrow \Upsilon(nS)Pb$ (left figure of lower panel), QED: $\gamma\gamma \rightarrow \mu^+\mu^-$ (middle figure of lower panel) and sum of signal+QED (right figure of lower panel) processes within invariant mass range $8 < m_{\mu^+\mu^-} < 12$ GeV. Red and blue dots represent generated and reconstructed distributions, respectively.	54
4.3	Generated and reconstructed distributions of muon ϕ_μ for $\gamma p \rightarrow \Upsilon(nS)p$ (upper panel), $\gamma Pb \rightarrow \Upsilon(nS)Pb$ (middle panel), signal: sum of $\gamma p \rightarrow \Upsilon(nS)p$ and $\gamma Pb \rightarrow \Upsilon(nS)Pb$ (left figure of lower panel), QED: $\gamma\gamma \rightarrow \mu^+\mu^-$ (middle figure of lower panel) and sum of signal+QED (right figure of lower panel) processes within invariant mass range $8 < m_{\mu^+\mu^-} < 12$ GeV. Red and blue dots represent generated and reconstructed distributions, respectively.	55
4.4	Generated and reconstructed distributions of muon pair $p_T(\mu^+\mu^-)$ for $\gamma p \rightarrow \Upsilon(nS)p$ (upper panel), $\gamma Pb \rightarrow \Upsilon(nS)Pb$ (middle panel), signal: sum of $\gamma p \rightarrow \Upsilon(nS)p$ and $\gamma Pb \rightarrow \Upsilon(nS)Pb$ (left figure of lower panel), QED: $\gamma\gamma \rightarrow \mu^+\mu^-$ (middle figure of lower panel) and sum of signal+QED (right figure of lower panel) processes within invariant mass range $8 < m_{\mu^+\mu^-} < 12$ GeV. Red and blue dots represent generated and reconstructed distributions, respectively.	56
4.5	Generated and reconstructed distributions of muon pair rapidity for $\gamma p \rightarrow \Upsilon(nS)p$ (upper panel), $\gamma Pb \rightarrow \Upsilon(nS)Pb$ (middle panel), signal: sum of $\gamma p \rightarrow \Upsilon(nS)p$ and $\gamma Pb \rightarrow \Upsilon(nS)Pb$ (left figure of lower panel), QED: $\gamma\gamma \rightarrow \mu^+\mu^-$ (middle figure of lower panel) and sum of signal+QED (right figure of lower panel) processes within invariant mass range $8 < m_{\mu^+\mu^-} < 12$ GeV. Red and blue dots represent generated and reconstructed distributions, respectively.	57

4.6	Reconstructed distributions of muon pair invariant mass for for $\gamma p \rightarrow \Upsilon(nS)p$ (upper panel), $\gamma Pb \rightarrow \Upsilon(nS)Pb$ (middle panel), signal: sum of $\gamma p \rightarrow \Upsilon(nS)p$ and $\gamma Pb \rightarrow \Upsilon(nS)Pb$ (left figure of lower panel), QED: $\gamma\gamma \rightarrow \mu^+\mu^-$ (middle figure of lower panel) and sum of signal+QED (right figure of lower panel) processes within invariant mass range $8 < m_{\mu^+\mu^-} < 12$ GeV. Blue dots represent reconstructed distributions.	58
5.1	Extra tower HF plus and HF minus energy distributions for pPb and Pbp run.	62
5.2	HB and HE leading tower energy distributions for Data and MC (STARLIGHT).	63
5.3	EM barrel and EM endcap leading tower energy distributions for Data and MC (STARLIGHT).	63
5.4	(Upper panel) Leading electromagnetic energy distribution in EB (left) and EE $^\pm$ (right), (middle panel) leading hadronic energy in HB (left) and HE $^\pm$ (right), (lower panel) leading energy distribution in HF plus (left) and HF minus (right) for pPb collisions at $\sqrt{s} = 8.16$ TeV Emptybx data. Thresholds are shown with vertical lines.	66
5.5	(left) CASTOR rechit energy distributions for Emptybx and ZeroBias data. (middle) CASTOR rechit max energy distributions for Emptybx and ZeroBias data. (right) CASTOR leading energy distributions for Emptybx and ZeroBias data. The threshold is shown with a vertical line.	67
6.1	Trigger efficiency as a function of muon p_T and η estimated with the Tag and Probe method.	70
6.2	Tag-and-probe mass fit for trigger efficiency for data.	71
6.3	Tag-and-probe mass fit for trigger efficiency for MC.	72
6.4	Trigger efficiency for MC as a function of muon p_T^μ and η^μ estimated using Tag and Probe method.	72
6.5	Muon ID efficiency as a function of muon p_T and η estimated with the Tag and Probe method.	73
6.6	Tag-and-probe mass fit for Muon ID efficiency for data.	74
6.7	Tag-and-probe mass fit for Muon ID efficiency for MC.	75
6.8	Tracker Muon efficiency as a function of muon p_T and η estimated with the Tag and Probe method.	75

6.9	Tag-and-probe mass fit for Tracker Muon efficiency for data.	76
6.10	Tag-and-probe mass fit for Tracker Muon efficiency for MC.	77
6.11	Acceptance (left), Efficiency (middle) and Acceptance \times Efficiency (right) distributions with $\Upsilon(1S)$ p_T^2 from STARLIGHT MC sample.	77
6.12	Acceptance (left), Efficiency (middle) and Acceptance \times Efficiency (right) distributions with $\Upsilon(1S)$ y from STARLIGHT MC sample.	78
7.1	Invariant mass distribution of exclusive muon pair candidates in four asymmetric rapidity bins that pass all the selection criteria from STARLIGHT MC, fitted to a Err \times Exp function for the two-photon QED continuum (blue dashed curve) plus three Gaussian distributions corresponding to the $\Upsilon(1S)$, $\Upsilon(2S)$, and $\Upsilon(3S)$ mesons (red dotted curves). Invariant mass fitting is done in the following 4-rapidity range: (a) $-2.2 < y_{\mu^+\mu^-} < -1.23$ (upper left plot), (b) $-1.23 < y_{\mu^+\mu^-} < -0.18$ (upper right plot), (c) $-0.18 < y_{\mu^+\mu^-} < 0.76$ (lower left plot), and (d) $0.76 < y_{\mu^+\mu^-} < 2.2$ (lower right plot). Details are given in the Table 7.1.	80
7.2	Invariant mass distribution of exclusive muon pair candidates in the rapidity interval $ y_{\mu^+\mu^-} < 2.2$ that pass all the selection criteria from STARLIGHT MC, fitted to an Err \times Exp function for the two-photon QED continuum (blue dashed curve) plus three Gaussian distributions corresponding to the $\Upsilon(1S)$, $\Upsilon(2S)$, and $\Upsilon(3S)$ mesons (red dotted curves). Details are given in Table 7.1.	82
7.3	Invariant mass distribution of exclusive muon pair candidates of STARLIGHT MC in four asymmetric $p_T^2(\mu^+\mu^-)$ bins that pass all the selection criteria, fitted to a Err \times Exp function for the two-photon QED continuum (blue dashed curve) plus three Gaussian distributions corresponding to the $\Upsilon(1S)$, $\Upsilon(2S)$, and $\Upsilon(3S)$ mesons (red dotted curves). Invariant mass fitting is done in the following 4- p_T^2 range: (a) $0 < p_T^2(\mu^+\mu^-) < 0.09$ (upper left plot), (b) $0.09 < p_T^2(\mu^+\mu^-) < 0.19$ (upper right plot), (c) $0.19 < p_T^2(\mu^+\mu^-) < 0.49$ (lower left plot), and (d) $0.49 < p_T^2(\mu^+\mu^-) < 1.0$ (lower right plot). The details are given in Table 7.1.	82

7.4	Invariant mass distribution of exclusive muon pair candidates of data in four asymmetric rapidity bins that pass all the selection criteria, fitted to a Err \times Exp function for the two-photon QED continuum (blue dashed curve) plus three Gaussian distributions corresponding to the $\Upsilon(1S)$, $\Upsilon(2S)$, and $\Upsilon(3S)$ mesons (red dotted curves). Invariant mass fitting is done in the following 4-rapidity range: (a) $-2.2 < y_{\mu^+\mu^-} < -1.23$ (upper left plot), (b) $-1.23 < y_{\mu^+\mu^-} < -0.18$ (upper right plot), (c) $-0.18 < y_{\mu^+\mu^-} < 0.76$ (lower left plot), and (d) $0.76 < y_{\mu^+\mu^-} < 2.2$ (lower right plot). The details are given in Table 7.2.	83
7.5	Invariant mass distribution of exclusive muon pair candidates of data in the rapidity interval $ y_{\mu^+\mu^-} < 2.2$ that pass all the selection criteria, fitted to an Err \times Exp function for the two-photon QED continuum (blue dashed curve) plus three Gaussian distributions corresponding to the $\Upsilon(1S)$, $\Upsilon(2S)$, and $\Upsilon(3S)$ mesons (red dotted curves). The details are given in Table 7.2.	83
7.6	Invariant mass distribution of exclusive muon pair candidates of data in four asymmetric $p_T^2(\mu^+\mu^-)$ bins that pass all the selection criteria, fitted to a linear function for the two-photon QED continuum (blue dashed curve) plus three Gaussian distributions corresponding to the $\Upsilon(1S)$, $\Upsilon(2S)$, and $\Upsilon(3S)$ mesons (red dotted curves). Invariant mass fitting is done in the following 4- p_T^2 range: (a) $0 < p_T^2(\mu^+\mu^-) < 0.09$ (upper left plot), (b) $0.09 < p_T^2(\mu^+\mu^-) < 0.19$ (upper right plot), (c) $0.19 < p_T^2(\mu^+\mu^-) < 0.49$ (lower left plot), and (d) $0.49 < p_T^2(\mu^+\mu^-) < 1.0$ (lower right plot). The details are given in Table 7.2.	84
8.1	Invariant mass distribution of data and MC in the sideband region ($8 < m_{\mu^+\mu^-} < 9$ GeV and $11 < m_{\mu^+\mu^-} < 20$ GeV) and $p_T(\mu^+\mu^-) < 0.15$ GeV where data is dominated by QED.	88
8.2	Acoplanarity distribution of dimuons for pPb added with the PbP run flipped leading to integrated luminosity of 173.4 nb^{-1} for the sideband region, $11 < M_{\mu^+\mu^-} < 20$ GeV. Data is compared with the simulated sample from STARLIGHT considering QED $\gamma\gamma \rightarrow \mu^+\mu^-$	89
8.3	Simultaneous fitting of proton-dissociation and inclusive background template within the rapidity range $ y_{\mu^+\mu^-} < 2.2$ using TFraction fitter [83] function. Here first 4- $p_T(\mu^+\mu^-)$ bins are chosen corresponding to the bins used for the signal cross-section extraction	91

8.4 Simultaneous fitting of proton-dissociation and inclusive background template using TFraction fitter [83] function. Fitting is done in the following 4-rapidity range: (a) $-2.2 < y_{\mu^+\mu^-} < -1.23$ (upper left plot),(b) $-1.23 < y_{\mu^+\mu^-} < -0.18$ (upper right plot), $-0.18 < y_{\mu^+\mu^-} < 0.76$ (lower left plot), $0.76 < y_{\mu^+\mu^-} < 2.2$ (lower right plot)	92
8.5 Input distribution of signal Υ (2S) from STARLIGHT MC, which are being decayed with PYTHIA as $\Upsilon(2S) \rightarrow \Upsilon(1S) + X$ ($\pi^+\pi^-$ or $\pi^0\pi^0$)	93
10.1 Differential $\Upsilon(1S) \rightarrow \mu^+\mu^-$ photo-production cross-section as a function of $ t $ measured in pPb collisions at $\sqrt{s_{NN}} = 8.16$ TeV. In this plot, the data points are placed along the abscissa following the prescription of [88], and the solid line is an exponential fit of the form $e^{-b t }$.The vertical bars represent the statistical and systematic uncertainties added in quadrature and the boxes represent the systematic uncertainties.	101
10.2 Differential $\Upsilon(1S)$ photo-production cross-section as a function of rapidity measured in pPb collisions at $\sqrt{s_{NN}} = 8.16$ TeV in the dimuon rapidity region $ y < 2.2$, compared to various theoretical predictions [29, 34–38]. The horizontal bars are plotted to indicate the width of each y bin. The vertical bars represent the statistical and systematic uncertainties added in quadrature and the boxes represent the systematic uncertainties.	103
10.3 Cross-section for exclusive $\Upsilon(1S)$ photo-production, $\gamma p \rightarrow \Upsilon(1S)p$, as a function of photon-proton centre-of-mass energy, $W_{\gamma p}$, compared to previous HERA [39–41] and LHCb [44] data as well as to various theoretical predictions [29, 34–38]. The vertical bars represent the statistical and systematic uncertainties added in quadrature and the boxes represent the systematic uncertainties.	105

1	Differential cross-sections of $\Upsilon(1S)$ as a function of $ t $ and y are shown in the left and the middle figure, respectively. The right figure shows the total cross-section of $\Upsilon(1S)$ as a function of $W_{\gamma P}$. The upper panel shows the cross-section corresponding to the +30% change of the parameters b and δ of the simulated STARLIGHT spectra. Similarly, the lower panel shows the cross-section corresponding to the -30% change of the parameters b and δ of the simulated STARLIGHT spectra. These plots are made to estimate systematic contribution corresponding to the model dependence of the product of the detector acceptance and efficiency.	108
2	Differential cross-sections of $\Upsilon(1S)$ as a function of $ t $ and y are shown in the left and the middle figure, respectively. The right figure shows the total cross-section of $\Upsilon(1S)$ as a function of $W_{\gamma P}$. The upper panel shows the cross-section corresponding to the +10% change of the HF threshold. Similarly, the lower panel shows the cross-section corresponding to the -10% change of the HF threshold. These plots are made to estimate systematic contribution corresponding to non-exclusive data driven template.	109
3	Differential cross-sections of $\Upsilon(1S)$ as a function of $ t $ and y are shown in the left and the middle figure, respectively. The right figure shows the total cross-section of $\Upsilon(1S)$ as a function of $W_{\gamma P}$. The upper panel shows the cross-section corresponding to the +3.5% change of luminosity. Similarly, the lower panel shows the cross-section corresponding to the -3.5% change of luminosity. These plots are made to estimate systematic contributions corresponding to the luminosity.	110
4	A differential cross-section of $\Upsilon(1S)$ as a function of y is shown left figure. The right figure shows the total cross-section of $\Upsilon(1S)$ as a function of $W_{\gamma P}$. These plots are made to estimate systematic contribution corresponding to the feed-down.	110
5	The differential cross-section of $\Upsilon(1S)$ as a function of y is shown in the left figure. The right figure shows the total cross-section of $\Upsilon(1S)$ as a function of $W_{\gamma P}$. The upper panel shows the cross-section corresponding to the +0.05% change of the BR fraction taken from PDG. Similarly, the lower panel shows the cross-section corresponding to the -0.05% change of the BR fraction. . . .	111

- 6 These figures show the total cross-section of $\Upsilon(1S)$ as a function of $W_{\gamma p}$. The left figure shows the cross-section corresponding to the +5% change of the lead ion radius in the STARLIGHT MC sample. Similarly, the right figure shows the cross-section corresponding to the -5% change of the lead ion radius. 111

Chapter 1

Introduction

This chapter introduces the Standard Model (SM) of particle physics, which describes the elementary particles and their interactions. Some limitations of the Standard Model are discussed.

1.1 Why do we study elementary particles and their interactions?

What are the fundamental building blocks of the visible universe? After hunting for many centuries, we found that we are made up of atoms. Protons, electrons, and neutrons form the substructure of an atom. While the electron is by and large believed to be elementary, there is also a substructure of proton and neutron. They are composed of quarks and gluons. We are curious to know the fundamental physics behind the many physical phenomena/observations. Some of the questions are mentioned below.

How are the protons confined in a small radius atom? What are the fundamental forces that exist in the universe? What was the scenario in the early universe? Is there any golden equation

to rule the universe? Are there a finite number of fundamental particles?

Many of the above questions are addressed by the Standard Model (SM) of particle physics. There is still much room left to understand nature by searching elementary particle physics and their interaction.

1.2 The Standard Model

The Standard Model is a quantum field theory that describes all currently observed elementary particles and their interactions. This theory can explain three interactions: electromagnetic, weak, and strong interaction. The form of interaction originated from the concept of gauge invariance that preserves local symmetries. The symmetry group of the SM is $SU(3)_C \times SU(2)_L \times U(1)_Y$. Where the indices represent the color charge C, the left-handedness L and Y denotes the hypercharge.

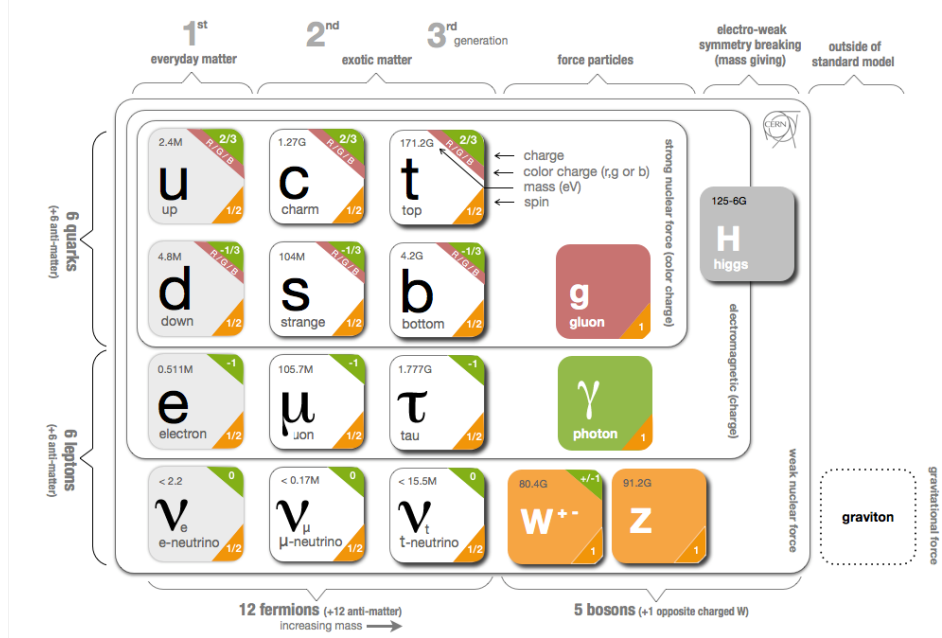


Figure 1.1: The elementary particles in the standard model of particle physics.

The fermions are shown on the left, with the quarks on top and leptons below.

The gauge and Higgs bosons are shown on the right [1].

The Standard Model represents a model of two types of particles: fermions that have half-integer spin and bosons with integer spin. The particle content of the SM with charge, mass, spin, and generation is shown in Figure 1.1. The fermions are quarks and leptons. There are 12 fermions, which are categorized into three generations. All these fermions have the same quantum numbers but they have different masses and different charges. Among them, 3rd generation fermions have the highest mass. In the SM, all fermions are the fundamental building blocks of matter. All these fermions can interact with each other. These interactions can be electromagnetic, weak, or strong interactions - their dynamics are cast into quantum field theories and form the core of the SM. In nature, quarks are not freely available and the reason is associated with QCD coupling (discussed in section 1.2.5). Hadrons are made of quarks and divided into two categories: baryons and mesons. Baryons consist of three quarks, for example, the proton(=uud) and neutron(=udd). A meson is a bound state of a quark + anti-quark.

Since each quark has spin $\frac{1}{2}$, a quark + anti-quark bound state can have a total spin 0, +1 or -1. Spin-0 bound states with even parity like the $K_0^*(1430)$ are called scalar mesons, while spin-0 bound states with odd parity are called pseudo scalar mesons. Among these, the $\pi^{0,+,-}$ is the most well-studied particle, perhaps because it was the earliest proposed particle for nuclear interactions in the Yukawa theory of particle interactions [2].

Mesons with spin-1 and odd parity are called vector mesons (those with even parity are called pseudo vector mesons). The terms scalar, vector, and tensor (spin 2) come from the underlying SU(3) group symmetry of the quark model first worked out by Gell-Mann [3] and Zweig [4].

The spectroscopy of quark bound states forms the foundational core of the Standard Model - it can accommodate all the known mesons and baryons and has predictive power guiding experiments to the discovery of higher mass bound states.

1.2.1 The $\Upsilon(1S,2S,3S)$

In this thesis, my work focuses on the Υ vector meson. This is a short-lived bound state of a bottom and anti-bottom ($b\bar{b}$) quark. It was discovered in 1977 by the E288 experiment team at Fermilab [5]. The $\Upsilon(2S)$ and $\Upsilon(3S)$ are higher energy or mass states of the $\Upsilon(1S)$. The masses

of $\Upsilon(1S)$, $\Upsilon(2S)$, and $\Upsilon(3S)$ are 9.46 GeV, 10.02 GeV, and 10.36 GeV, respectively ((Particle Data Group, 2018)) with a lifetime $\sim 10^{-20}$ s. It has the same quantum numbers as the photon $J^{PC} = 1^{--}$. Therefore, it is well suited to probe the structure of the proton when the partons in a proton interact electromagnetically with an external field. Under certain conditions, for example in the vicinity of a nucleus during a p-nucleus (pA) collision, many photons are exchanged and some will lead to the exclusive production of Υ . By “exclusive” production we mean that the proton and the nucleus remain intact - just the exchanged photons produce an Υ . We do not include cases where the proton disintegrates as part of the interaction leading to other $q\bar{q}$ fragments overlapping with the exclusive Υ we are looking for. The main task of this thesis is to isolate and study such interactions where photo-production of Υ occurs in a pA collision. The dominant decay modes of $\Upsilon(1S)$ are $\tau^+\tau^-$, e^+e^- and $\mu^+\mu^-$. Since it decays to $\mu^+\mu^-$, it is ideally suited for study in CMS experiment which is optimized for tracking muons.

1.2.2 Standard Model interactions

The Standard model suggests that there should be a force carrier associated with each interaction. The force carrier and the strength of the different types of interactions are given below.

Table 1.1: The strength of different forces, name, and mass of force carrier is listed in this table [6].

Force	Strength	force carrier	Spin	Mass/GeV
Strong	1	Gluon g	1	0
Electromagnetism	10^{-3}	Photon γ	1	0
weak	10^{-8}	W Boson W^\pm	1	80.4
	10^{-8}	Z Boson Z	1	91.2
Gravity	10^{-37}	Graviton G (not observed)	2	0

How does a particle acquire mass? To address this question, theorists Robert Brout, Francois Englert and Peter Higgs introduced the electroweak symmetry breaking mechanism in SM.

It's also known as the Brout-Englert-Higgs mechanism [7, 8], which explains that W and Z bosons acquire mass due to interaction with the Higgs field. Like all other fundamental fields, the Higgs field is associated with a particle called the Higgs boson. The recent discovery of the Higgs boson [9, 10] is a benchmark in the history of particle physics.

1.2.3 A Brief Introduction to Quantum Field Theory

In a nutshell, quantum field theory (QFT) is the extension of quantum mechanics to describe a complete picture of the physical world. More profoundly, QFT is the theoretical and mathematical framework to describe elementary particles and their interactions as quantized excitations of Lorentz invariant objects in the whole space-time known as quantum fields. A more detailed description of SM particle interaction in terms of QFT is given below. In this section, mathematical expressions are simplified by choosing $\hbar = 1$ and $c = 1$.

1.2.4 Quantum electrodynamics

Quantum electrodynamics (QED) is the relativistic quantum version of Maxwell's theory of classical electrodynamics. QED addresses the motion of a fermion field like the motion of an electron and the interaction of a fermion with a photon which is the mediator of electromagnetic interactions. In 1926, the wave equation of electron was first described by the Schrödinger equation at a non-relativistic scale. In 1928, Dirac introduced the relativistic motion of a free spin-half particle and given by Dirac Lagrangian:

$$\mathcal{L}_{Dirac} = \bar{\Psi}(i\gamma^\mu \partial_\mu - m)\Psi. \quad (1.1)$$

The Lagrangian is invariant under the U(1) global symmetry transformation $\Psi \rightarrow e^{i\theta}\Psi$. However, the Dirac equation 1.1 is not invariant under a local gauge transformation since the 2nd term in Eq. 1.2

$$\partial_\mu \Psi \rightarrow \partial_\mu(e^{i\theta(x)}\Psi) = e^{i\theta(x)}\partial_\mu\Psi + i\partial_\mu\theta(x)e^{i\theta(x)}\Psi \quad (1.2)$$

is non-zero. In order to maintain the invariance of Eq. 1.1, we need to consider an interaction term between a spin- $\frac{1}{2}$ field and a spin-1 field in the form of:

$$\mathcal{L}_{EM-int} = gA_\mu\bar{\Psi}\gamma^\mu\Psi, \quad (1.3)$$

where g is coupling constant and A_μ is covariant four-potential of the electromagnetic field (photon field) which transform as $A_\mu \rightarrow A'_\mu = A_\mu + \partial_\mu\theta(x)$. The kinetic term of photon is given by Maxwell Lagrangian:

$$\mathcal{L}_{Maxwell} = -\frac{1}{4}F_{\mu\nu}F^{\mu\nu}, \quad (1.4)$$

where $F_{\mu\nu}$ ($F_{\mu\nu} = \partial_\mu A_\nu - \partial_\nu A_\mu$) is field strength tensor which is invariant under the local gauge transformation. So, the QED Lagrangian density is given by

$$\begin{aligned} \mathcal{L}_{QED} &= \mathcal{L}_{Dirac} + \mathcal{L}_{EM-int} + \mathcal{L}_{Maxwell} \\ &= \bar{\Psi}(i\gamma^\mu\partial_\mu - m)\Psi + gA_\mu\bar{\Psi}\gamma^\mu\Psi - \frac{1}{4}F_{\mu\nu}F^{\mu\nu} \\ &= \bar{\Psi}(i\gamma^\mu D_\mu - m)\Psi - \frac{1}{4}F_{\mu\nu}F^{\mu\nu}, \end{aligned} \quad (1.5)$$

where D_μ is covariant derivative ($D_\mu = \partial_\mu - igA_\mu$). The QED coupling strength is constant ($\alpha_{em} \sim \frac{1}{137}$) at low energy scale. The cross-section for the higher-order QED process is proportional to $(\alpha_{em})^n$, where n is the number of vertices. Hence the cross-section of the higher-order Feynman loop diagram is very small. Fig. 1.2 shows that α_{em} increases with the increase of four-momentum transfer (Q^2). In leading order, it can be written as

$$\alpha_{QED}(Q^2) = \frac{\alpha_{em}}{1 - \frac{\alpha_{em}}{3\pi}\ln(\frac{Q^2}{m^2})}, \quad (1.6)$$

where m is the electron mass.

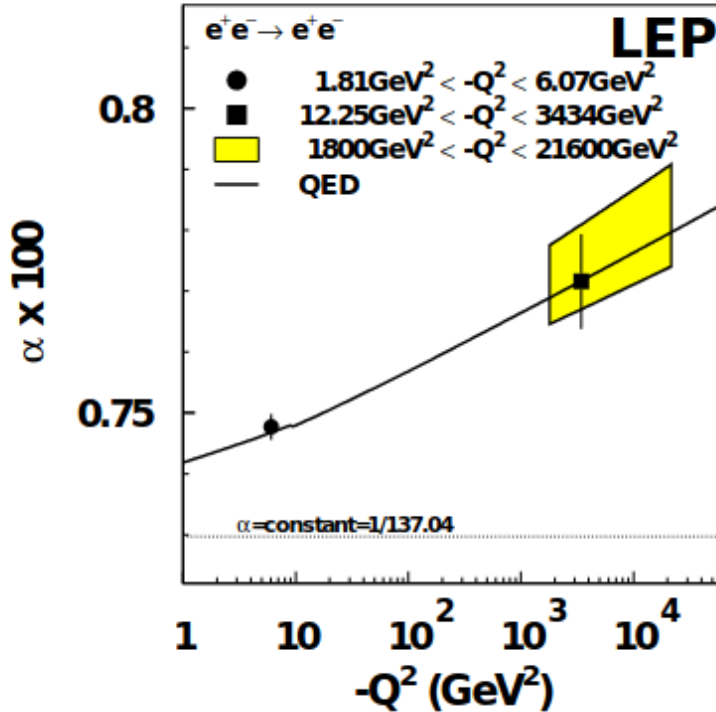


Figure 1.2: QED coupling strength α as a function of four-momentum transfer Q^2 [11].

1.2.5 Quantum Chromodynamics

Quantum Chromodynamics (QCD) is the Quantum Field Theory of $SU_c(3)$ gauge symmetry group and describes the strong interaction between color charge particles, namely quarks. Corresponding to the $SU_c(3)$ symmetry there are $3^2 - 1 = 8$ color charges which are conventionally called red, blue, and green. The net color of any bound state (hadrons) is zero as the color charge is conserved in QCD.

During the studies of baryon Ω^- (sss) and Δ^{++} (uuu), the color charge concept was first proposed. We know that three identical quarks with parallel spins can't sit together as it violates the Pauli exclusion principle. The color quantum number was introduced to resolve this issue.

Gluon is the mediator of strong interaction in QCD like the photon in QED. Gluons are

massless with spin-1. The Lagrangian of quantum chromodynamics is given by

$$\mathcal{L}_{QCD} = \bar{\Psi}_i (i(\gamma^\mu D_\mu)_{ij} - m\delta_{ij}) \Psi_j - \frac{1}{4} G_{\mu\nu}^a G_a^{\mu\nu}, \quad (1.7)$$

where Ψ represents the quark fields with mass m , $D_\mu = \partial_\mu - \frac{1}{2}igA_\mu^\alpha\lambda_\alpha$ is the covariant derivative, A_μ^α are eight gluon fields and λ_α are Gell-Mann matrices. $G_a^{\mu\nu}$ is gluon field tensor:

$$G_{\mu\nu}^a = (\partial_\mu A_\nu - \partial_\nu A_\mu + g_s f_{abc} A_b^\mu A_c^\nu), \quad (1.8)$$

where g_s is the coupling constant and f_{abc} represents the SU(3) structure constants with the indices $a, b, c \in [1, \dots, 8]$. Gluons have a few interesting features as they can interact with each other, but do not interact with the Higgs field or any other scalar field. In a re-normalizable quantum field theory, the coupling constant is a function of momentum transfer (Q^2) and given by

$$\alpha_s(Q^2) = \frac{\alpha_s(\mu^2)}{1 + \frac{\alpha_s(\mu^2)}{12\pi}(33 - 2n_f)\ln(\frac{Q^2}{\mu^2})}. \quad (1.9)$$

Where n_f is the number of quark flavors ($n_f = 6$ in SM). Fig. 1.3 shows that the strong coupling decreases with the increase of momentum transfer. At such high energy ($Q \gg \Lambda_{QCD}$, $\Lambda_{QCD} \sim 200$ MeV) or small distance, the interaction between quarks is very weak, and the phenomenon is referred to as asymptotic freedom. The utmost case of asymptotic freedom is a Quark-Gluon Plasma (QGP) as discussed in section 1.2.6. In QCD, the energy scale of confinement is determined by Λ_{QCD} . Below the Λ_{QCD} scale, quarks group into bound states to form hadrons (as the strong coupling constant increases), and the phenomenon is known as color confinement. Hence there is no experimental observation of free quarks to date at such low energies.

The theory of Electrodynamics (QED) was combined with the weak interaction to obtain the Electroweak theory [13] unifying two of the four fundamental forces of nature. The addition of Quantum Chromodynamics - the quantum theory of strong interactions in quarks and gluons, makes the SM almost complete, albeit with a conjectured unification of the strong and electroweak forces at some high energy scale. A quantum theory of gravity, however, has proven elusive so far, thus preventing a grand unification of all forces in nature.

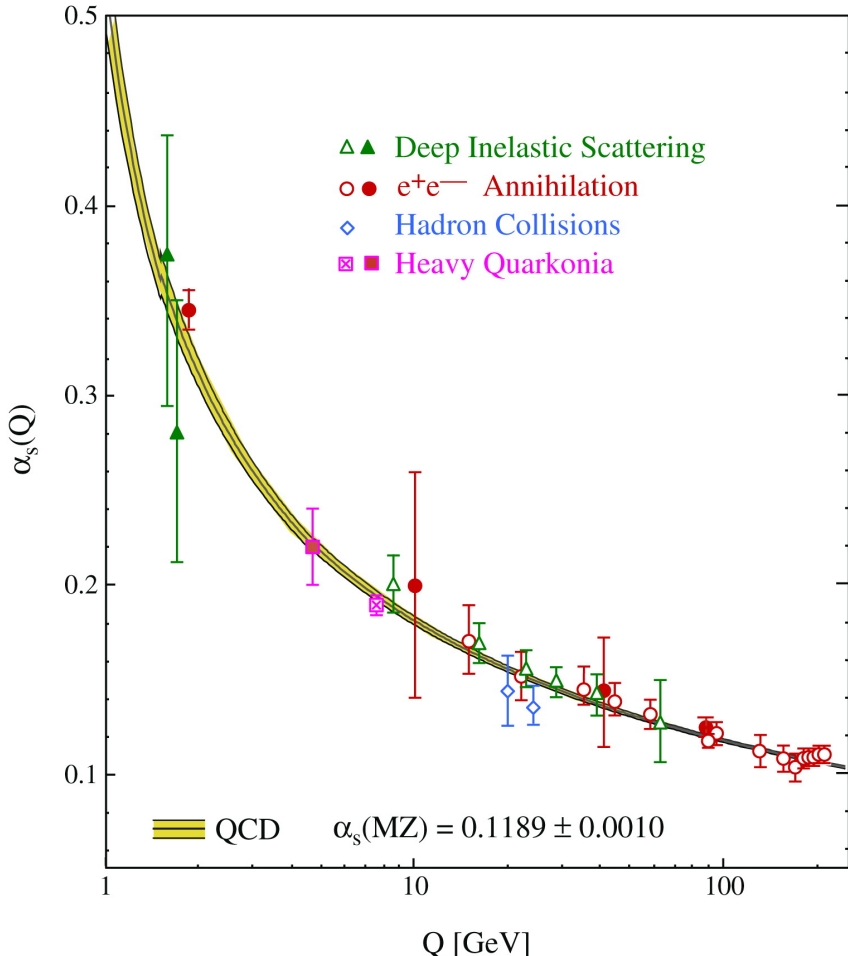


Figure 1.3: QCD coupling constant $\alpha_s(Q)$ as a function of energy scale Q [12].

1.2.6 Quark-Gluon Plasma (QGP)

The quark-gluon plasma (QGP) is an exotic state of matter predicted by QCD. According to QCD, the strong coupling constant decreases at high energy. Thus, in an extremely high energy density environment, quarks and gluons are expected to form a relativistic weakly-interacting parton gas which is a QGP.

Fig. 1.4 shows the QCD phase diagram with baryon chemical potential (μ_B) on the X-axis and temperature on the Y-axis. Also, it shows the regions that various accelerator facilities have probed. Here μ_B is analogous to the net baryon number of a system. When the baryon chemical potential is close to zero, a smooth crossover phase transition from confined to deconfined quarks occurs at a temperature of around 170 MeV. There is also a first-order transition at high

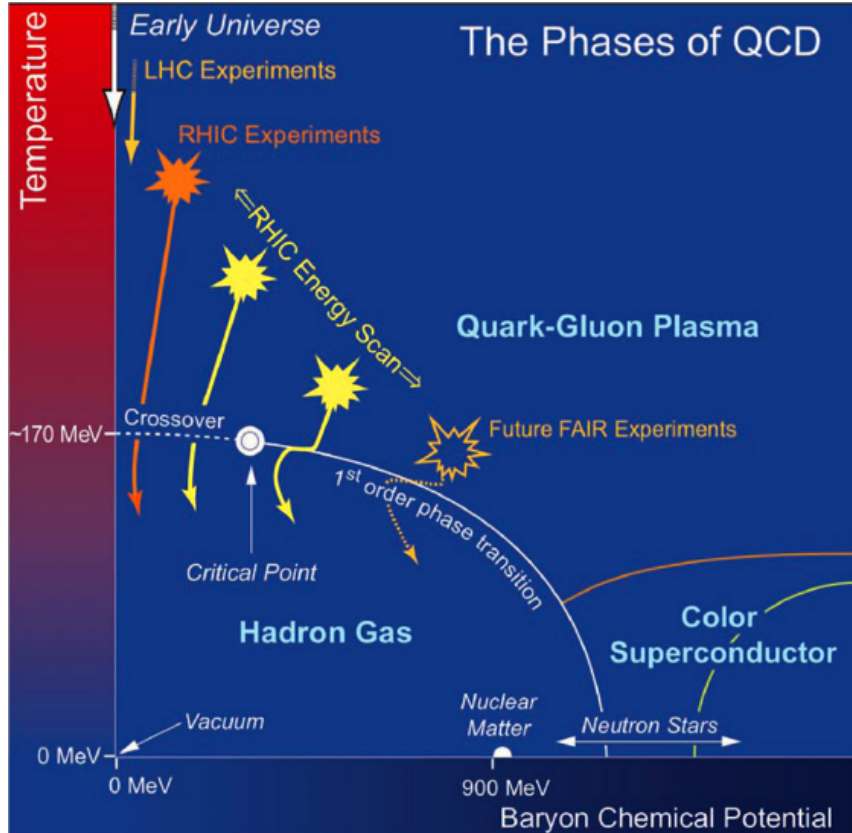


Figure 1.4: The QCD phase diagram [14].

baryon chemical potential. Few experimental observations indicate the existence of the QGP state, which are discussed below.

Nuclear modification factor: Parton energy losses due to medium induced gluon radiation in a QCD medium are expected in high energy heavy-ion collisions. One can measure this radiative energy loss indirectly in terms of the nuclear modification factor. It is defined as the ratio of yield of a given observable (such as jets, quarks, charged hadrons) produced in $A + A$ collisions to the identical observable in $p + p$ collisions at the same nucleon-nucleon energy:

$$R_{AA}(p_T) = \frac{dN_{AA}/dp_T}{\langle N_{coll} \rangle dN_{pp}/dp_T}, \quad (1.10)$$

where $\langle N_{coll} \rangle$ is the average number of binary nucleon-nucleon collisions. The symbol A refers to heavy-ion (like Lead (Pb), Gold (Au), Xenon (Xe), etc.) and p refers to proton. In particle physics, the collision energy of two particles is expressed in center-of-mass energy \sqrt{s} . The symbol \sqrt{s} is given by the square root of the Lorentz invariant quantity s . It is formed from the total energy and momentum of the two colliding particles and can be writ-

ten as $s = (E_1 + E_2)^2 - (\vec{p}_1 + \vec{p}_2)^2$. For head on collisions of two high energy particles in a collider experiment, when $E_i \gg m_i$ the center-of-mass energy \sqrt{s} is approximately $\sqrt{4E_1E_2}$.

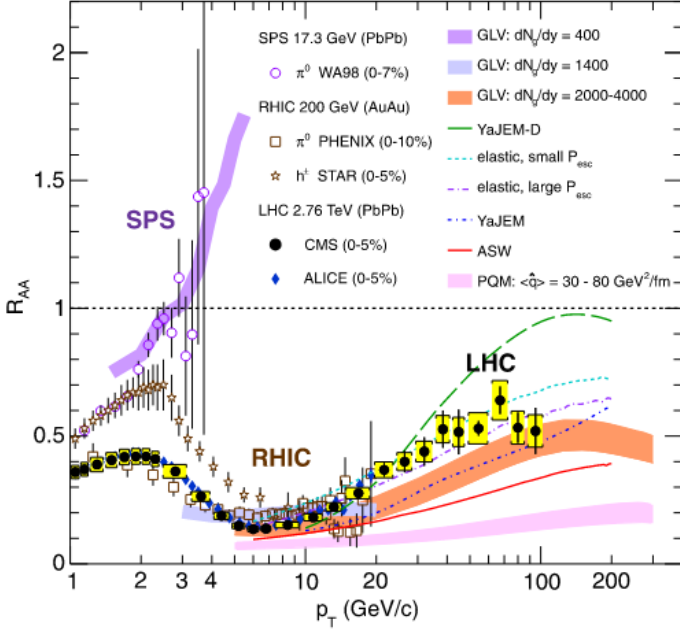


Figure 1.5: Measurements of the nuclear modification factor (R_{AA}) in central heavy-ion collisions at three different $\sqrt{S_{NN}}$ energies, as a function of p_T , for charged hadrons (h^\pm), neutral pions (π^0), and charged particles. Also, a comparison with several theoretical predictions is shown here [15].

Fig. 1.5 exhibit that low to high p_T partons confronts considerable radiative energy loss interacting with the medium. Another noticeable observation is that the maximum suppression around $p_T : 6 - 9$ GeV/c is a factor of about 7 at LHC. On the other hand, in RHIC, it is suppressed by a factor of 5. If there is no QGP formation in heavy-ion collisions, we expect to get the value of $R_{AA} = 1$.

Azimuthal asymmetries: Heavy-ion collisions could be head-on ("central") or non-central collisions. In the case of non-central collisions, the colliding ions overlap partially. Initially, a spatial anisotropy is formed in the overlapping region of non-central heavy-ion collisions, which geometrically looks like an ellipse. As a result, an asymmetry of the azimuthal distribution of final state particles can be seen in the transverse plane of heavy ion collisions. The following

Fourier expansion can represent the azimuthal distribution of particles emitted in the collision,

$$\frac{dN}{d(\phi - \Psi_{RP})} \propto 1 + \sum_n^{\infty} 2v_n \cos(n(\phi - \Psi_{RP})) \quad (1.11)$$

where ϕ is the azimuthal angle of emitted particle, ψ_{RP} is the reaction plane angle and v_n is the n^{th} order flow coefficient. A schematic diagram of an azimuthal plane and angle can be found in Fig. 1 of Ref. [16]. The term v_2 for $n = 2$ is known as elliptic flow and can be written as

$$v_2 = \langle 2v_n \cos(2(\phi - \Psi_{RP})) \rangle. \quad (1.12)$$

The Elliptic flow (v_2) is another important observable apart from R_{AA} that has been measured in several heavy-ion collision experiments. We expect $v_2 = 0$ in the absence of QGP effects.

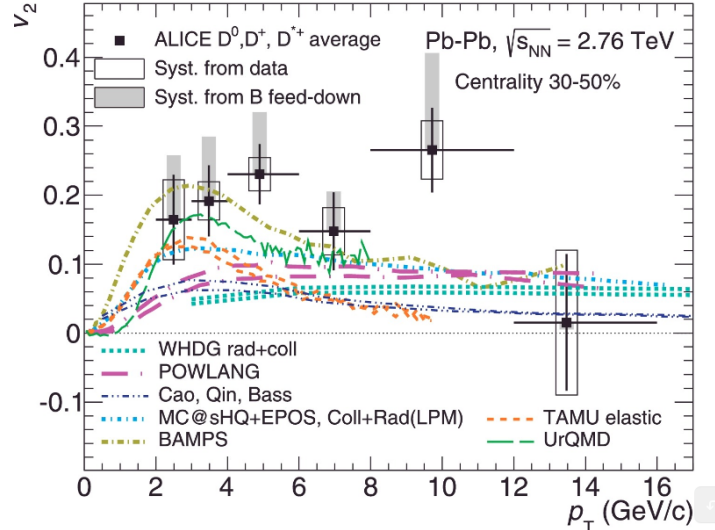


Figure 1.6: Elliptic flow (v_2) of average D mesons as a function of p_T in Pb-Pb collisions at center-of-mass energy 2.76 TeV [17].

Fig. 1.6 shows the elliptic flow as a function of p_T for D meson in the ALICE experiment. We observed a non-zero value of v_2 throughout the entire p_T range confirming the presence of a QGP. Physically, it implies that partons suffer larger energy losses along the long axis (larger transverse path length in the medium).

1.2.7 Parton distribution function

In ep scattering, photons emitted from an electron can probe the structure of the proton. At higher energy, when the wavelength of the photon is small compared to the radius of a proton (i.e $\lambda_{\text{photon}} < r_p$), a photon can interact with the proton constituent. In that case, a proton can dissociate into many final state particles. The cross-section of such a process depends on the momentum transfer and scattering angle of the source electron. This cross-section is associated with a proton structure function.

From factorisation theorem [18], the total cross-section of a hadronic process $A + B \rightarrow X$ can be written as

$$\sigma_{AB} = \int dx_a dx_b f_{a/A}(x_a, Q^2) f_{b/B}(x_b, Q^2) \times \hat{\sigma}_0(ab \rightarrow X). \quad (1.13)$$

So, the total cross-section is factorised into the leading-order partonic process $\hat{\sigma}_0$, and normalization from parton distribution functions (PDF) $f_{a/A}$ and $f_{b/B}$ of the initial-state partons a and b that belong to the hadrons A and B , respectively. We need to know appropriate PDFs to measure the total cross-section.

The distribution of proton constituents is shown in Fig. 1.7. In this figure, x is the longitudinal momentum fraction carried by parton and Q^2 is the four-momentum square of the photon. It shows that the gluon dominates at low Bjorken- x and the uncertainty is larger in this region. So, more measurements are needed to reduce the uncertainty and explore this region. Conversely, the up and down quarks are dominated at high Bjorken- x .

It is also possible to explore low Bjorken- x in ultra-peripheral collisions at the LHC. More details of it are discussed in section 2.

1.2.8 Insufficiency of the Standard Model

SM is compact and many aspects of it have been experimentally verified to high accuracy. However, SM can't explain some of the experimental observations which are listed below.

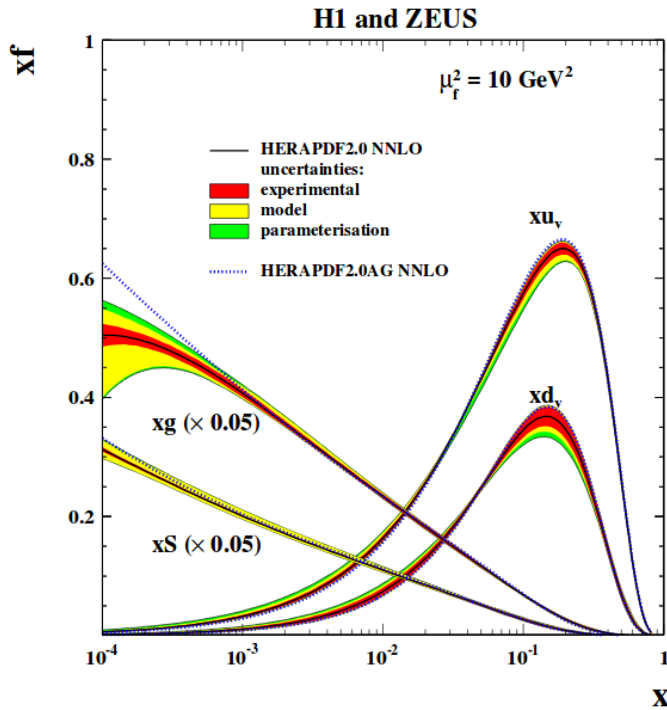


Figure 1.7: Parton distribution function in proton from HERA data and theoretical prediction [19].

1. **Hierarchy problem:** It is expected that quantum loop correction in the Higgs boson propagator contributes to the Higgs boson mass. Approximately it can be written as $m_H^2 \approx m_{bare}^2 + \Delta m_h^2$, where m_H is measured Higgs mass, m_{bare} is a negative free parameter, and Δm_h is loop correction term which is proportional to high mass scale Λ . If the SM is valid up to the Planck scale ($\Lambda_{pl} \sim 10^{19}$ GeV), this loop correction inflates the Higgs mass to a very large value. But it requires some unnatural fine-tuning of SM parameters to constrain the experimental observed Higgs mass ($M_H \sim 125$ GeV) around the electroweak scale ($\Lambda_{ew} \sim 100$ GeV). This is known as the hierarchy problem.
2. **Neutrino masses:** In the SM, neutrinos are massless. However, the experimental observation of neutrino oscillations between their flavor eigenstates proves that they possess a non-zero mass. In the SM, it is not completely understood how neutrinos gain mass.
3. **Dark matter:** Cosmological observations like galaxy rotation curves and galaxy cluster masses indicate that a significant part of the universe's mass budget is not observable through any known interaction. Ascribing this unobservable mass to particles, such particles are called dark matter particles. However, none of the SM particles is a good

candidate for such dark matter.

4. **Gravity:** The SM describes well three fundamental forces: the electromagnetic force, the strong force, and the weak force at the quantum level. Furthermore, the coupling constants of these forces are expected to evolve to a unified value at the Planck scale. Finding an equivalent quantum theory of gravity that fits in this framework, however, remains the outstanding problem facing the unification of all forces.
5. **Baryon asymmetry:** We observed that the universe is dominated by matter. The SM does not explain the imbalance of matter and antimatter in the Universe.

1.3 Motivation for this study

How does the proton gain mass? We know that proton is made of uud quarks. But the sum of these three quark masses is only about 1% of the measured proton mass. How does it acquire 99% extra mass? The hidden story is carried by the gluons which bind quarks together. This binding energy contributes to the proton mass.

In section 1.2.7, we have seen that the proton structure function xf depends on Bjorken- x and Q^2 . Fig. 1.7 shows that the distribution of quarks is very well known through the entire range of x ($x \in [0, 1]$). But the gluon distribution is poorly understood at small values of Bjorken- x , where non-linear QCD effects like gluon saturation could be prominent.

In next chapter, we will see that exclusive vector meson photo-production can probe the gluon distribution of protons since it is related to the slope parameter- b of the differential cross-section ($\frac{d\sigma}{dp_T^2} \propto e^{-bp_T^2}$) of this process.

All the above reasons drive me to study exclusive vector meson photo-production in p-Pb collisions at high energy at the LHC.

1.4 Thesis outline

The subject matter of the thesis is presented in the following eleven chapters,

- ✓ Chapter-1: Introduction to particle physics.
- ✓ Chapter-2: This chapter includes an introduction to UPC and why I'm interested to look for vector meson photo-production in UPC.
- ✓ Chapter 3: Experimental techniques of particle detection is explained here.
- ✓ Chapter-4: It includes information on DATA and MC simulation used in this analysis.
- ✓ Chapter-5: Details of event selection are discussed here.
- ✓ Chapter-6: In this chapter, I discussed the measurement of single muon efficiency, muon ID efficiency, and muon tracking efficiency. Also, Detector acceptance and efficiency estimation from MC is discussed here.
- ✓ Chapter-7: Dimuon invariant mass fitting procedure is discussed here.
- ✓ Chapter-8: Estimation of different background contributions in the signal region, background subtraction and extraction of Υ cross-section is explained here.
- ✓ Chapter-9: Different sources of systematic uncertainty and their contribution to the results are discussed in this chapter
- ✓ Chapter-10: This chapter includes the results of this analysis.
- ✓ Chapter-11: this chapter contains a summary of the analysis results and observations.

Chapter 2

Ultra-peripheral collisions and photo-production

2.1 Ultra-peripheral collisions of heavy-ions

Exclusive photo-production of vector mesons (VM) is an important benchmark process in ultra-peripheral collisions (UPCs). Ultra-peripheral collisions (UPC) are characterized by impact parameters larger than the sum of the radii of the incoming hadrons [20]. The impact parameter is defined as the perpendicular distance between the path of a projectile and the center of the target in a collision system. In UPCs, hadronic interactions are strongly suppressed, resulting in a dominance of the long-range electromagnetic interaction over the short-range strong force. Hence the photon plays a crucial role in UPC, and the probability of such interactions is enhanced by the photon flux. Fig. 2.1 shows a schematic diagram of electric field and photon radiation from relativistic heavy-ions. The cross-section of ultra-peripheral heavy-ion collisions

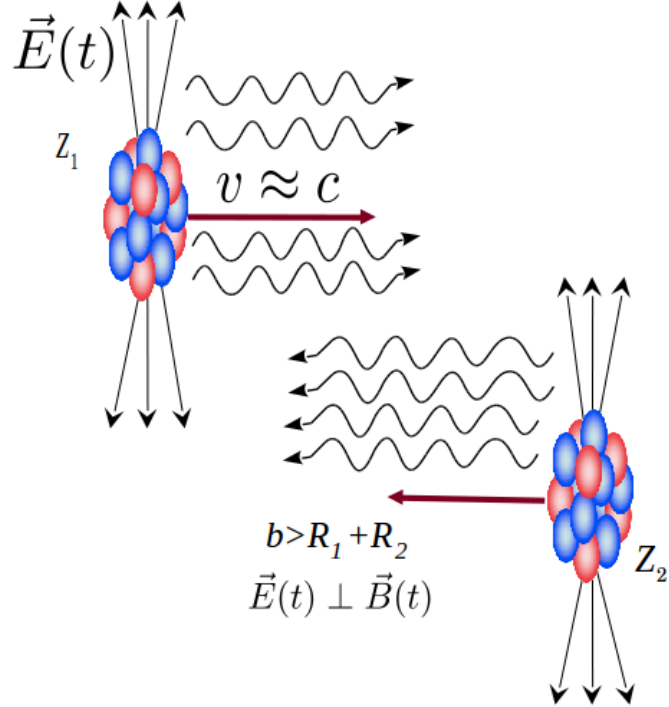


Figure 2.1: Schematic diagram of electric field and photon radiation from relativistic heavy-ions.

can be expressed as

$$\frac{d\sigma_{A_1 A_2}}{dy} = N_{\gamma/A_2}(y)\sigma_{\gamma A_1}(y) + N_{\gamma/A_1}(-y)\sigma_{\gamma A_2}(-y). \quad (2.1)$$

In Eq. 2.1, $N_{\gamma/A_2}(y)$ represents that the 2nd relativistic ion A_2 is the source of the photon that interacts with the target ion A_1 and $N_{\gamma/A_1}(y)$ represents the opposite scenario. Relativistic charged particles radiate photons. We can explain it from classical electrodynamics. The total radiated power ($P_{rad}(r)$) passing out through a surface of spherical shell is the integral of the Poynting vector (\mathbf{S}): $P_{rad}(r) = \oint \mathbf{S} \cdot d\mathbf{a} = \frac{1}{\mu_0} \oint (\mathbf{E} \times \mathbf{B}) \cdot d\mathbf{a}$. The area of a sphere goes as $4\pi r^2$. So, the radiation could occur if the pointing vector doesn't go faster than $1/r^2$. For example, if \mathbf{S} goes as $1/r^3$ then

$$P_{rad} \equiv \lim_{r \rightarrow \infty} P_{rad}(r) = \lim_{r \rightarrow \infty} \frac{1}{r^3} \times r^2 = 0. \quad (2.2)$$

In relativistic case, both \mathbf{E} and \mathbf{B} consist of $1/r$ term (Eq. 10.65 and 10.66 of Ref. [21]). As a result, P_{rad} become finite in the limit of $r \rightarrow \infty$. Thus relativistic charged particles become a source of photon/radiation.

According to Weizsäcker-William approximations, the photon number density [22] from a relativistic nucleus with charge Z is

$$N(k, b) = \frac{Z^2 \alpha k}{\pi^2 (\hbar c)^2 \gamma^2} [K_1^2(x) + \frac{1}{\gamma^2} K_0^2(x)] \quad (2.3)$$

where k is the photon energy, $x = kb/\gamma\hbar c$, b is the impact parameter, $\alpha \approx 1/137$ is the electromagnetic fine structure constant, γ is the Lorentz boost and K_1 and K_0 are modified Bessel functions. Here K_1 and K_0 give the photon flux in the transverse and longitudinal direction respectively. The transverse term K_1 is dominant as $\gamma \gg 1$ for relativistic ions.

2.2 Vector meson photo-production

In this case, one of the incoming hadrons emits a quasi-real photon that converts into a $q\bar{q}$ pair, which interacts with the other hadron via a color-singlet gluon (i.e. only two gluons) exchange producing a bound state of a $q\bar{q}$ pair, namely a VM [23, 24]. Photo-production of VM is strongly enhanced in heavy ions as the photon flux grows as Z^2 , where Z is the charge of the ion. Thus, for photo-production, Proton-lead (p+Pb) collisions have an advantage over proton-proton (p+p). On the other hand, relative to lead-lead (Pb+Pb) collisions, center-of-mass energies and luminosities are larger for p+Pb collisions at the LHC [25]. Also, one more advantage of the asymmetric system (i.e. p+Pb) is that there is no ambiguity to determine the photon direction and hence the photon-proton center-of-mass energy $W_{\gamma p}$.

The cross-section of exclusive vector meson photo-production can be expressed as

$$\frac{d\sigma_{\gamma A \rightarrow VA}}{dt} = \frac{d\sigma_{\gamma A \rightarrow VA}}{dt} \Big|_{t=0} |F_A(t)|^2, \quad (2.4)$$

where $\frac{d\sigma_{\gamma A \rightarrow VA}}{dt} \Big|_{t=0}$ is the forward elastic scattering amplitude and $F_A(t)$ is the form factor of tar-

get nuclei. Numerically, the form factor represents the Fourier transform of the nuclear density. Parameter t indicates the squared four-momentum transfer at the proton vertex, $|t| \approx p_T^2$

In this work, the exclusive photo-production of Υ mesons is studied in pPb collisions, using the process $p\text{Pb} \rightarrow (\gamma p) \rightarrow p\Upsilon\text{Pb}$ shown in Fig. 2.2a. The data is collected at $\sqrt{s_{NN}} = 8.16$ TeV with the CMS detector. In this process, the main dominating background is the QED process, where both proton and lead ion radiate photons and produce an exclusive dimuon (Fig. 2.2b). If the Υ photo-production is followed by the proton breakup, the process is called "semi-exclusive" (Fig. 2.2c).

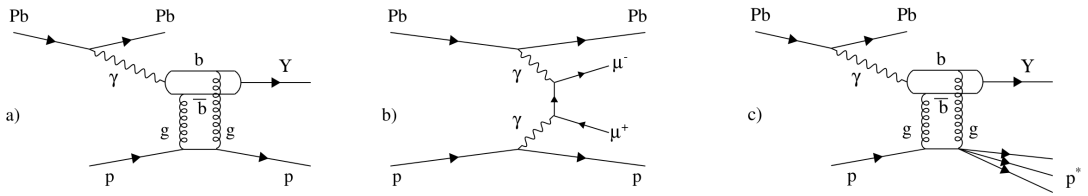


Figure 2.2: Diagrams representing (a) exclusive Υ photo-production, (b) exclusive dimuon QED continuum production, and (c) proton dissociation background in pPb collisions.

In particular, the photo-production of Υ mesons off protons is highly sensitive to the gluon density of the target nuclei. The mass of the bottom quark provides a hard scale, justifying the use of the factorization theorem of perturbative QCD (pQCD) [26–28]. In the leading logarithmic approximation of perturbative QCD (pQCD), the photo-production cross-section of a Υ vector meson is proportional to the square of the gluon density in the target (i.e. $\frac{d\sigma_{\gamma p \rightarrow \gamma p \Upsilon}}{dt} \Big|_{t=0} \propto [xG(x, Q^2)]^2$) [26–38].

Experimental results of exclusive photo-production of Υ , J/ψ in UPCs at HERA and LHC, reveal the importance of these measurements to probe the gluon distributions in nucleons and in nuclei at small Bjorken x , where x is the fraction of target longitudinal momentum carried by the gluon. In this analysis, proton considered as the target. Exclusive photo-production of Υ was first studied at the HERA with electron-proton collisions [39–42]. At the LHC, the LHCb experiment has measured the exclusive photo-production of J/ψ , $\psi(2S)$ and Υ at forward rapidities ($2 < y < 4.5$) in proton-proton UPC at 7, 8 TeV [43, 44]. The CMS collaboration has measured exclusive Υ photo-production in pPb collision at $\sqrt{s_{NN}} = 5.02$ TeV within the rapidity range $|y| < 2.2$ corresponding to $91 < W_{\gamma p} < 826$ GeV [45]. The ALICE collaboration has

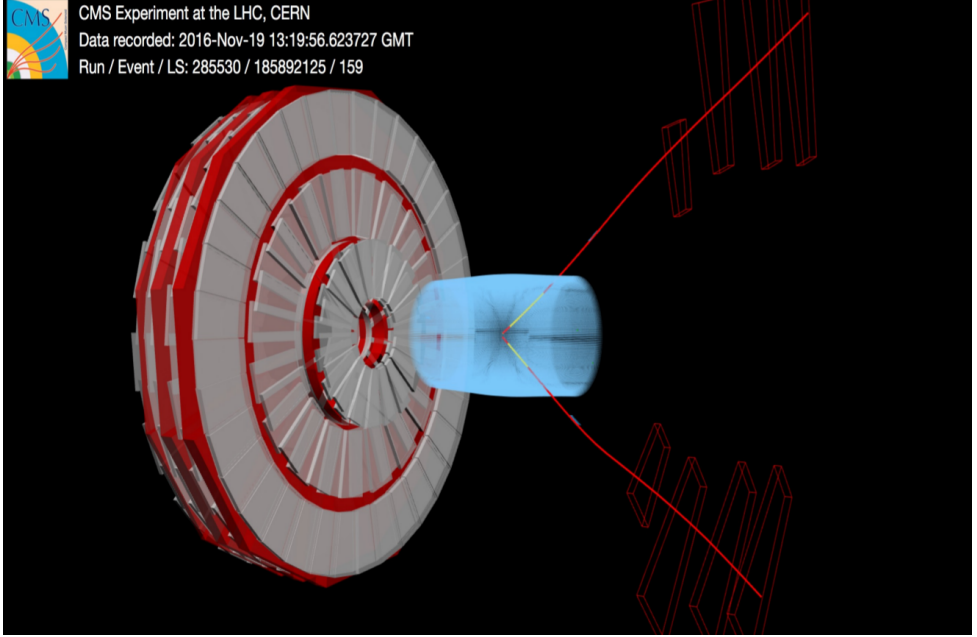


Figure 2.3: Event display of a typical exclusive Υ photo-production in pPb collisions.

measured exclusive J/ψ photo-production in pPb collision at $\sqrt{s_{NN}} = 5.02$ TeV in the rapidity intervals $2.5 < y < 4.0$ (p-Pb) and $-3.6 < y < -2.6$ (Pb-p) corresponding to $21 < W_{\gamma p} < 45$ GeV and $577 < W_{\gamma p} < 952$ respectively.

A characteristic feature of exclusive heavy VM photo-production is the rapid rise of the cross section with the photon-proton centre-of-mass energy $W_{\gamma p}$. All experiments have shown that the Υ cross section follows a power-law dependence, i.e. $\sigma \propto W_{\gamma p}^{\delta}$ with $\delta = 0.7 - 1.2$ [40, 41, 45]. Also, the differential cross-section of exclusive VM photo-production depends on t and can be parameterized as $\frac{d\sigma}{dt} \propto e^{(-b|t|)}$ for proton targets at low values of $|t|$. The slope parameter b is related with the parton transverse density distribution of the proton [26, 27, 46]. From Regge theory, the slope parameter b is energy dependent ($W_{\gamma p}$) [47] and given by the form

$$b(W_{\gamma p}) = (\alpha + \alpha' \ln(W_{\gamma p}/W_0)) \text{ GeV}^{-2}, \quad (2.5)$$

where W_0 is central value of $W_{\gamma p}$ range, α and α' are constant parameters.

We know that, photon energy $k = (M_{\Upsilon(1S)}/2) \exp(\pm y)$ [48]. The center-of-mass energy \sqrt{s} of two high energy colliding particle in collider experiment is approximately $\sqrt{4E_1 E_2}$. So,

photon-proton centre-of-mass energy can be written in terms of rapidity as

$$W_{\gamma p} = \sqrt{4kE_p} = \sqrt{4 \times (M_{\Upsilon(1S)}/2) \exp(\pm y) \times E_p} \Rightarrow W_{\gamma p}^2 = 2E_p M_{\Upsilon(1S)} \exp(\pm y).$$

In this thesis, we present a measurement of the differential cross-section of $\Upsilon(1S)$ photo-production with p_T^2 and y , as well as the total cross-section of $\Upsilon(1S)$ with $W_{\gamma p}$. We have measured the exclusive $\Upsilon(1S)$ photo-production in the rapidity range $|y| < 2.2$ corresponding to $117 < W_{\gamma p} < 1054$ GeV and probing the gluon density in the proton in low values of Bjorken $x \approx 10^{-4} - 10^{-2}$, where non-linear QCD effects could play a key role and provide evidence of the gluon saturation effect [49–51]. A well-known example of non-linear QCD is the gluon radiation, which rises as a power of the energy with which the hadron is probed [52]. However, at a certain point, the gluon density becomes so high that these gluons start recombining and controlling this growth. This phenomenon is known as the gluon saturation effect.

Chapter 3

Experimental techniques of particle detection

3.1 Particle interactions with matter

Since particle physics experiments depend on detecting and identifying particles, it is necessary to understand the details of particle interactions with matter. This section discusses the different mechanisms through which particles interact with matter and leave a ‘signature’ signal of their passage [53].

3.1.1 Ionization energy losses

As a particle (projectile) travels through a material, it interacts with the constituent atoms(targets). If the projectile is a charged particle, the interaction is primarily electromagnetic (i.e. governed by the Coulomb force) with some relativistic and radiative (bremsstrahlung) effects becoming

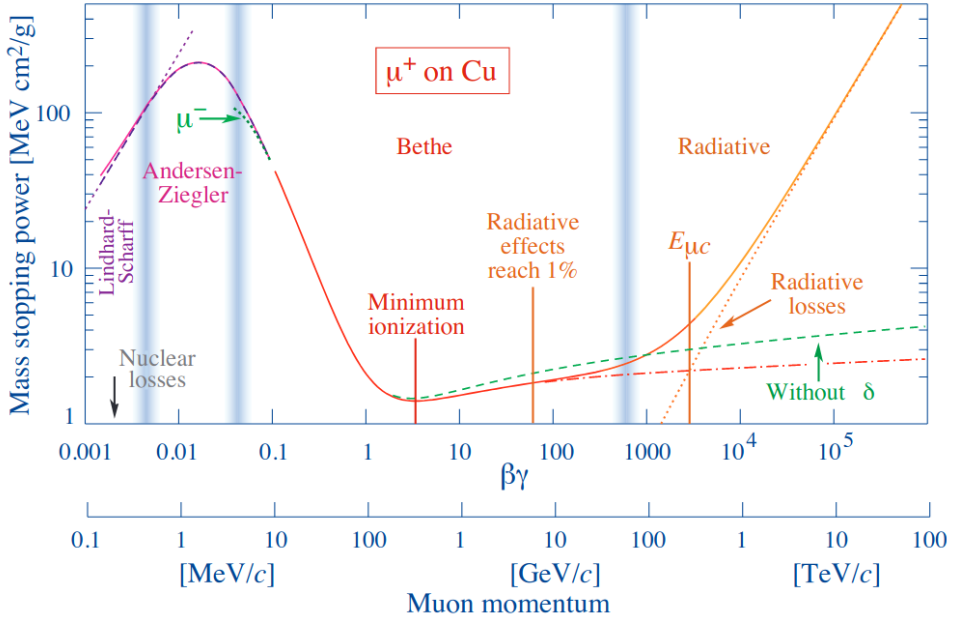


Figure 3.1: Mean energy loss $-\langle \frac{dE}{dx} \rangle$ for positive muons in copper as a function of $\beta\gamma$ (Particle Data Group, 2018).

important at high energy. The particle loses some energy per unit length travelled, characterized by the Bethe-Bloch energy loss formula [54]. The energy lost by the projectile is transferred to the target. Since the electromagnetic interactions governing the energy loss are primarily with outer shell electrons, the atoms get ionized if the energy is larger than the ionization energy of the atom. Such ionized atoms (in case of gas detectors) or electron-hole pairs (in case of solid semiconductor detectors) provide the electronic signal of the projectile's passage through the material.

The mean energy loss of relativistic charged particles is given by the Bethe–Bloch equation:

$$\left\langle -\frac{dE}{dx} \right\rangle = K z^2 \frac{Z}{A} \frac{1}{\beta^2} \left[\frac{1}{2} \ln \frac{2m_e c^2 \beta^2 \gamma^2 W_{max}}{I^2} - \beta^2 - \frac{\delta(\beta\gamma)}{2} \right] \quad (3.1)$$

with $K = 4\pi N_A r_e^2 m_e c^2$. Details of variables used in Eq. 3.1 are given in Table 3.1.

Fig. 3.1 shows the mean energy loss $-\langle \frac{dE}{dx} \rangle$ for positive muons in copper as a function of $\beta\gamma$. From Fig. 3.2, in the low momentum region, $-\langle \frac{dE}{dx} \rangle$ falls rapidly due to the $1/\beta^2$ term in the Bethe-Bloch equation.

Table 3.1: Summary of variables used in equation 3.1.

Symbol	Variable name	Symbol	Variable name
r_e	classical electron radius	β	v/c of the incident particle
m_e	electron mass	I	mean excitation energy
N_A	Avogadro's number	z	charge of incident particle
Z	atomic number of absorber	γ	$(1 - \beta^2)^{-1/2}$
A	atomic mass of absorber	δ	density correction
W_{max}	maximum energy transfer in a single collision	x	distance travelled by the incident particle in the medium

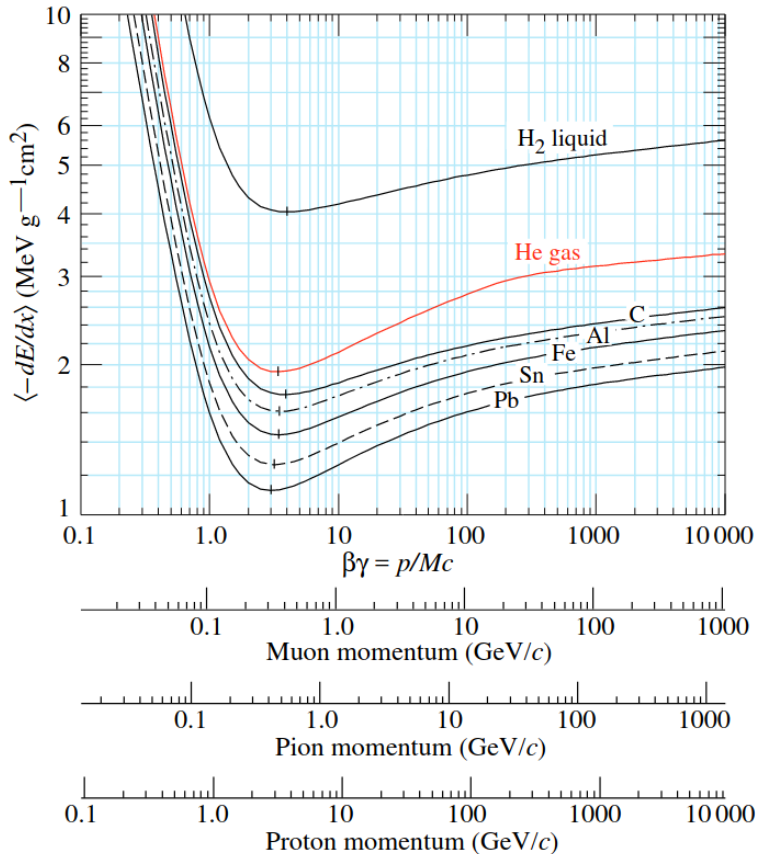


Figure 3.2: Mean ionization energy loss $-\langle \frac{dE}{dx} \rangle$ curves for a singly charged particle in various materials as a function of $\beta\gamma$ (Particle Data Group, 2018).

As shown in Fig. 3.2, a remarkable feature of the Bethe-Bloch energy loss formula is that the mean energy loss of different projectiles (muons, pions and protons shown) having a broad range of momentum is constant and at a minimum value (both x and y axes of the figure are

on a log scale). Hence charged particles with momentum in this range are called ‘Minimum Ionizing Particles’ (MIP’s). This feature occurs irrespective of the target material (the heaviest element Pb to the lightest H₂ are shown in Fig. 3.2). This is because of the Z/A dependence in the energy loss formula Eqn. 3.1: $Z/A \approx \text{constant}$ for stable elements of the periodic table.

At high momentum, there is a relativistic rise of $-\langle \frac{dE}{dx} \rangle$ due to logarithmic dependency on $(\beta\gamma)^2$ in the Bethe-Bloch equation.

This relativistic rise gets cancelled by the medium dependent density correction term $\delta(\beta\gamma)$ in Eq. 3.1. At $\beta\gamma \approx 1000$ GeV/c, radiative effect becomes more important. Fig. 3.3

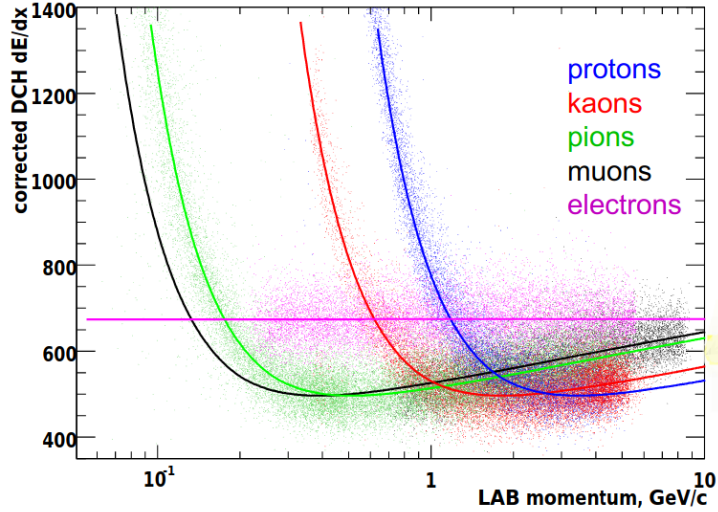


Figure 3.3: $-\langle \frac{dE}{dx} \rangle$ curves as a function of different projectiles (electrons, muons, protons, kaons, and pions) momentum [fig courtesy BaBar experiment at SLAC]

shows the $-\langle \frac{dE}{dx} \rangle$ curve for various charged projectiles. The distinct nature of the $-\langle \frac{dE}{dx} \rangle$ profile in the low momentum region can be exploited to identify the projectile by simultaneously measuring the incident particle’s $-\langle \frac{dE}{dx} \rangle$ and momentum p .

3.1.2 Bremsstrahlung energy loss

The relativistic charged particles can also lose energy due to Bremsstrahlung, i.e. radiation of photons, in the Coulomb field of the atomic nuclei, as shown in Fig. 3.4. Classically, we could say this radiation arises due to the acceleration or deceleration of the charged projectile

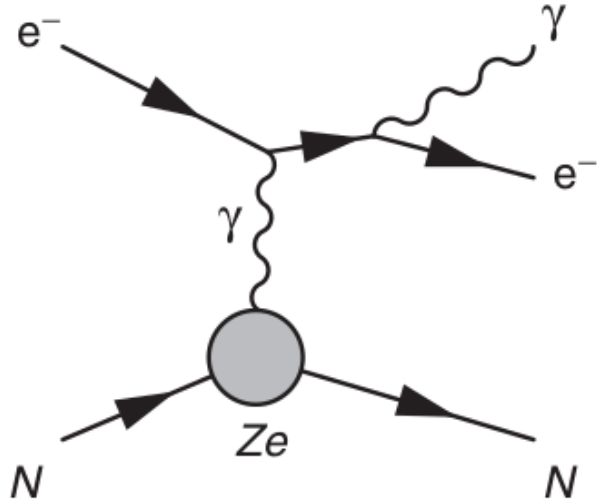


Figure 3.4: The bremsstrahlung process $e^- + N(Z,A) \rightarrow e^- + \gamma + N(Z,A)$. N is a nucleus of charge $+Ze$ [6]

when it passes through the nuclear electric field. The Bremsstrahlung emission probability is proportional to the radius square of the incident charged particle, i.e., $\sigma_{rad} \propto r_e^2 = (e^2/mc^2)^2$. Hence, the radiation energy loss is dominant for electrons and positrons relative to high mass charged particles. Total energy loss of electron or positron can be written as sum of collision-ionization energy loss and radiation loss,

$$\left(\frac{dE}{dx}\right)_{Tot} = \left(\frac{dE}{dx}\right)_{coll-ion} + \left(\frac{dE}{dx}\right)_{rad}. \quad (3.2)$$

Fig. 3.5 shows that the electron radiation energy increases rapidly as the incident electron energy increases beyond ~ 10 MeV. Also, radiation energy loss depends on the absorbing material. The energy E_C at which radiation losses become equal to the ionization energy losses is called critical energy. From Bethe and Heitler approximation [53], E_C can be written as

$$E_C = \frac{1600m_e c^2}{Z}, \quad (3.3)$$

where m_e is the electron mass and Z is the atomic number of the absorber. Similarly, a characteristic parameter of absorber material called radiation length (X_0), which is defined as the average

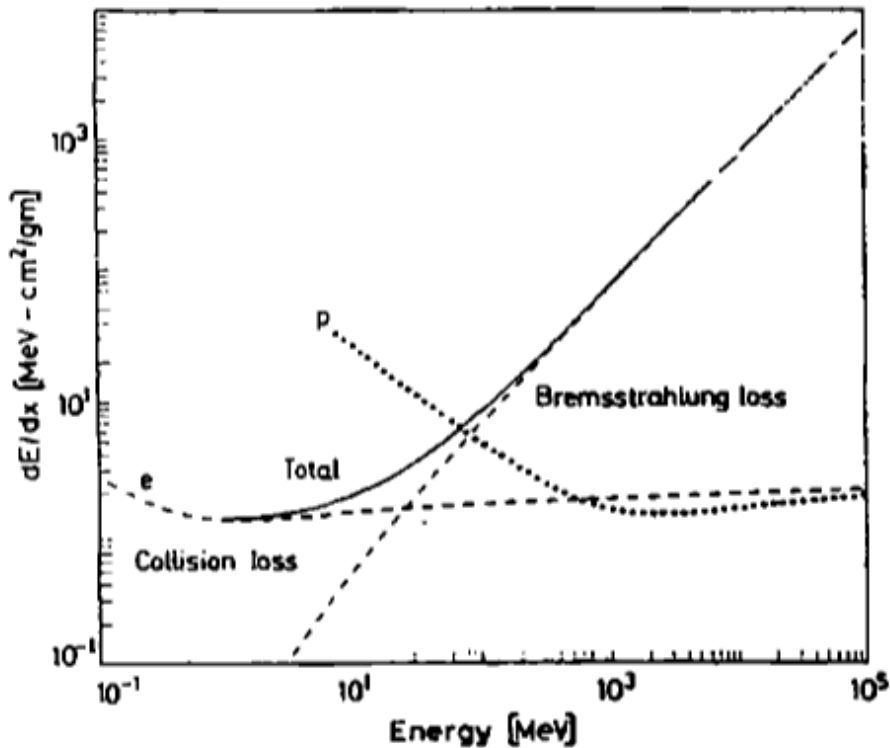


Figure 3.5: Collision-ionization energy loss, radiation energy loss, and total energy loss for an electron in copper [53].

thickness of material at which radiation energy loss is reduced by a factor e and is given by

$$\frac{1}{X_0} = 4 \left(\frac{\hbar}{mc} \right)^2 Z(Z+1) \alpha^3 n_a \ln \frac{183}{Z^{1/3}}. \quad (3.4)$$

3.1.3 Čerenkov radiation

In addition to the above two energy losses, high energy charged particles can also lose energy through photon emission, called Čerenkov radiation. When a charged particle with velocity v passes through a dielectric medium with refractive index n , the molecules in the medium become polarised. If the particle's velocity v is greater than the speed of light in that medium c/n , the molecules emit photons, which cause them to revert to their unpolarised state. In time t , the charged particle travels βct distance, whereas emitted wavefront travels a distance ct/n in

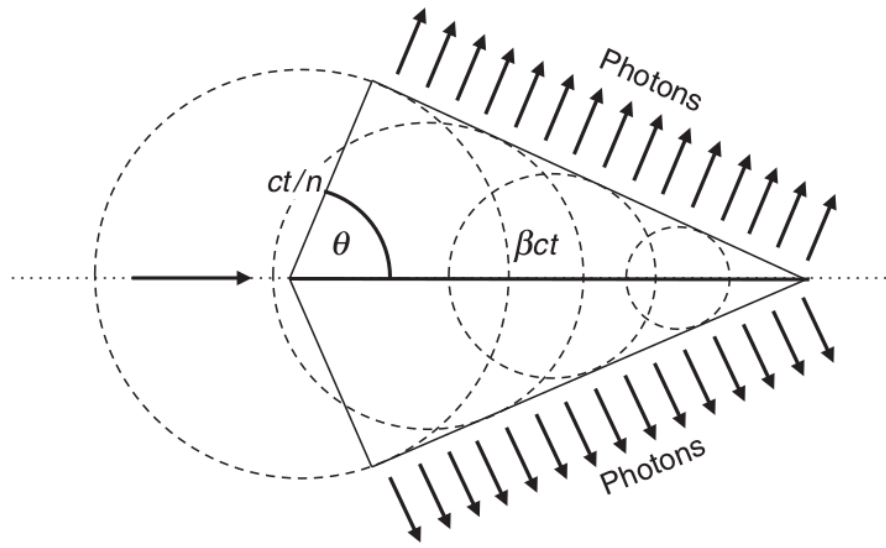


Figure 3.6: The geometry of Čerenkov radiation emitted by a charged particle travelling with velocity v greater than the speed of light (c/n) in the dispersive medium [6].

a dispersive medium, as shown in Fig. 3.6. Čerenkov radiation is emitted at a specific angle

$$\cos \theta = \frac{1}{n\beta} \quad (3.5)$$

with respect to the direction of motion of the charged particle. Photo-multiplier tubes (PMTs) or large volumes of liquid (Ex. water) can detect this radiation. This radiation occurs only when the charged particle is highly relativistic such that $\beta > 1/n$. Hence only particles having mass m and satisfying the condition

$$mc < (n^2 - 1)^{1/2} p, \quad (3.6)$$

will emit Čerenkov radiation. The energy loss due to the Čerenkov radiation is very low relative to ionization energy loss.

3.2 Particle detectors

3.2.1 Gas detectors

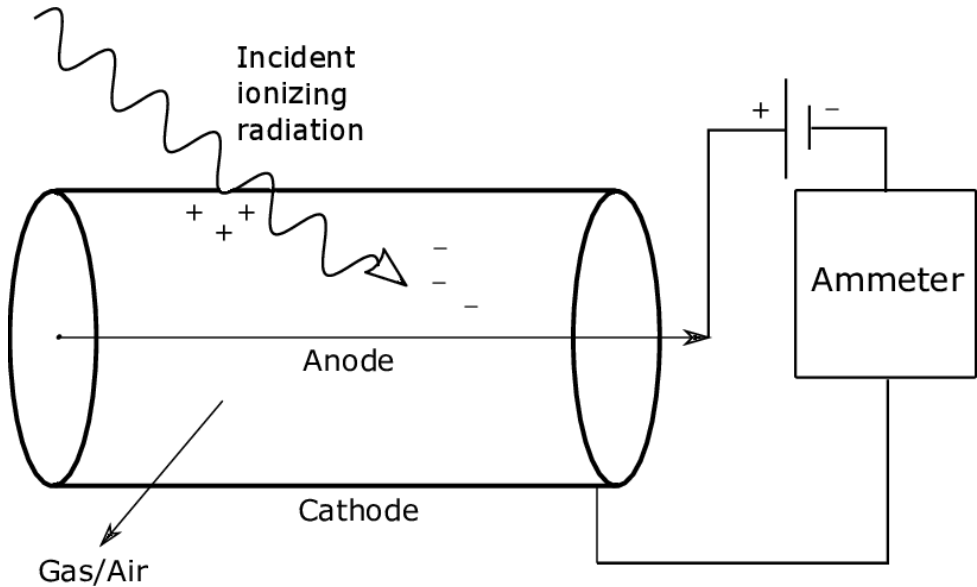


Figure 3.7: A schematic diagram of a gas-filled detector showing how gaseous ionization detectors work [55].

Fig. 3.7 shows a schematic diagram of a gas-filled detector. The gas detector detects the amount of ionization produced by a charged particle passing through the gas volume. The gas detector can be categorized in three different regions based on different phenomena of ion-pairs production under different operating parameters. These are named ionization chamber, proportional counter, and Geiger-Müller counter, as shown in Fig. 3.8.

Ionization chamber: The most basic form of an ionization chamber is made up of a pair of parallel plate electrodes filled with a gas mixture. It generates a uniform electric field $E = V/d$ after applying a voltage V to the electrodes, where d is the distance between the plates. In addition to that, the cylindrical ionization counter (Fig. 3.9) is also useful. The electric field strength of the cylindrical detector is given by

$$|E(r)| = \frac{1}{r} \frac{V}{\ln(b/a)}, \quad (3.7)$$

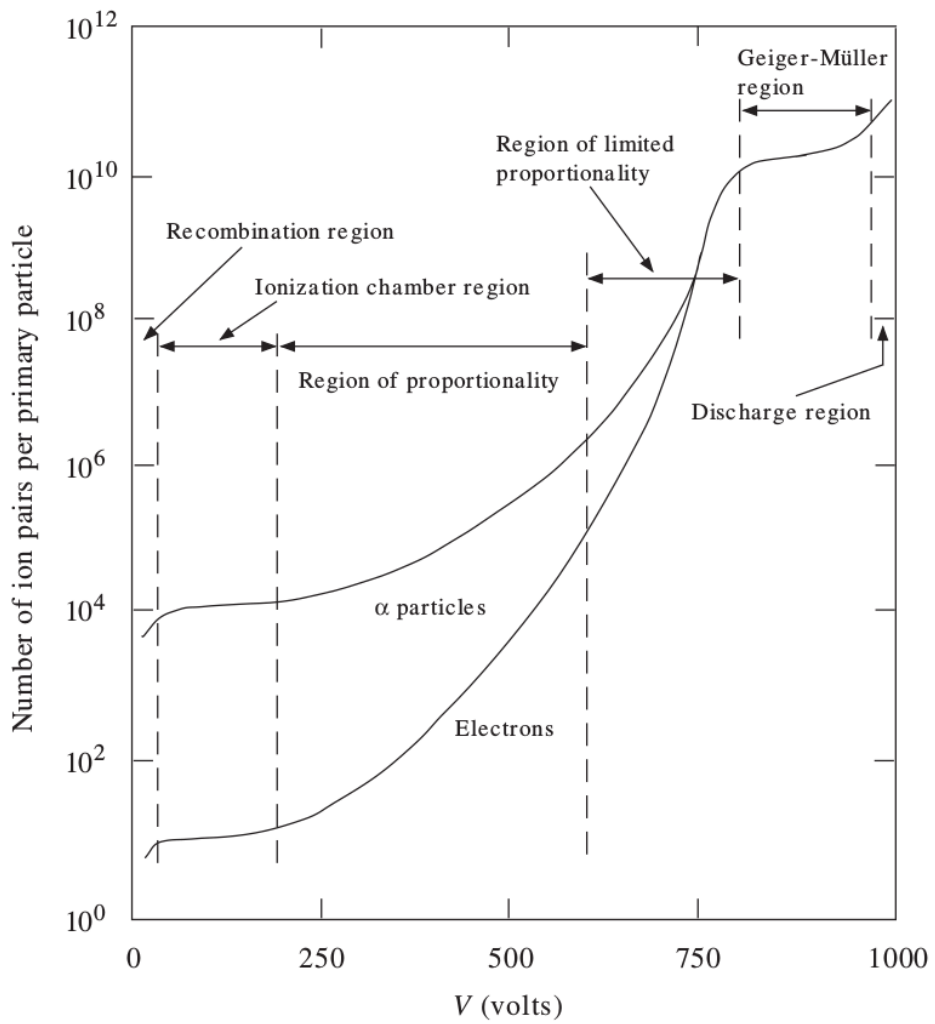


Figure 3.8: Number of collected ions as a function of voltage with different characteristic modes of operation of a single wire gas chamber [56].

where r : radial distance from central z axis; b : inner anode radius and a : outer cathode radius of cylinder. This ionization detector needs to operate above a minimum threshold voltage to

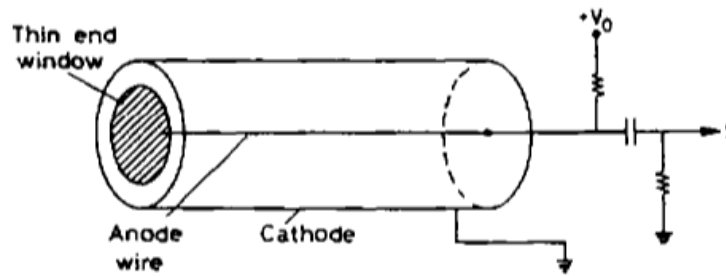


Figure 3.9: Cylindrical ionization detector [53].

prevent the produced ion pair from recombining before reaching the electrodes. If we gradually

increase the voltage, the production of ion pairs reaches saturation and gains sufficient velocity for secondary ionization. This is the upper bound of the ionization chamber. Particle energy can be measured if a particle is completely absorbed in an ionization chamber. This type of chamber has very limited use (Ex. beam monitor) due to poor energy and time resolution.

Proportional counter: If we increase the voltage in a cylindrical gas detector beyond the operation region of the ionization chamber, the primary electron created during ionization could gain adequate energy to ionize another atom. This secondary ionization causes more ionization and so on. Thus, there is an ionization amplification known as the Townsend avalanche. However, the number of avalanche electron-ion pairs is proportional to the number of primary electrons. Hence, it's called a proportional counter, and such proportionality holds up to a specific voltage region, as shown in Fig. 3.8. The gain of the output signal is high relative to the ionization chamber and the resolution is also improved for this detector. Nowadays, people use proportional detector properties in modern detectors such as multi-wire proportional chamber (MWPC) [57], micro-strip gas chamber ((MSGC) [58], gas electron multiplier (GEM) [59], etc. They all have multiple counters next to each other. As a result, it has a better position resolution.

Geiger-Müller counter: Proportionality is lost when the voltage in the proportional chamber is increased beyond a threshold. In this case, there is a fast exponential multiplication of charge in the gas chamber due to primary electrons created in ionization by the detected particle creating a very large number of secondary electrons, to the point where the gas ionization reaches a saturation level. The signal strength in a Geiger-Müller counter is not proportional to energy loss by the detected particle - it merely “counts” the number of particles passing through. Generally, Geiger-Müller counters are used as radiation safety survey meters rather than particle detectors in an experiment.

3.2.2 Semiconductor detectors

Semiconductor detectors are solid-state ionization detectors in which electron-hole pairs play a similar role as electron-ion pairs in gas detectors. For most applications, semiconductors are made of a thin silicon wafer with appropriate doping and follow the principle of the p-n junction diode, as shown in Fig. 3.10. We apply a reverse bias voltage across the p-n junction. Electron-hole pairs are created along the particle flight direction when a particle passes

through the depleted semiconductor detector. After that, electron-hole pairs are separated and drift in the direction of the applied electric field. The energy required to create an electron-hole pair in a semiconductor is about 3-4 eV, whereas, in a gas detector, it is about 30 eV. Hence semiconductor detectors are very useful for detecting low-energy particles. Examples of semiconductor detectors are silicon pixel and silicon strip detectors, mainly used for track reconstruction. Pixel/strip detectors are used in the CMS experiment, and details are discussed in Section 3.5.2.

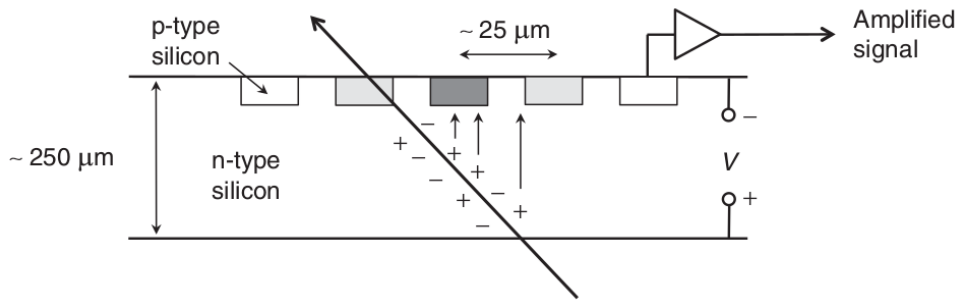


Figure 3.10: Schematic diagram of silicon tracking detector [6].

3.2.3 Scintillation detectors

A scintillation detector consists of two parts: scintillating material and a photomultiplier tube (PMT). These are coupled via photocathode, as shown in Fig. 3.11. The scintillator material usually has a complex molecular structure (often organic molecules are included). These molecules have vibrational excitation levels that decay quickly emitting photons. The photomultiplier tube consists of a photo-cathode - a material coating that emits electrons through the photoelectric effect when light is incident on it. This is followed by a sequence of electrodes maintained at a successively higher potential which also emits secondary electrons upon the incidence of primary electrons.

The scintillator material and PMT are closely coupled through an optically transparent glue. Charged or neutral particles passing through the scintillator excite molecular vibrational states, which quickly de-excite emitting photons. These photons hit the photocathode in the PMT emitting electrons by the photoelectric effect. The geometrical design of the electrodes in the PMT and their successively higher potential is such that each pair acts as a “mini elec-

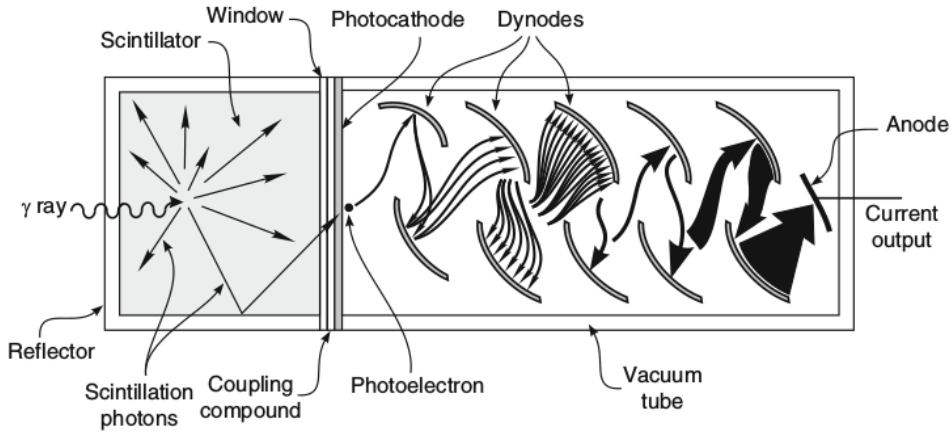


Figure 3.11: Schematic diagram of a scintillator with photomultiplier tube (PMT) [60].

tron accelerator" - hence the term "dynode". Electrons incident on one of the dynodes emits secondary electrons, which are accelerated by a high electric field to the next dynode in the sequence.

Hence there is an amplification of electrons by secondary emission at each dynode. Finally, the electron cascade is collected at the anode, which produces an output signal pulse.

The total charge deliverance in the PMT is proportional to the n^{th} power of gain, i.e. $Q \propto G^n$. Where G is the number of electrons deliverance per dynode per electron (the gain) and n is the total number of dynodes in the PMT. This detector has linear behaviour as the output voltage is proportional to the initial energy deposited by the particle. Also, it has a fast time response. Various experiments use PMT; for example, the CASTOR detector in the CMS experiment uses PMTs.

Since vibrational excited states have an extremely short lifetime, the signal response from the scintillator is very fast ($\mathcal{O}(ps)$). However, an important limitation of PMT's is that they cannot be used in areas of the detector where there is a high magnetic field, since it would distort the flow of electrons between dynodes inside the PMT. Hence, typically the scintillator may be placed in the path of the particles to be detected, but they are optically coupled by optic fibres to PMT's placed far outside the magnetic field region

3.2.4 Calorimeters

A calorimeter is a type of detector that absorbs the particle completely, i.e. it measures the total energy E of the particle. By contrast, tracking detectors rely on signals of small energy loss by the particle as it crosses the tracking detector in a magnetic field to reconstruct the particle's trajectory and hence obtain the momentum p . Combining E and p the particle(s) can be uniquely identified. Calorimeters are often made with scintillators interleaved with high-Z absorber/converter materials. The interactions in the calorimeter are characterized by the nuclear interaction length λ . It is the mean free path of a particle between two inelastic interactions. Numerically, $\lambda = \frac{A}{N_A \times \sigma \times \rho}$, where A , ρ are the atomic weight and density of the target, N_A is the Avogadro number, σ is the inelastic nuclear cross-section. λ differs for various particles as σ is different for different particle interactions with the calorimeter material. There are mainly two categories of Calorimeters used in particle physics: Electromagnetic Calorimeter (ECAL) and Hadronic Calorimeter (HCAL). An electromagnetic calorimeter is generally used to measure the energy of photons and electrons, whereas HCAL measures the energy of hadrons. In CMS, both detectors are made of scintillating crystal that acts as an active material as it absorbs the energy of the incident particle. This scintillator is sandwiched with a readout channel which is placed at the back end of the scintillator. A larger volume is necessary for the hadronic shower as it takes a larger distance between nuclear interaction. Hence HCAL is larger in dimension relative to ECAL. The CMS detector in LHC uses both ECAL and HCAL and more details of it are discussed in section 3.5.3-3.5.4.

3.3 The Large Hadron Collider

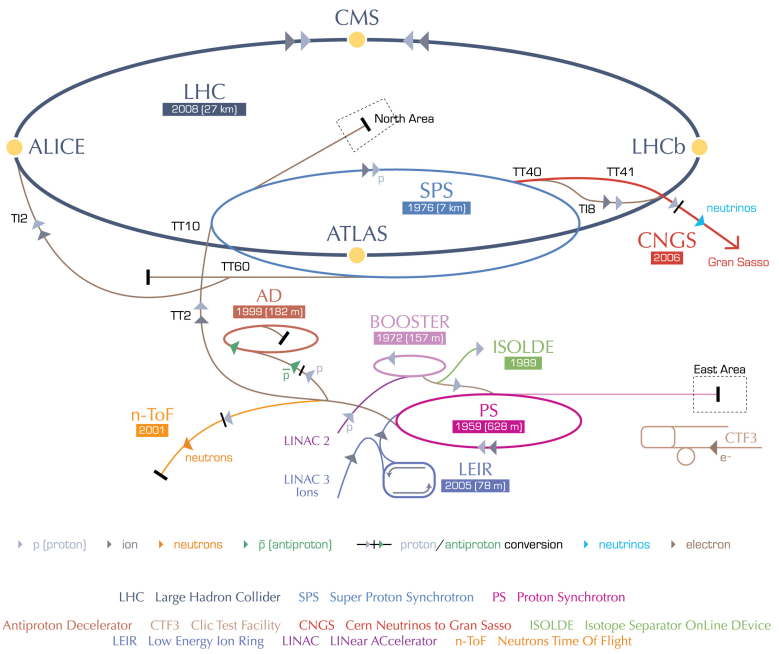
The Large Hadron Collider (LHC) is the world's largest and highest energy particle accelerator built to date. The LHC is operated at the European Organization for Nuclear Research (CERN) near Geneva, Switzerland. The collider is built in a circular tunnel that was previously used by the Large Electron-Positron Collider (LEP) [61], with a circumference of 27 km and resides within 45-170 m underground. The LHC collides hadrons (protons or heavy ions), accelerating them in opposite directions to near the speed of light and then smashing the particles

together. The energy loss per revolution of an accelerated charged particle (Ze) of mass m due to synchrotron radiation is

$$\Delta E \propto \frac{(Ze)^2}{R} \left(\frac{E}{m}\right)^4 \quad (3.8)$$

Where R is the radius of the circular orbit [62]. The energy loss due to synchrotron radiation is more for electron/positron relative to proton or heavy-ion as $m_{p/A} > m_{e^-/e^+}$. Hence, energy loss due to synchrotron radiation is more for the LEP relative to the LHC. Therefore, LHC is more beneficial relative to LEP in order to maintain constant beam energy. A schematic view of the CERN accelerator complex is shown in Fig. 3.12. Initially, acceleration takes place in

CERN's accelerator complex



European Organization for Nuclear Research | Organisation européenne pour la recherche nucléaire

© CERN 2008

Figure 3.12: A schematic view of the CERN accelerator complex.

different stages before injection of the beam in LHC. Electrons of hydrogen gas are stripped away to produce protons that undergo acceleration in the presence of an intense electric field at Linear Accelerator (LINAC 2) and gain energy up to 50 MeV. After that proton beam is injected into the Proton Synchrotron Booster (PSB) and energy is boosted up to 1.4 GeV. Then the beam is delivered to the Proton Synchrotron (PS) and energy reaches about 25 GeV. The beam again transferred to the large Super Proton Synchrotron (SPS). It has a circumference of 7 km and the

energy raises up to 450 GeV. At the last stage, the particle beam reaches the main LHC ring from SPS and is accelerated to the maximum energy of 6.5 TeV.

The LHC ring is not exactly in a circular shape. It consists of eight 2.45 km long arcs called octants and eight 545 m long rectilinear sections, shown in Fig. 3.13. Each arc consists of 154 superconducting dipole magnets operating at a magnetic field of 8.33 T to keep the beam focused. Beam injection in LHC takes place on Octant 2 and Octant 4. Two general-purpose

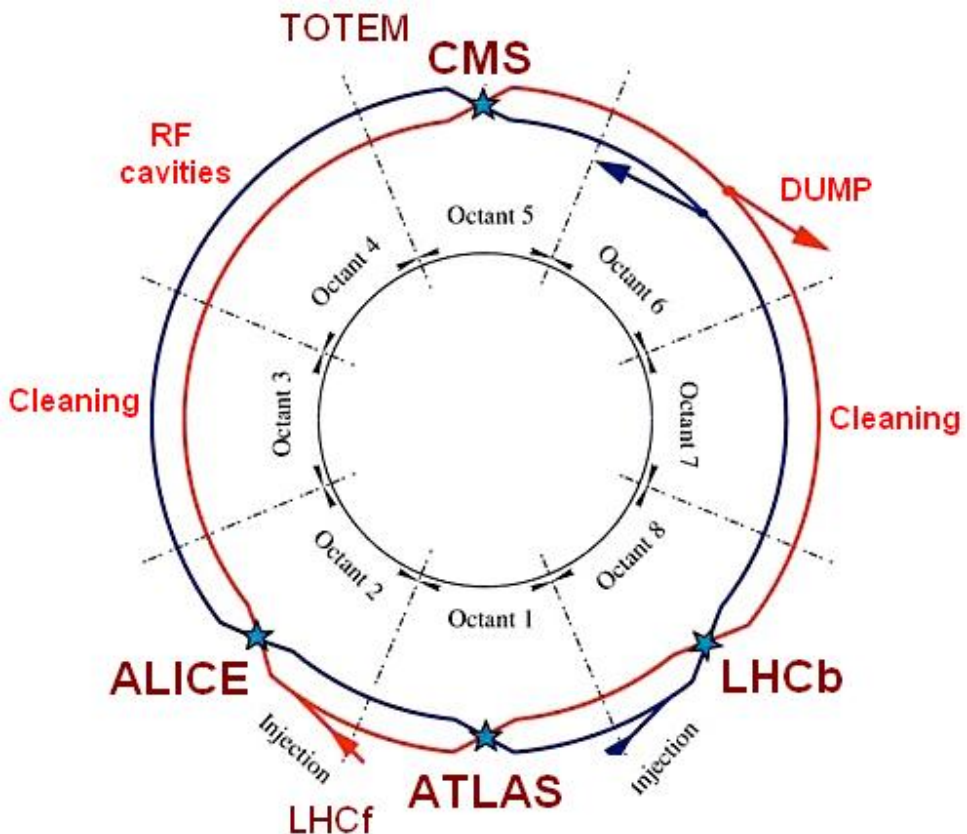


Figure 3.13: The structure of the LHC layout.

detectors A Toroidal Large hadron collider ApparatuS (ATLAS) and Compact Muon Solenoid (CMS) are deployed to do precision measurements within SM and look for new particles in BSM physics. ATLAS and CMS are placed in octant 1 and octant 5, respectively. Two other detectors, A Large Ion Collider Experiment (ALICE) and Large Hadron Collider beauty (LHCb) are located in octant 2 and octant 8. ALICE is specially designed to look for quark-gluon plasma in heavy-ion collisions. LHCb experiment is focused on the precision measurement of CP symmetry violation and b-quark related physics process.

3.4 LHC Luminosity

The number of events per unit time of a certain physics process is proportional to the cross-section σ of such process:

$$\frac{dN}{dt} = L_{inst} \sigma, \quad (3.9)$$

where proportionality constant L is the instantaneous luminosity of the collider. For head-on collision of two particle bunches (assuming Gaussian beam profile in all dimensions), the instantaneous luminosity can be written as

$$L_{inst} = \frac{f_{rev} N_1 N_2 n_b}{4\pi \sigma_x \sigma_y} \quad (3.10)$$

where f_{rev} is the revolution frequency, N_1 and N_2 are the number of particles per bunch, n_b is the number of bunches per beam, and σ_x/σ_y is the rms beam size in the transverse direction. Due to different beam characteristics and non-zero crossing angle of the LHC beam, the modified formula is

$$L_{inst} = \frac{f_{rev} N_1 N_2 n_b \gamma_r}{4\pi \epsilon_n \beta^*} F \quad (3.11)$$

where F is geometric luminosity reduction factor, γ_r relativistic gamma factor. Here beam width is expressed in terms of normalized transverse beam emittance, ϵ_n and the amplitude function at the collision point, β^* (i.e. $\sigma_{x,y} = \sqrt{\epsilon \cdot \beta_{x,y}/\gamma_r}$).

New particle searches or any statistical precision measurement require a large statistical number of events. We could get it at high luminosity or keep the luminosity low for a longer time as

$$N_{Events}^{obs} = \sigma \times \epsilon \times \int L_{inst} \cdot dt, \quad (3.12)$$

where σ is the cross-section of the rare process, ϵ is the efficiency of detection of the experiment. Cumulative luminosity versus day delivered during pPb run in 2016 is shown in Fig. 3.14. Since L is inversely related to the beam size, reducing the beam size (equivalent to increasing

proton density) can increase luminosity or N_{Events}^{obs} . The barn ($1 \text{ barn} = 10^{-24} \text{ cm}^2$) is the standard unit for measuring a nuclear cross-section (denoted as σ). The unit of luminosity is barn^{-1} since $N = \sigma \times L$ (from Eq. 3.11), where N is dimensionless quantity.

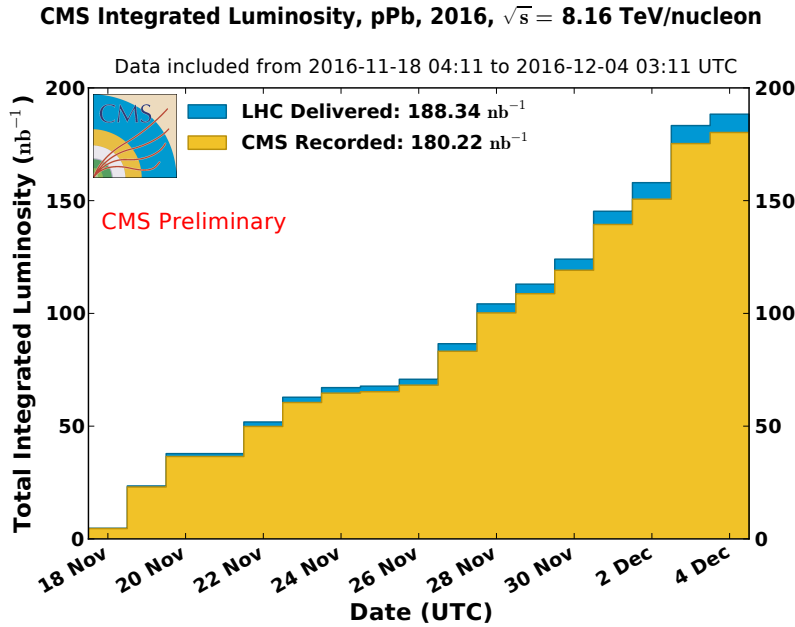


Figure 3.14: The cumulative delivered and recorded luminosity versus day for pPb, 2016 run.

3.5 The Compact Muon Solenoid

The CMS detector is one of the multipurpose detectors at the LHC, installed in a cavern about 100 m underground near Cessy in France. The CMS detector is of cylindrical shape, symmetric w.r.t beam pipe, and centered at the point of beam collision. It consists of different multiple layered cylindrical detecting components, co-axial along the beam direction, called barrel region, and closed by disks at both ends called endcap region. CMS weighs approximately 12500 tons, with a length of 21.6 m and a diameter of 14.6 m. Fig. 3.15 shows a schematic view of the CMS detector and its various components.

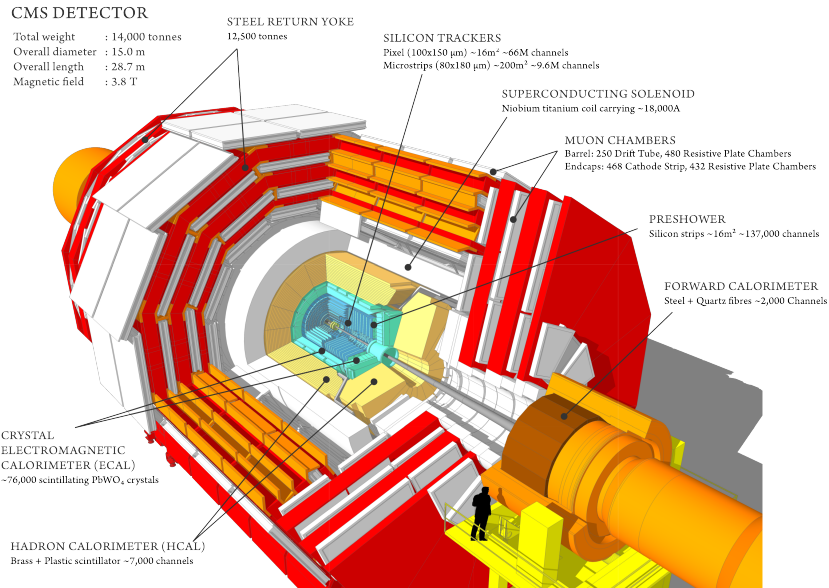


Figure 3.15: A schematic view of the CMS detector [63].

3.5.1 CMS Coordinate System

CMS uses a right-handed coordinate system with the origin at the collision point. In this coordinate system, the X-axis is pointed towards the center of the LHC collider, the Y-axis is pointed upwards and the Z-axis is pointed along the anticlockwise direction of the proton beam. Due to the cylindrical symmetry of the detector, it is convenient to use cylindrical coordinates (r , θ , z). Where r is the radius (i.e. $r = \sqrt{x^2 + y^2}$) in x-y plane and polar angle θ is the angle formed with +z direction in r -z plane. In case of cylindrical to spherical coordinate transformation, z is replaced by ϕ , where ϕ is the azimuthal angle in the x-y plane. In relativistic particle physics, it

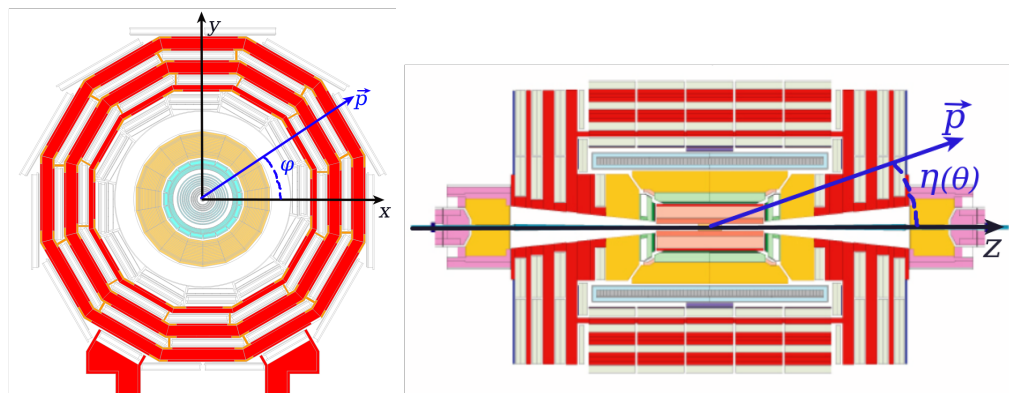


Figure 3.16: A schematic view of the CMS coordinate system [63, 64].

is crucial to use a Lorentz invariant quantity. Hence, for a boosted system along the $+z$ direction, we use a Lorentz invariant quantity called rapidity y . It is defined as

$$y = \frac{1}{2} \ln \frac{E + p_z}{E - p_z} \quad (3.13)$$

where E is the energy of the particle and p_z is the z -component of particle three-momentum \vec{p} . The difference between the rapidities of two particles is invariant under boosts along the Z -axis. For mass-less particles rapidity, y reduces to pseudorapidity η and is defined in terms of polar angle θ as

$$\eta = -\ln(\tan \frac{\theta}{2}) = \frac{1}{2} \ln \frac{|\vec{p}| + p_z}{|\vec{p}| - p_z} = \tanh^{-1} \frac{p_z}{|\vec{p}|}. \quad (3.14)$$

3.5.2 CMS Tracker System

The silicon tracker is the innermost detector of CMS and is placed nearest to the interaction point. It is specially designed for the precise determination of the trajectory of charged particles in presence of a magnetic field, and to reconstruct the primary and secondary vertices of the event. The silicon tracker is 5.8 m long with a diameter of 2.5 m and covers the range of $|\eta| < 2.5$, as can be seen in Fig. 3.17

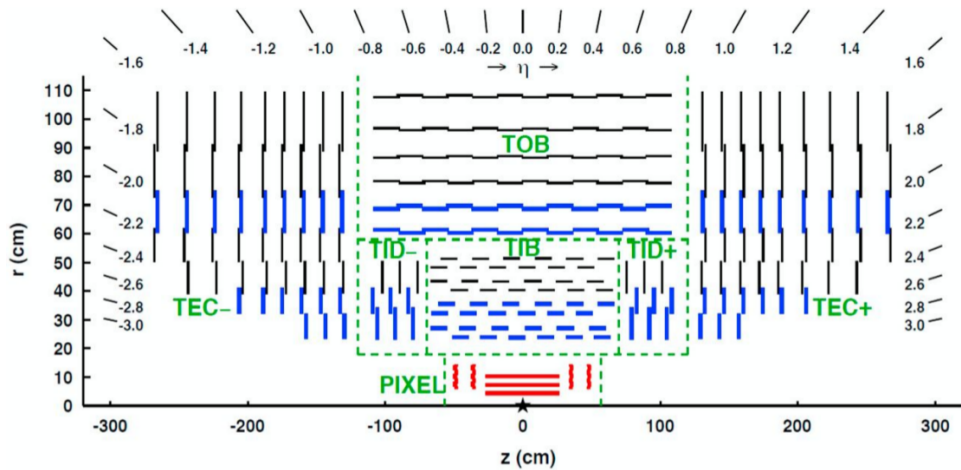


Figure 3.17: A schematic overview of the CMS tracker system.

It consists of two different sections, the pixel tracker (PIXEL) and the strip tracker. The pixel tracker is the closest to the beam pipe consisting of 3 co-axial barrel layers (BPIX) and closed by 2 end-cap disks (FPIX) on each side of the barrel. These cylindrical layers of BPIX are arranged at radii 4.4, 7.2, and 10.2 cm from the beamline. Endcap disk (FPIX) are located at $z = 34.5$ cm and $z = 46.5$ cm with radius from 6 to 15 cm. The BPIX and FPIX have 48×10^6 pixels and 18×10^6 pixels, respectively.

The strip tracker is located outside the pixel tracker and contains 9.3×10^6 strips. The silicon strip tracker consists of 4 tracker inner barrels (TIB) and 6 tracker outer barrels (TOB). The concentric TIB lies within the radius from 25.5 cm to 49.8 cm and cover the range $|z| < 70$ cm. The TOB is 218 cm long and radially extended from 55.5 cm and 116 cm. The TIB is closed by 3 tracker inner disks (TID) on each side of TIB and cover the range $80 < |z| < 90$ cm, whereas TOB is closed by 9 tracker end-caps (TEC) on each side of TOB and covers the range $124 < |z| < 280$ cm.

3.5.3 Electromagnetic Calorimeter

The Electromagnetic Calorimeter (ECAL) is designed to identify and measure the energy of photons, electrons, and positrons. The calorimeter is made of lead tungsten (PbWO_4) crystals. The ECAL is homogeneous and compact in shape along with fine granularity and radiation hardness properties. The crystal is the active material and as it absorbs the energy of the particle it will induce electromagnetic showers, and generate scintillation photons. The number of generated scintillation photons is proportional to the deposited energy of the particle. The scintillation photons are collected by a PMT as described earlier in the section on scintillator detectors. The PMT current signal is fed through an amplification electronics chain and finally digitized to be included as part of the recorded event data. In CMS, PbWO_4 scintillation crystal is used - it has a short scintillation time which permits the collection of about 80% of the light within 25 ns, which is the same as the time interval between LHC bunch crossing. This will reduce the pileup contribution. The ECAL consists of two parts, an ECAL barrel (EB) and 2 ECAL endcaps (EE). The barrel (EB) covers the region $|\eta| < 1.479$, while the endcap (EE) covers the range $1.479 < |\eta| < 3.00$, as shown in Fig. 3.18. The EB consists of 61200 crystals, while the EE has 7324 crystals. A pre-shower detector is placed in front of the endcap to dis-

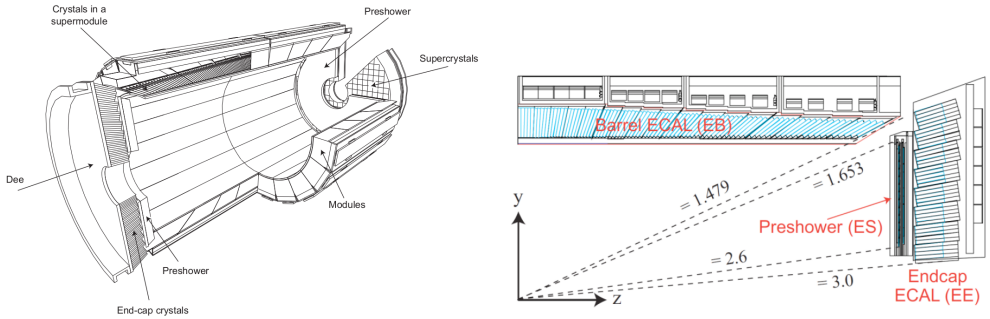


Figure 3.18: A view of ECAL detector in CMS and η coverage of ECAL components.

tinguish between photon and pion. It covers the range $1.65 < |\eta| < 2.6$. The energy resolution of ECAL has been measured with electron beams in the momentum range of 20 to 250 GeV, as shown in Fig. 3.19. The observed resolution of ECAL can be parametrized as

$$\left(\frac{\sigma_E}{E}\right)^2 = \left(\frac{N}{E}\right)^2 + \left(\frac{S}{\sqrt{E}}\right)^2 + C^2, \quad (3.15)$$

where N represents the noise term, S is the stochastic term, and C is the constant term. The noise term N takes into account the electronic noise and the pile-up events contribution. The total number of proton-proton interactions per bunch crossing is known as pileup. The stochastic term is dominant at low energies and accounts for the contribution of statistical fluctuations in the number of photo-electron collections. The last term C is a constant and is dominant at high energies. It includes the contribution of longitudinal non-uniformity of the crystal and energy scale calibration errors.

3.5.4 Hadronic Calorimeter

The Hadronic Calorimeter (HCAL) is located outside ECAL and inside the solenoid ($1.77 \text{ m} < r < 2.95 \text{ m}$). To measure jet energy and missing transverse energy in an event, it's employed as a complement to the ECAL. A jet is a cascade of particles produced from a very energetic quark or gluon in a particle physics or heavy-ion experiment. The energy imbalance in the plane transverse to the colliding particle beams is referred to as missing transverse energy. Such imbalance occurs when a particle escapes outside of the detector acceptance region or the

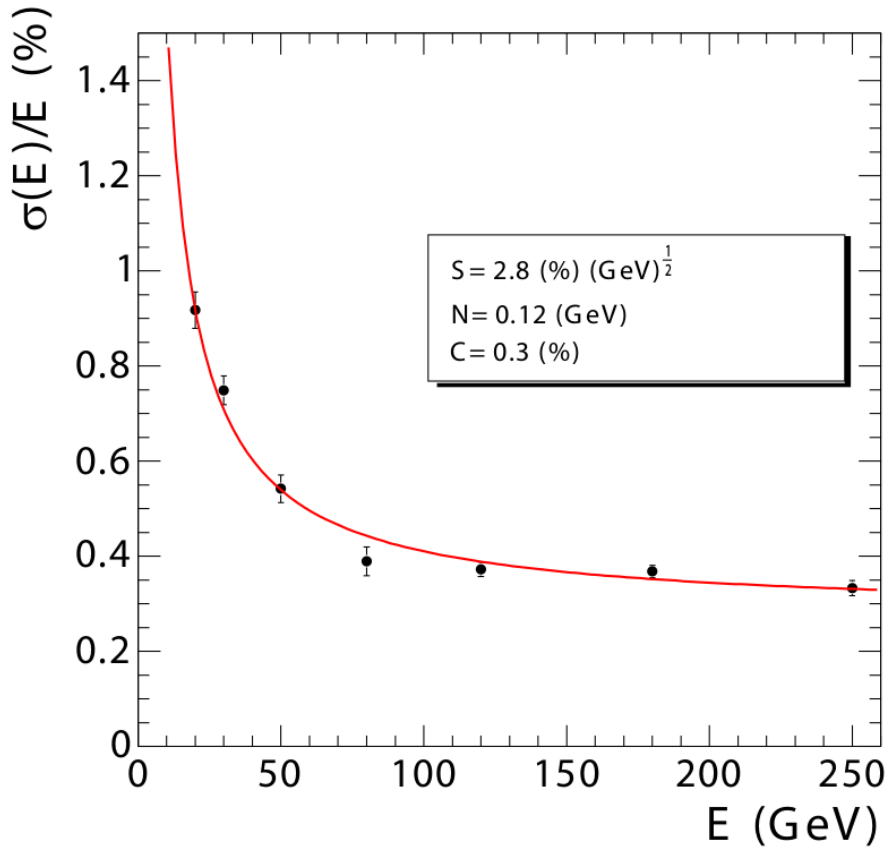


Figure 3.19: ECAL energy resolution (σ/E) as a function of the electron energy [65].

particle is not detectable. The HCAL is comprised of 4 sub-detectors: the HCAL inner barrel

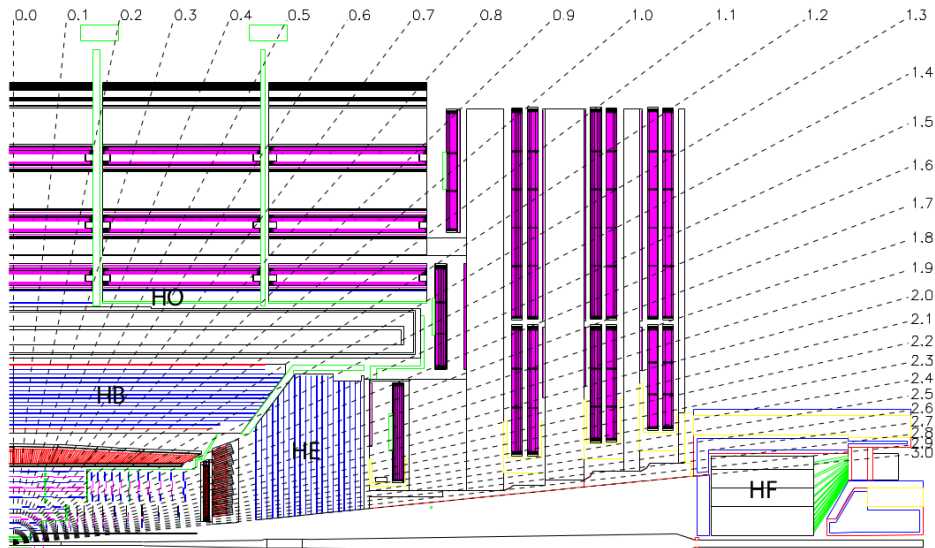


Figure 3.20: Longitudinal view of the CMS HCAL detector [65].

(HB), the HCAL outer barrel (HO), two HCAL endcaps (HE), and two forward calorimeters (HF), as shown in Fig. 3.20. Both HB and HO are covering the pseudorapidity region $|\eta| < 1.3$. The HE is placed behind the EE and covers the region $1.3 < |\eta| < 3.0$. The HF is placed close to the beam pipe in the very forward region ($3.1 < |\eta| < 5.2$). The HF plays the most crucial role in this analysis, because of its application in triggering non-hadronic events. Non-hadronic event means there is no nuclear/nucleon dissociation event like exclusive Υ photo-production (Fig. 2.2a) in pPb collision. The HB, HO, and HE are made of alternating layers of brass absorbers and plastic scintillators. The scintillator is connected to the hybrid photodiode via wavelength-shifter optical fibers to read out the scintillation light. HF consists of steel absorbers and quartz fibers as the active medium for resisting high radiation. The HCAL resolution can be parameterized by noise (N), stochastic (S) and constant (C) terms as

$$\left(\frac{\sigma_E}{E}\right)^2 = \left(\frac{N}{E}\right)^2 + \left(\frac{S}{\sqrt{E}}\right)^2 + C^2. \quad (3.16)$$

3.5.5 Magnet

The superconducting magnet is deployed between the HCAL and the muon system. The distinctive features of the superconducting magnet are to distinguish between positive, negative and neutral particles. It is used to bend the tracks of charged particles and to measure the momentum of all produced charged particles in a collision. The transverse momentum of a charged particle in a magnetic field can be written as

$$p_T = 0.3RB, \quad (3.17)$$

where p_T is the momentum of a charged particle, R is the radius of the track curvature of the charged particle and B is the magnetic field. Fig. 3.21 shows the CMS superconducting magnet. It has an inner diameter of 6 m and a length of 12.5 m. It can reach a maximum of 4 T field by operating it at 19.14 kA current.

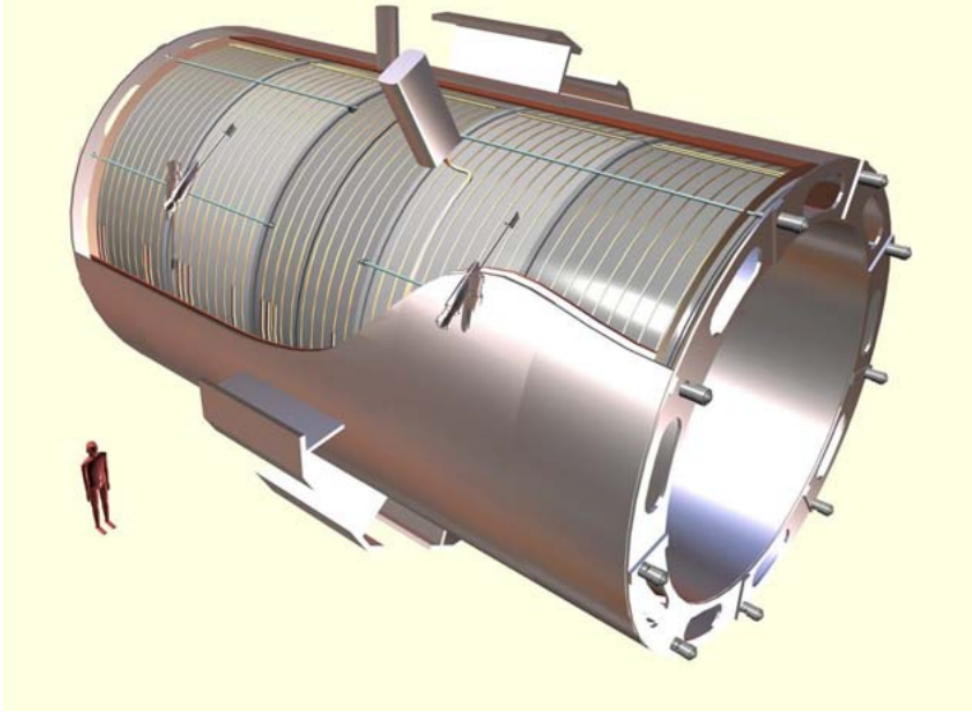


Figure 3.21: An artistic view of CMS superconducting magnet having 5 modules [65].

3.5.6 Muon System

CMS is well known for its excellent muon detection system. The muon system is the outermost detector of CMS as the muon is very penetrating. It is specially designed to identify and measure the momentum of muon by combining the hit information with the tracker. It consists of 3 sub-detectors: muon drift tubes (DT), cathode strip chambers (CSC), and resistive plate chambers (RPC). The layout of the muon system is shown in Fig. 3.22.

The DT chambers cover the barrel region with $|\eta| < 1.2$ and radially extended from 4.0 m to 7.0 m. There is a total of 250 drift tube chambers placed into 4 concentric cylinder stations around the beamline and interspersed in the layers of the iron yoke. Each station contains a gas mixture of Ar (85%) + CO₂ (15%) surrounding a gold-plated stainless-steel anode wire. Fig. 3.23 shows a schematic view of a drift tube chamber. When a muon passes the tube it ionizes the gas. Then electrons get drifted in presence of an electric field to an anode wire and produce a signal, which results in a drift time of 380 ns. The resolution of a station is 100 μm in both r- ϕ and r-z direction.

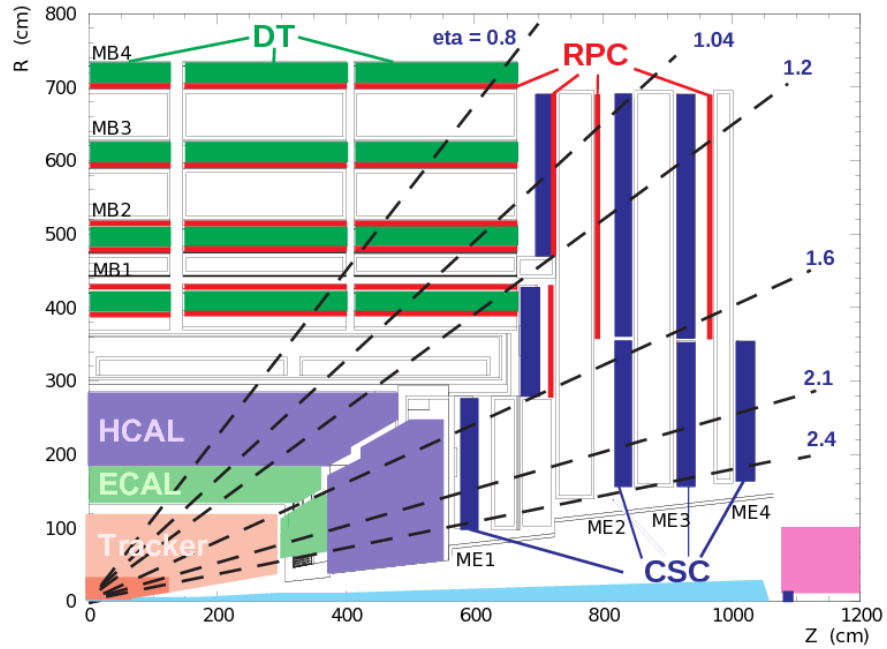


Figure 3.22: A schematic view of a quadrant of muon system [66].

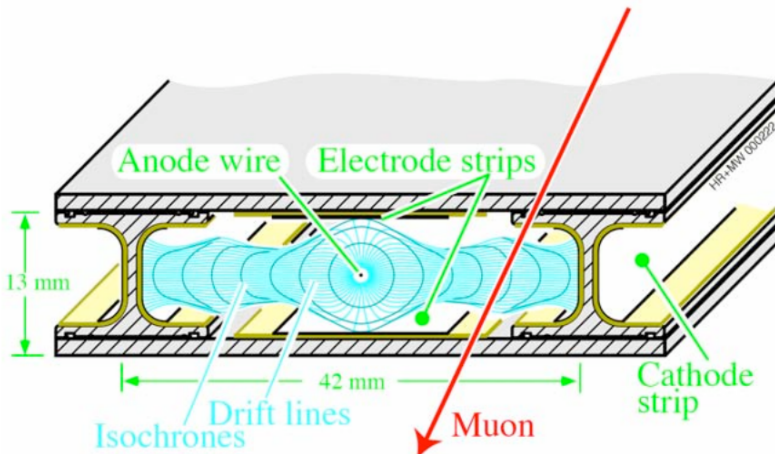


Figure 3.23: A schematic view of a drift tube [65].

The cathode strip chambers are placed in end-cap region with $0.9 < |\eta| < 2.4$. There are 234 CSC chambers placed in 4 stations on each side of the two end-caps, separated by the flux return plates of the superconducting magnet and arranged perpendicularly to the beam pipe. CSCs are multi-wire proportional chambers with a trapezoidal shape. Each CSC chamber consists of 6 anode planes interleaved among 7 cathode panels. The chambers are filled with a gas mixture of CO₂ (50%), Ar (40%) and CF₄ (10%). It also ionizes the gas when muon traverses through the chamber. Then an avalanche of electrons is generated in presence of the

strong electric field in the gap. It produces a signal on anode wires and induces a charge on the cathode strips. The spatial resolution of CSC is about 80 - 85 μm .

The RPC chambers are made of 4 bakelite planes separated by 2 mm gap. The gap is filled with a gas mixture of $\text{C}_2\text{H}_2\text{F}_4$ (94.5%) and Isobutane. The RPC detector covers the region $|\eta| < 1.6$ and has detection mechanism similar to CSC. The RPC chamber has a fast response with good time resolution (less than 25 ns) which provides an independent triggering system for muons. Also, it has a good spatial resolution.

3.5.7 CASTOR

The Centauro And STrange Object Research (CASTOR) calorimeter is a forward detector placed at a distance $z = 14.37$ m from the interaction point. The CASTOR is a Cherenkov detector. It covers the pseudorapidity region $-6.6 < \eta < -5.2$. It is Segmented into 16-sectors

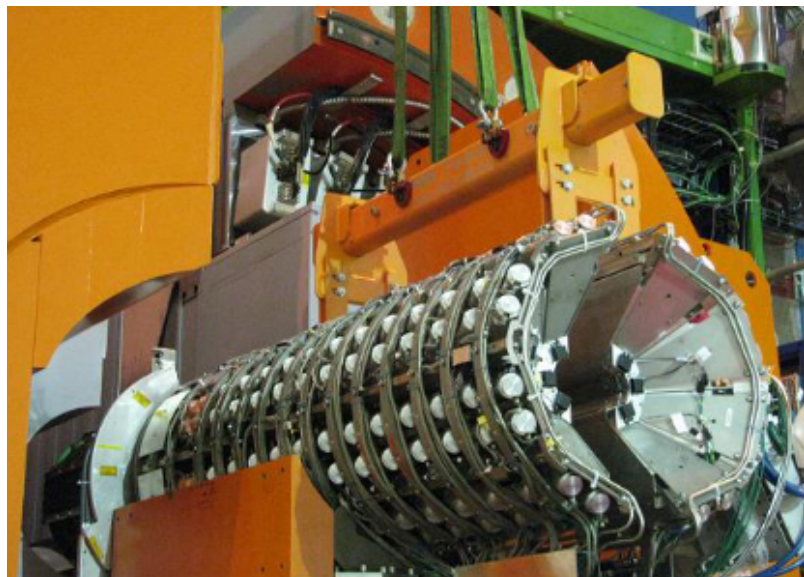


Figure 3.24: View of the CASTOR calorimeter [67].

in ϕ direction and 14-modules in-depth, resulting in 224 readout channels. Each module is composed of five tungsten absorber plates and five quartz plates, an air-light guide, and a PMT photo-sensor. The tungsten (quartz) plates have a thickness of 5 mm (2 mm) in the first two modules. For the remaining 12 modules, the thickness of the tungsten (quartz) plates is 10 mm (4 mm). The first two modules can detect electromagnetic showers and the remaining 12 mod-

ules are designed to detect hadronic showers. This detector is very useful for the forward jet study, diffractive measurement, and exclusive event selection.

3.5.8 Trigger

In LHC, bunches of the proton are separated by 25 ns resulting in a collision rate of about 40 MHz. It is not possible to store the data at such a high rate. Therefore, CMS uses a two-level trigger system for data collection. The first level of the CMS trigger system (L1) is composed of custom hardware processors. It uses information from the calorimeters and muon detectors to select the most interesting events associated with the final state particles of the analysis within a given bunch crossing and reduces the accepted events rate to about 100 kHz [68]. The high-level trigger (HLT) is designed to reduce the event rate further from 100 kHz to less than 1 kHz, before data storage [68]. The HLT uses a large number of processors to run physics algorithms. This algorithm can collect information from all CMS sub-detectors. The L1 trigger first makes the decision to select the event. At the same time, if the HLT accept condition is true, the HLT stores the data. In this analysis, we have used the UPC trigger and details of it are discussed in section 5.1.

Chapter 4

CMS data and MC simulation

4.1 Dataset

CMS acquires data using the data acquisition system. The data acquisition system is a complex chain of electronics that acquires analog electrical signals from the individual detector elements, digitizes and orders them, and forms a composite data block corresponding to signals recorded in every part of the detector from particles emitted in the primary collision of protons(or nuclei) at the center of the detector. This composite data block constitutes an ‘event’. As the data is processed in real-time, several selection criteria are also applied at various levels to selectively record events of interest for a particular measurement or set of measurements - these are called ‘triggers’. In order to identify blocks of events where specific trigger criteria have been applied, or the experiment was operated under special conditions, the data recorded to disk is further segmented into ‘runs’. For each run, all the meta-data like trigger conditions applied, active detector components, accelerator beam status etc are recorded. Reconstruction algorithm are then applied to obtain particle information (e.g. p_T) from the raw data signals (e.g. counted photo-electrons).

The prompt reconstructed (RECO) Analysis Object Data (AOD) datasets of proton-lead collisions (pARun2016C), namely "PAForward/PARun2016C-PromptReco-v1/AOD" have been used in the analysis. PromptReco AOD refers to the dataset type immediate reconstruction and the file format structure in AOD. AOD data is a subset of the RECO DATA. In AOD, information of physics objects is stored in a compact format and convenient for physics analyses. The data have been reconstructed in the CMSSW version CMSSW_8_0_26_patch2 with global tag "80X_dataRun2_Prompt_v15". CMSSW is an acronym for ‘**CMS** Soft**W**are framework. It is a collection of ROOT based libraries and analysis codes that is used to process and analyze data collected by CMS. (ROOT = **R**ene’s **O**bject **O**riented **T**oolkit, after the first author Rene Brun who originally started developing ROOT in 1995, though now the community has many thousands of contributors) The global tag contains information on detector health conditions during the proton-lead run.

The data sets used in this analysis include runs 285479- 285832, and 285956- 286496 correspond to 173.4 nb^{-1} of pPb collisions recorded by the CMS experiment in 2016, with beam energies of 6.5 TeV for the protons and 2.56 TeV per nucleon for the lead nuclei, resulting in a center-of-mass energy per nucleon-nucleon pair of $\sqrt{s_{NN}} = 8.16 \text{ TeV}$. The data comprise two subsets: the pPb sample, with the Pb ion going in $+z$ beam direction, corresponding to an integrated luminosity of 62.6 nb^{-1} , and the Pbp sample, with the Pb ion going in the $-z$ direction, corresponding to an integrated luminosity of 110.8 nb^{-1} .

4.2 Monte Carlo Samples

The STARLIGHT [69, 70] Monte Carlo (MC) event generator is used to simulate exclusive $\Upsilon(nS)$ photo-production events (Fig. 2.2, left) and the exclusive QED background (Fig. 2.2, right). A MC event generator is a program that simulates particle physics events produced in particle collider experiments. People use this widely to make predictions or comparisons with experimental results and preparations for future experiments. STARLIGHT assumes that the photon flux from the incoming hadron(s) is described by the Weizsäcker-Williams Equivalent Photon Approximation [71, 72], and uses an empirical fit of the exclusive VM photo-production cross-sections to the existing HERA γp data.

In the $\Upsilon(nS)$ sample two contributions are simulated, with the photon being emitted either from the Pb ion or from the proton. The events where the photon is emitted from the Pb ion, $pPb \rightarrow (\gamma p) \rightarrow pPb\Upsilon(nS)$, constitute the signal, while the small fraction of events with the photon emitted from the proton, $pPb \rightarrow (\gamma Pb) \rightarrow pPb\Upsilon(nS)$, is treated as background. The signal events in STARLIGHT are simulated assuming an exponential dependence on the four-momentum transfer squared at the proton vertex, $\exp(-b|t|)$ with $b = 4 \text{ GeV}^{-2}$, and a power-law dependence of the cross section on the photon-proton center-of-mass energy, $(W_{\gamma p})^\delta$ with $\delta = 1.7$, as determined from HERA data [41, 42]. Table 4.1 shows the cross-section for three Upsilon states for γp and γPb and QED background estimated from STARLIGHT.

The simulated events are passed through the GEANT4-based [73] detector simulation, and the event reconstruction chain of CMS. Figs. 4.1, 4.2, 4.3 and 4.4, 4.5, 4.6 show the generated and reconstructed muon p_T^μ , η_μ and ϕ_μ and muon pair $p_T(\mu^+ \mu^-)$, rapidity ($y_{\mu^+ \mu^-}$) and invariant mass ($m_{\mu^+ \mu^-}$) distributions, respectively, for γp , γPb and QED processes.

The backgrounds from inclusive and semi-exclusive Υ and dimuon production processes are obtained using data-driven templates as explained in Section 8.

Generated muons are produced in full phase space. But we have applied offline reconstructed muon selection cuts, which are discussed in Section 5.2.

Table 4.1: Cross-sections for Upsilon photo-production in pPb collisions at $\sqrt{s} = 8.16 \text{ TeV}$ from STARLIGHT.

Process	$\sigma(\text{nb})$
$pPb \rightarrow (\gamma p) \rightarrow p\Upsilon(1S)Pb \times \text{BR}[\mu^+ \mu^-]$	5.35 nb
$pPb \rightarrow (\gamma p) \rightarrow p\Upsilon(2S)Pb \times \text{BR}[\mu^+ \mu^-]$	1.87 nb
$pPb \rightarrow (\gamma p) \rightarrow p\Upsilon(3S)Pb \times \text{BR}[\mu^+ \mu^-]$	1.52 nb
$pPb \rightarrow (\gamma Pb) \rightarrow p\Upsilon(1S)Pb \times \text{BR}[\mu^+ \mu^-]$	0.39 nb
$pPb \rightarrow (\gamma Pb) \rightarrow p\Upsilon(2S)Pb \times \text{BR}[\mu^+ \mu^-]$	0.13 nb
$pPb \rightarrow (\gamma Pb) \rightarrow p\Upsilon(3S)Pb \times \text{BR}[\mu^+ \mu^-]$	0.11 nb
$pPb \rightarrow (\gamma\gamma) \rightarrow p\mu^+ \mu^- Pb, m_{\mu^+ \mu^-} : (8 - 20) \text{ GeV}$	332 nb

Fig. 4.1 shows the generated single muon p_T^μ distribution for signal events that fall roughly between 0 and 6 GeV. Also, it indicates that the muon reconstruction efficiency is poor in the

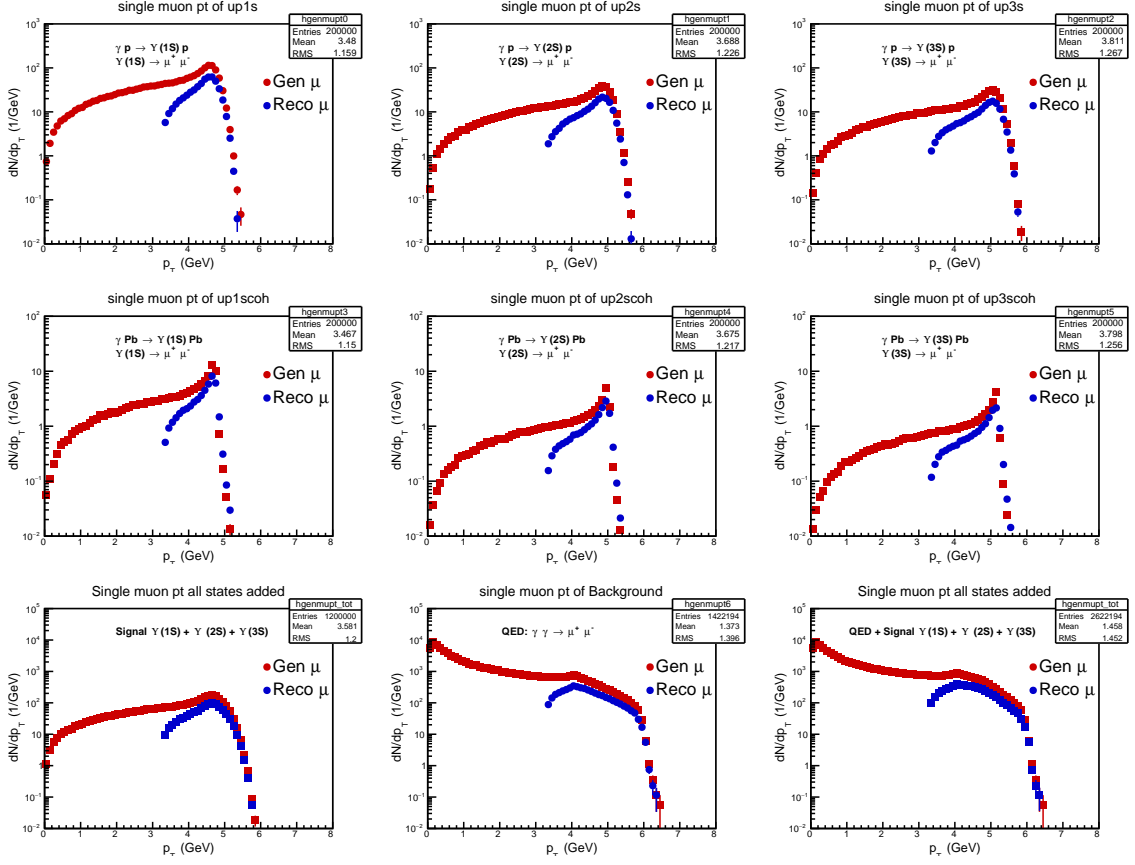


Figure 4.1: Generated and reconstructed distributions of muon p_T^μ for $\gamma p \rightarrow Y(nS)p$ (upper panel), $\gamma Pb \rightarrow Y(nS)Pb$ (middle panel), signal: sum of $\gamma p \rightarrow Y(nS)p$ and $\gamma Pb \rightarrow Y(nS)Pb$ (left figure of lower panel), QED: $\gamma\gamma \rightarrow \mu^+ \mu^-$ (middle figure of lower panel) and sum of signal+QED (right figure of lower panel) processes within invariant mass range $8 < m_{\mu^+ \mu^-} < 12$ GeV. Red and blue dots represent generated and reconstructed distributions, respectively.

low $p_T^\mu < 3$ GeV region, as indicated by the reconstructed p_T^μ distribution, which is in the range of $p_T^\mu:3\text{-}6$ GeV. In Fig. 4.2, the single muon η_μ distribution is not symmetric w.r.t $\eta_\mu = 0$ as the atomic mass numbers (A) of colliding particles are different. We observed similar nature in the case of dimuon rapidity distribution (Fig. 4.5) also. The probability of getting a muon in any ϕ direction is the same. As a result, we get a flat distribution of ϕ (Fig. 4.3). Fig. 4.4 shows that signal and QED events are dominated in the low $p_T(\mu^+ \mu^-)$ region, and the highest accessible $p_T(\mu^+ \mu^-)$ is around 1.5 GeV. Furthermore, the dimuon invariant mass distribution (Fig. 4.6) shows $Y(1S)$, $Y(2S)$, and $Y(3S)$ peaks at 9.46 GeV, 10.02 GeV, and 10.36 GeV, respectively. All these plots imply that the reconstruction is sufficient for the analysis.

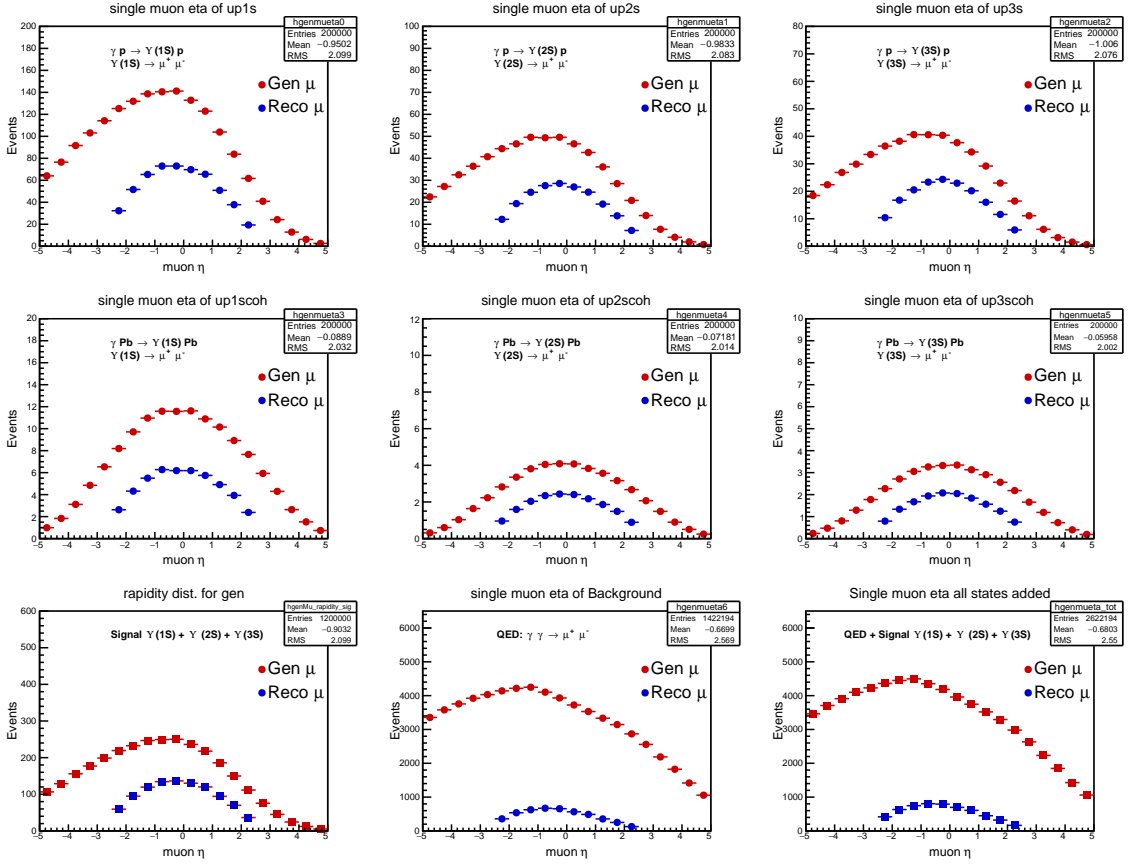


Figure 4.2: Generated and reconstructed distributions of muon η_μ for $\gamma p \rightarrow \Upsilon(nS)p$ (upper panel), $\gamma Pb \rightarrow \Upsilon(nS)Pb$ (middle panel), signal: sum of $\gamma p \rightarrow \Upsilon(nS)p$ and $\gamma Pb \rightarrow \Upsilon(nS)Pb$ (left figure of lower panel), QED: $\gamma\gamma \rightarrow \mu^+\mu^-$ (middle figure of lower panel) and sum of signal+QED (right figure of lower panel) processes within invariant mass range $8 < m_{\mu^+\mu^-} < 12$ GeV. Red and blue dots represent generated and reconstructed distributions, respectively.

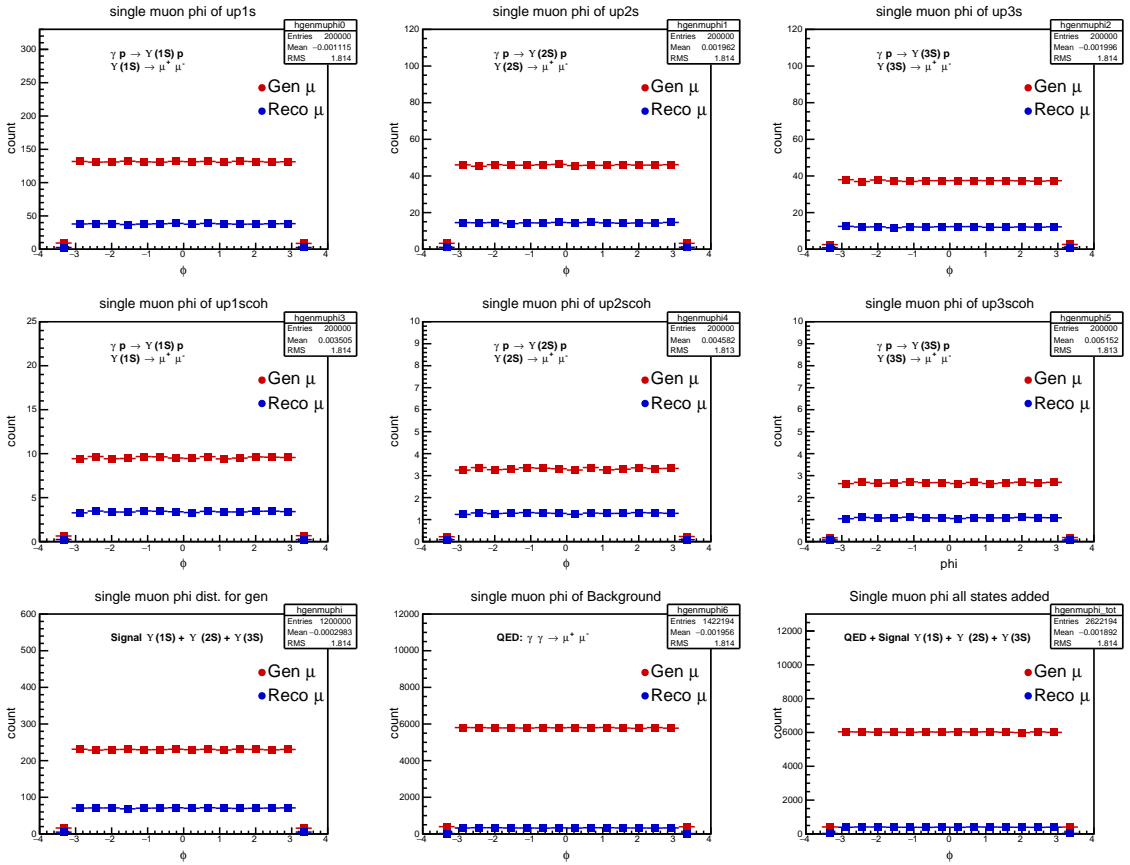


Figure 4.3: Generated and reconstructed distributions of muon ϕ_μ for $\gamma p \rightarrow \Upsilon(nS)p$ (upper panel), $\gamma Pb \rightarrow \Upsilon(nS)Pb$ (middle panel), signal: sum of $\gamma p \rightarrow \Upsilon(nS)p$ and $\gamma Pb \rightarrow \Upsilon(nS)Pb$ (left figure of lower panel), QED: $\gamma\gamma \rightarrow \mu^+ \mu^-$ (middle figure of lower panel) and sum of signal+QED (right figure of lower panel) processes within invariant mass range $8 < m_{\mu^+ \mu^-} < 12$ GeV. Red and blue dots represent generated and reconstructed distributions, respectively.

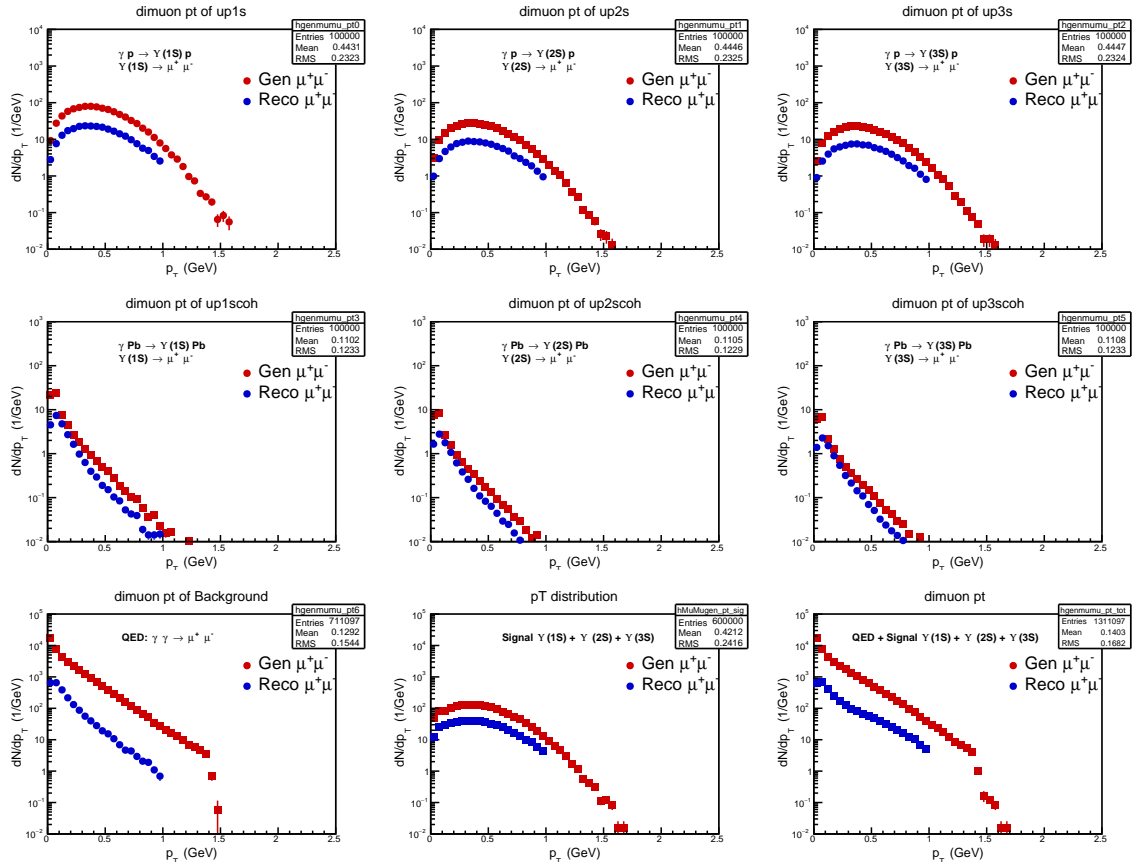


Figure 4.4: Generated and reconstructed distributions of muon pair $p_T(\mu^+\mu^-)$ for $\gamma p \rightarrow \Upsilon(nS)p$ (upper panel), $\gamma Pb \rightarrow \Upsilon(nS)Pb$ (middle panel), signal: sum of $\gamma p \rightarrow \Upsilon(nS)p$ and $\gamma Pb \rightarrow \Upsilon(nS)Pb$ (left figure of lower panel), QED: $\gamma\gamma \rightarrow \mu^+\mu^-$ (middle figure of lower panel) and sum of signal+QED (right figure of lower panel) processes within invariant mass range $8 < m_{\mu^+\mu^-} < 12 \text{ GeV}$. Red and blue dots represent generated and reconstructed distributions, respectively.

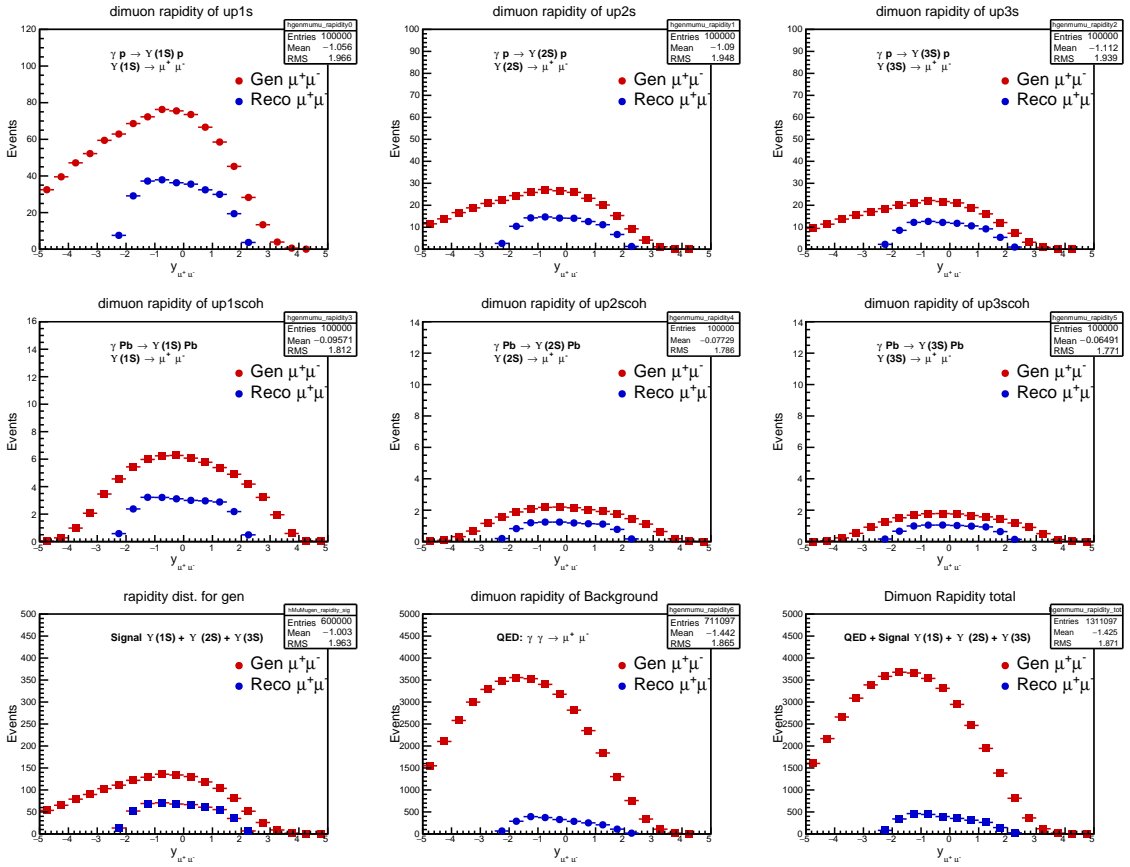


Figure 4.5: Generated and reconstructed distributions of muon pair rapidity for $\gamma p \rightarrow Y(nS)p$ (upper panel), $\gamma Pb \rightarrow Y(nS)Pb$ (middle panel), signal: sum of $\gamma p \rightarrow Y(nS)p$ and $\gamma Pb \rightarrow Y(nS)Pb$ (left figure of lower panel), QED: $\gamma \gamma \rightarrow \mu^+ \mu^-$ (middle figure of lower panel) and sum of signal+QED (right figure of lower panel) processes within invariant mass range $8 < m_{\mu^+ \mu^-} < 12$ GeV. Red and blue dots represent generated and reconstructed distributions, respectively.

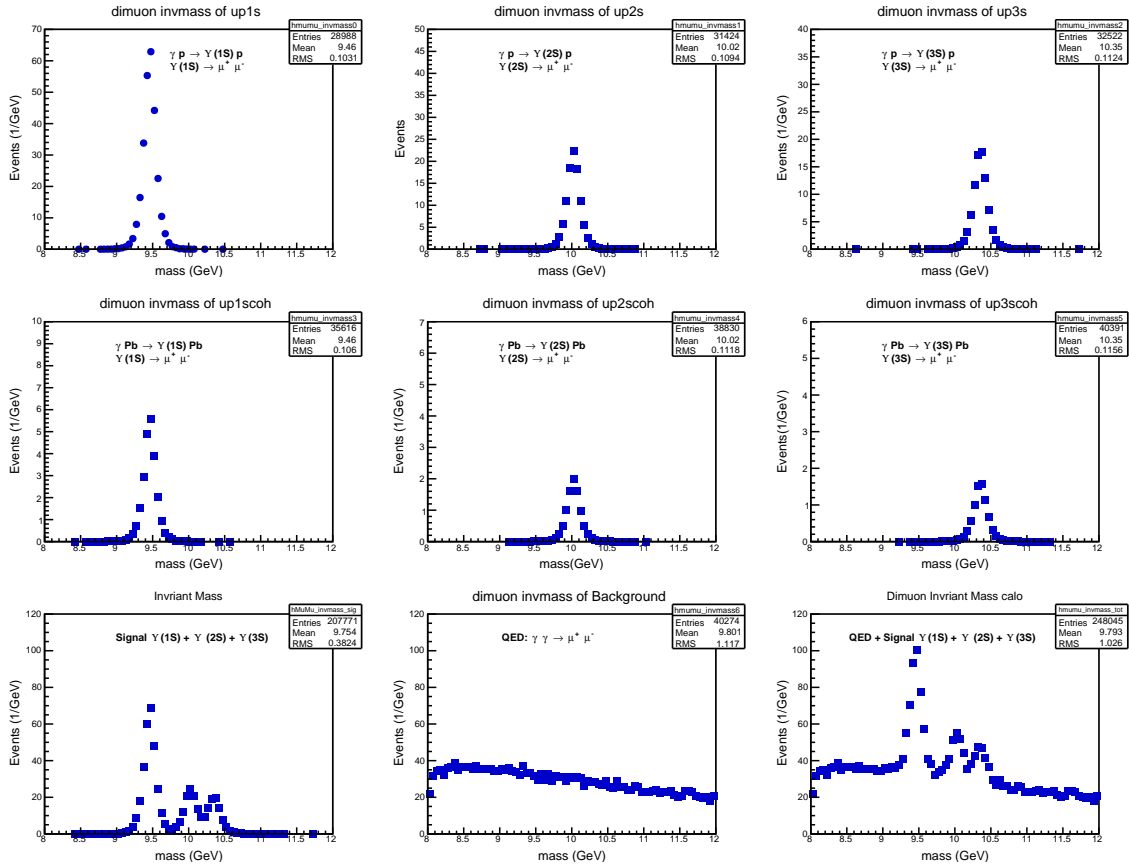


Figure 4.6: Reconstructed distributions of muon pair invariant mass for for $\gamma p \rightarrow \Upsilon(nS)p$ (upper panel), $\gamma Pb \rightarrow \Upsilon(nS)Pb$ (middle panel), signal: sum of $\gamma p \rightarrow \Upsilon(nS)p$ and $\gamma Pb \rightarrow \Upsilon(nS)Pb$ (left figure of lower panel), QED: $\gamma\gamma \rightarrow \mu^+\mu^-$ (middle figure of lower panel) and sum of signal+QED (right figure of lower panel) processes within invariant mass range $8 < m_{\mu^+\mu^-} < 12$ GeV. Blue dots represent reconstructed distributions.

Chapter 5

Event Selection

5.1 Trigger

The dataset is skimmed by requesting UPC dedicated HLT trigger path "HLT_PASingleMuOpen_HFOneTowerVeto_v1". It's a single muon trigger, seeded with L1_SingleMuOpen. "SingleMUOpen" denotes a single muon selection by requiring at least one hit in the muon chambers. "HFOneTowerVeto" refers to a veto applied on at least one side to have all HF towers below the optimised threshold to select UPC events by excluding hadronic activity in HF. The skimming and the root ntuples were created using the HIonka skimming used for the study of inclusive upsilon in pPb. The skim makes a HLT-based preselection of events and reduces the size of the datasets significantly. The root ntuple is tabular where each event consists of a fixed length row of data.

5.2 Muon selection

The $\Upsilon(1S, 2S, 3S)$ states are considered in their dimuon decay channel. The data sample was skimmed when requesting dedicated HLT UPC trigger bits and for events with two-tracker muons that pass the soft muon ID selection.

Muon candidates used in this analysis are accepted only if they belong to the following kinematic regions: $|\eta_\mu| < 2.2$ and $p_T^\mu > 3.3$ GeV. These cuts are applied following muon efficiency studies by Tag and Probe method [74]. The muon candidates are selected if reconstructed as tracker muons and passing the soft muon ID selection [75], as defined by the Muon POG. Below all quality cuts for muon selection are described:

- The number of valid tracker layers > 5 which indicates the quality of inner tracks;
- The number of pixel layers with valid hits > 0 ;
- The track high purity flag is used to reject bad quality tracks, which consists of a few outliers;
- The distance between the event vertex and the muon track in the transverse plane, $D_{xy} < 0.3$ cm, and the longitudinal plane, $D_z < 20.0$ cm, which indicates if the muon comes from decay in flight or is a prompt muon, and removes cosmic muons. A vertex is a point from which heavy particles (Ex. J/Ψ , Υ , etc.) start to decay. In this scenario, vertex referred to as decay point of Υ to $\mu^+ \mu^-$;
- TMOneStationTight (requires one well-matched segment in the muon stations for the track);

For the “`HLT_PASingleMuOpen_HFOneTowerVeto_v1`” trigger, the muon kinematic selection region is given below:

$$(|\eta_\mu| < 1.3 \& p_T^\mu >= 3.3), (1.3 <= |\eta_\mu| < 2.1 \& p_T^\mu >= 5.075 - 1.75 \times |\eta_\mu|), (2.1 <= |\eta_\mu| < 2.4 \& p_T^\mu >= 1.4).$$

5.3 Selection of exclusive Upsilon candidates

All selection cuts for exclusive Upsilon candidates are discussed below.

- Invariant mass cut: The muon pairs are selected within the invariant mass interval 8.0–12.0 GeV.
- Muon selection: In order to minimize the uncertainties related to the low- p_T muon efficiencies, muons with $p_T^\mu > 3.3$ GeV are selected in the pseudorapidity region $|\eta^\mu| < 2.2$.
- Exclusivity criteria: Exclusivity criteria are applied by selecting only dimuon events with a single vertex and no extra charged particles with $p_T > 0.1$ GeV associated to it.

With the above selection criteria, we will still get contamination of proton-dissociation events along with exclusive Υ . Fig. 5.1 shows the extra tower HF energy distribution for HF plus and HF Minus for pPb and Pbp runs after applying all event selection criteria. Fig. 5.2 and Fig. 5.3 show the extra tower HCAL and ECAL energy distribution respectively for pPb runs after applying all event selection criteria. In this analysis, we haven't applied any offline HF veto in the event selection criteria to exclude the proton-dissociation event.

Hence, we separately estimated the non-exclusive contribution in the data which satisfy the above Upsilon selection cuts.

- Dimuon selection: the rapidity of the muon pair is required to be in the region $|y| < 2.2$. Only events with the $p_T < 1$ GeV of the muon pair are considered, thereby reducing the contamination from Υ production in inclusive and semi-exclusive (where the proton dissociates into a low-mass hadronic system, called "proton dissociation") processes, that dominate the region of larger dimuon p_T .

A number of events after applying each event selection cut for pPb and Pbp collisions is shown in Table 5.1.

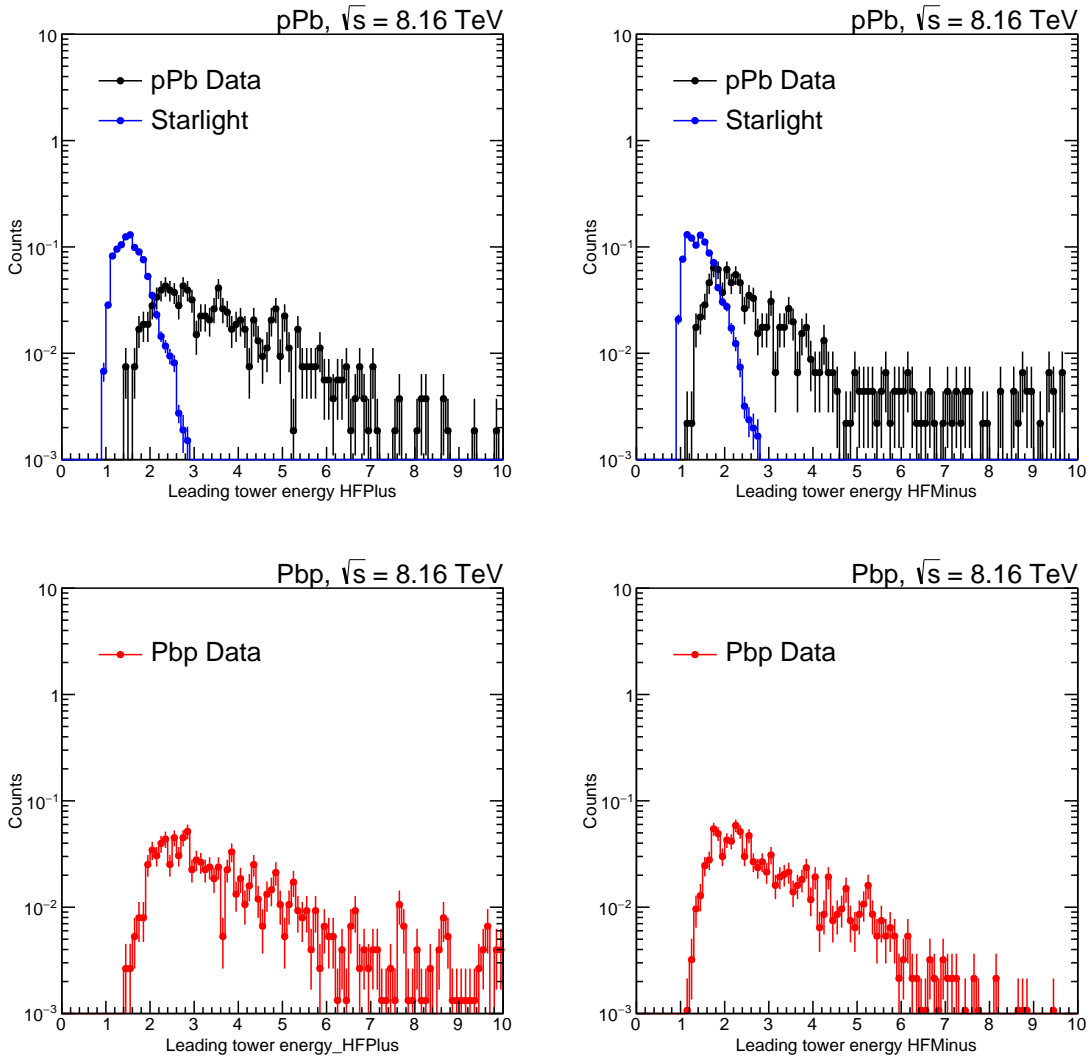


Figure 5.1: Extra tower HF plus and HF minus energy distributions for pPb and Pbp run.

5.4 Noise study

Noise study in different sub-detectors plays an important role in exclusive and proton-dissociation event selection. Hence, for such event selection, it is required that there should be no additional towers above noise thresholds in the calorimeters (EB, EE, HB, HE, HF and CASTOR). An additional tower in the calorimeters is defined as any tower above noise thresholds. In CMS, different calorimeters have different η and ϕ segmentation. Here, a tower is a collection of different layers of the calorimeter(s) that have the same value of η and ϕ . In a collision event,

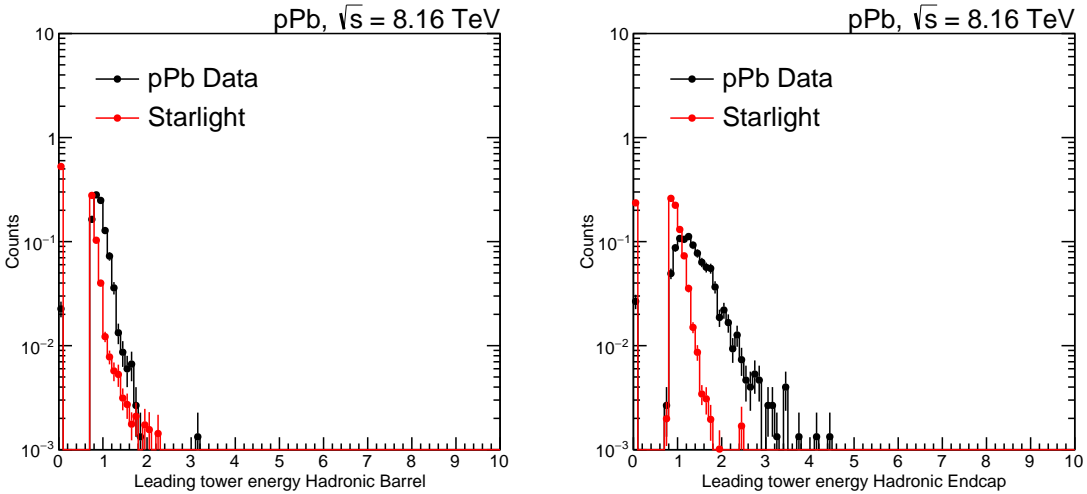


Figure 5.2: HB and HE leading tower energy distributions for Data and MC (STARLIGHT).

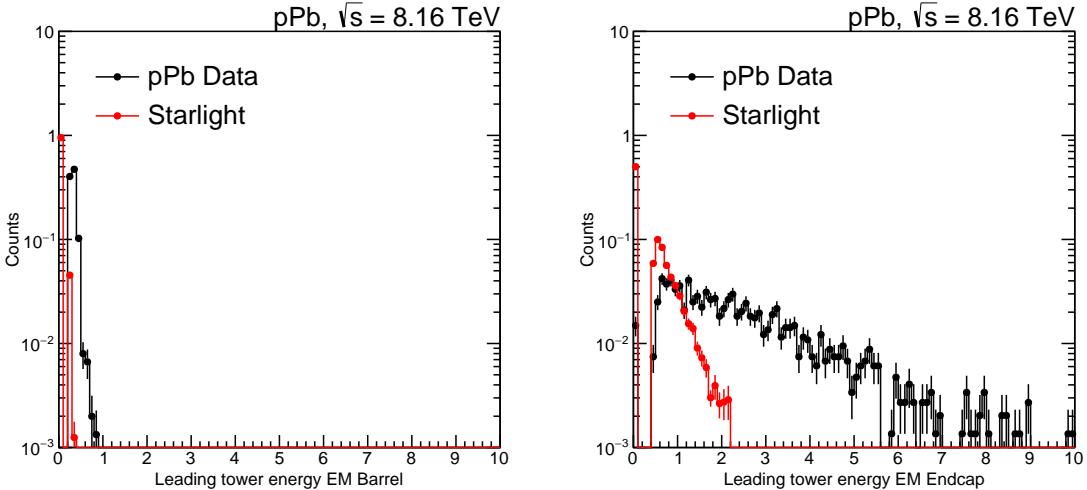


Figure 5.3: EM barrel and EM endcap leading tower energy distributions for Data and MC (STARLIGHT).

the leading tower energy is the highest energy of a calorimeter tower among all other towers.

The noise threshold for each calorimeter is determined using the single beam BPTX events. Since only one beam passes through the interaction point, no collisions occur in such events. Therefore a single-beam data set is very useful to study the noise distributions. These events were accessed by reconstructing the PAEmptyBX dataset, namely, “/PAEmptyBX/PARun2016C-PromptReco-v1/AOD”, collected by the CMS experiment in 2016.

Table 5.1: Statistics after each event selection cut for pPb and Pbp collisions at $\sqrt{s} = 8.16$ TeV

Cuts applied	No. of Muon pairs selected	
	pPb run	Pbp run
	Opposite sign	Opposite sign
HLT skimmed, Accepted, Reconstructed	3903297	6005060
nPV=1, $N_{Trk} = 2, M_{\mu^+\mu^-}$: 8-12 GeV	1886	3165
HLT single muon trigger	1885	3159
$p_T(\mu^+, \mu^-) > 3.3$ GeV	1607	2681
$p_T(\mu^+\mu^-) < 1$ GeV	1146	1922
$ \eta_{\mu^+, \mu^-} < 2.2, y_{\mu^+\mu^-} < 2.2$ GeV	1040	1758

Events are reconstructed by following the same reconstruction chain used for the exclusive Υ analysis. “HLT_PAL1BptxMinusNotBptxPlus_v1” (BPTX-) and “HLT_PAL1BptxPlusNotBptxMinus_v1” (BPTX+) were used for reconstruction. Also, we used zero bias data, namely, “/ZeroBias/PARun2016C-PromptReco-v1/AOD” for noise study in CASTOR. This zero bias data is a control data sample selected using the two beam pick-up monitors (installed at the opposite ends of CMS along the beam line) to detect the coincidence of two simultaneous signals caused by colliding bunches crossing. Zero bias data was skimmed with the HLT trigger “HLT_PAZeroBias_v1”.

Fig. 5.4 shows the leading tower energy distributions for BPTX+ and BPTX- events in the EB, EE, HB, HE, HF Plus, and HF Minus respectively. Fig. 5.5 shows the leading tower energy distributions for BPTX+, BPTX-, and zero bias events in the CASTOR. The noise threshold in each sub-detector is defined as the energy value at which we get 99% integral of the leading tower energy spectrum and specified in Table 5.2. In this analysis, we have used a 10 GeV threshold for HF $^\pm$, input was taken from a Two-particle correlation analysis at 8.16 TeV [76].

In case of a proton dissociation (PD) event, the energy deposition of the proton takes place in the forward detector(Ex. HF, CASTOR). In our analysis, we didn't use CASTOR as it is situated only in the -ve η region. So, we didn't use it. The HF noise threshold was used to make a data driven PD template ($N_{Track} = 2, HF_{Leadingtowerenergy} > 10$ GeV). We used this template to

Table 5.2: Thresholds in each sub-detector.

Sub-detector	eta range	Threshold
ECAL Barrel	$0 < \eta < 1.479$	0.5 GeV
ECAL Endcap	$1.479 < \eta < 3$	4.5 GeV
HCAL Barrel	$0 < \eta < 1.305$	1.5 GeV
HCAL Endcap	$1.305 < \eta < 3$	2.8 GeV
HF Plus	$3.1 < \eta < 5.2$	9.0 GeV
HF Minus	$-5.2 < \eta < -3.1$	7.0 GeV
CASTOR	$-6.6 < \eta < -5.2$	5.0 GeV

estimate PD contribution in the signal region. Details of PD estimation are described in sec. 8.3.

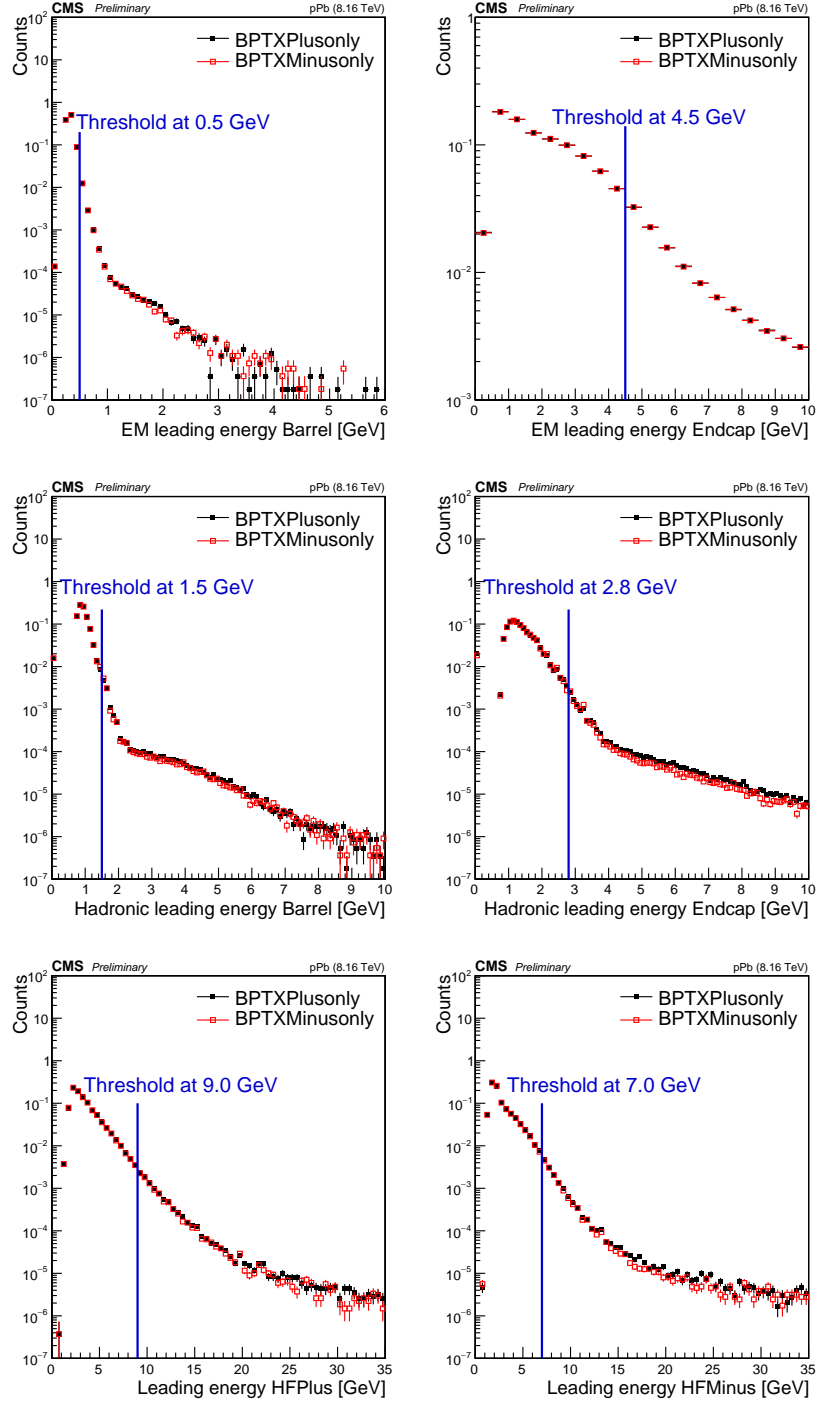


Figure 5.4: (Upper panel) Leading electromagnetic energy distribution in EB (left) and EE^\pm (right), (middle panel) leading hadronic energy in HB (left) and HE^\pm (right), (lower panel) leading energy distribution in HF plus (left) and HF minus (right) for pPb collisions at $\sqrt{s} = 8.16$ TeV Emptybx data. Thresholds are shown with vertical lines.

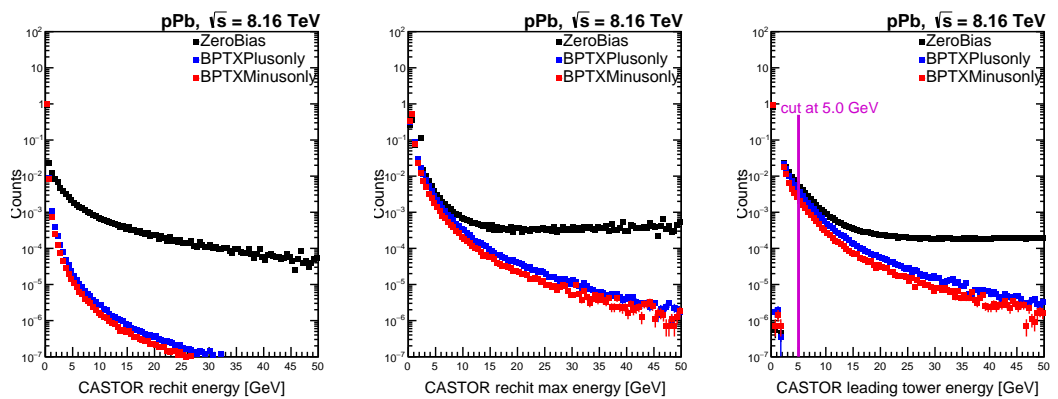


Figure 5.5: (left) CASTOR rechit energy distributions for Emptybx and ZeroBias data. (middle) CASTOR rechit max energy distributions for Emptybx and ZeroBias data. (right) CASTOR leading energy distributions for Emptybx and ZeroBias data. The threshold is shown with a vertical line.

Chapter 6

Muon efficiency using Tag and Probe method

Efficiency determines whether the detector will respond to the particle passage sufficiently to enable detection. Actually, efficiency accounts for reconstruction and identification losses. Accurate knowledge of the efficiency for kinematic selections of objects (muons in this analysis) plays a crucial role in cross-section measurements. The MC simulation results are not entirely reliable due to inaccuracies in the detector response modelling. In light of this, we need to evaluate correction factors, namely scale factors (SF). It is defined as the ratio of efficiency (ε) from data and MC in a given kinematic range, $SF = \frac{\varepsilon_{Data}}{\varepsilon_{MC}}$. So, we can evaluate the value of SF by measuring efficiency. We use the tag and probe (T&P) method to estimate the single-muon trigger, identification, and tracking efficiencies on both data and MC. The efficiencies are estimated using Υ (to evaluate trigger efficiency) & J/Ψ (to evaluate muonID & tracker muon efficiency) resonance which is reconstructed as a pair of "tag" and "probe" muon. A tag muon must match tight selection criteria while a probe muon selection depends on the efficiency being measured. A condition is applied to the probes that are split into the passing (matching the probe criteria) and failing (not matching the probe criteria) probe categories. Two categories

of dimuon mass distributions are then separately fitted to the resonance signal and background model. So, one category of dimuon events passes tag+passing probe criteria, and another passes tag+failing probe criteria. The invariant mass fit corresponding to the combination of these two categories, i.e. tag+passing probe+failing probe, is referred to as all probes. We have used these three probe categories to measure the inner-track reconstruction, muon reconstruction and identification, and muon trigger efficiencies. Then the efficiency for a given kinematic bin of η and p_T is evaluated from dimuon invariant mass fits (Ex. Fig. 6.2) as the ratio of resonance signal yield from passing probes and all probes. Numerically it can be written as

$$N_{\text{Passing Probes}} = \epsilon \times N_{\text{All Probes}}, \quad (6.1)$$

$$N_{\text{Failing Probes}} = (1 - \epsilon) \times N_{\text{All Probes}}, \quad (6.2)$$

where $N_{\text{All Probes}}$, $N_{\text{Passing Probes}}$, and $N_{\text{Failing Probes}}$ are the number of all probes, passing probes, and failing probes signal, respectively.

We used following data and MC sample to estimate trigger efficiency:

- Data: /PAForward/PARun2016C-PromptReco-v1/AOD (Run No: 285479-286496 (pPb+Pbp))
- MC: STARLIGHT $\Upsilon(1S)$

MuonID and tracking efficiencies are estimated using the following data and MC sample:

- Data: /PASingleMuon/PARun2016C-PromptReco-v1/AOD (Run No: 285479-286204 (pPb+Pbp))
- Official MC: Psi1SToMuMu_pTMu-2p5_pPb-Bst_8p16-Pythia8

6.1 Trigger efficiency

The following describes the tag, probe, and passing probe requirements for measuring trigger efficiency.

- Tag: tracker muon that passed softID criteria & matching to single muon UPC trigger (HLT_PASingleMuOpen_HFOneTowerVeto_v1)
- Probe: tracker muon that passed softID criteria without trigger matching
- Passing Probe: probe that can be matched to the trigger "HLT_PASingleMuOpen_HFOneTowerVeto_v1"

On top of the above cuts, muons with $p_T > 3$ GeV are considered.

Fig. 6.1 shows the single muon trigger efficiency as a function of muon p_T and η estimated with the Tag and Probe method. Fig. 6.2 shows the example data invariant mass fits for passing, failing and all probes used for trigger efficiency measurement in a given p_T and η bin. Fig. 6.3 shows a similar invariant mass fit for MC. In Fig. 6.2-6.3, the signal is fitted with Gaussian function and the background is fitted with linear function in the dimuon invariant mass range $8 < m_{\mu^+\mu^-} < 12$ GeV. Three yields ($N_{All\ Probes}$, $N_{Passing\ Probes}$, and $N_{Failing\ Probes}$) are extracted from invariant mass fit corresponding to the three cases: passing probes, failing probes and all probes. These yields are used to evaluate efficiency using Eq. 6.1.

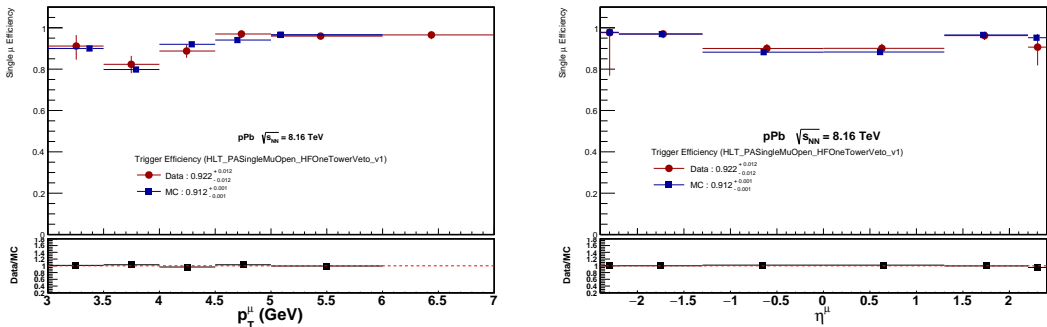


Figure 6.1: Trigger efficiency as a function of muon p_T and η estimated with the Tag and Probe method.

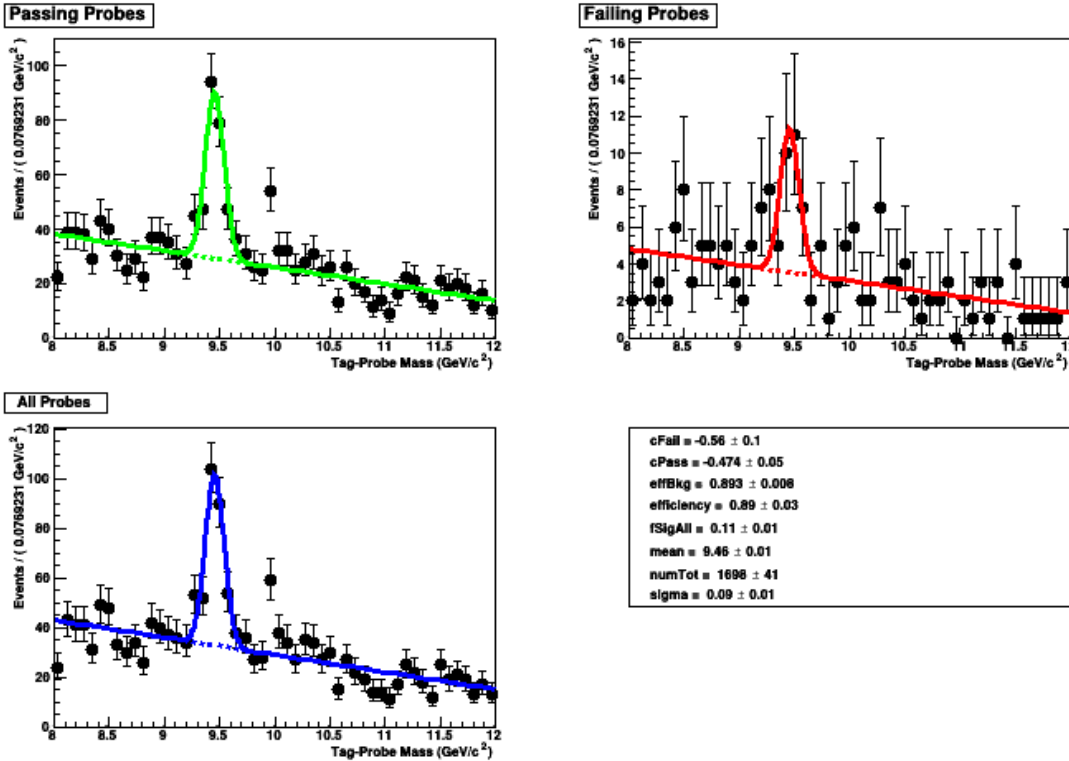


Figure 6.2: Tag-and-probe mass fit for trigger efficiency for data.

Fig. 6.1 shows that the efficiency in the 2nd p_T bin is slightly lower relative to the efficiency in the lowest p_T bin. We can understand it better from this 2D-efficiency plot (Fig. 6.4). From this 2D-plot, we can see that muon can be detected in the barrel region ($|\eta| < 1.3$) if it has $p_T^\mu > 3.3$ GeV. Also, it shows that efficiency is closed to 1 in first $p_T \in [3.0, 3.3]$ bin with $1.3 < |\eta| < 2.4$. In $p_T \in [3.3, 4.0]$ and $\eta \in [0, 1.3]$ region, the trigger efficiency is about $\sim 73\%$. So, if we take average efficiency in the $|\eta| < 2.4$ and $p_T \in [3.3, 4.0]$ region, the efficiency is slightly lower relative to the efficiency in lowest $p_T \in [3.0, 3.3]$ bin. We see similar behaviour for tracking efficiency (Fig. 6.9) also.

6.2 Muon ID efficiency

The tag, probe, and passing probe conditions for evaluating Muon ID efficiency are listed below.

- Tag: tracker muon which passed softID criteria & matching to single muon trigger
(HLT_PAL3Mu3(5,712,15), HLT_PAL2Mu12, HLT_PAL2Mu15)

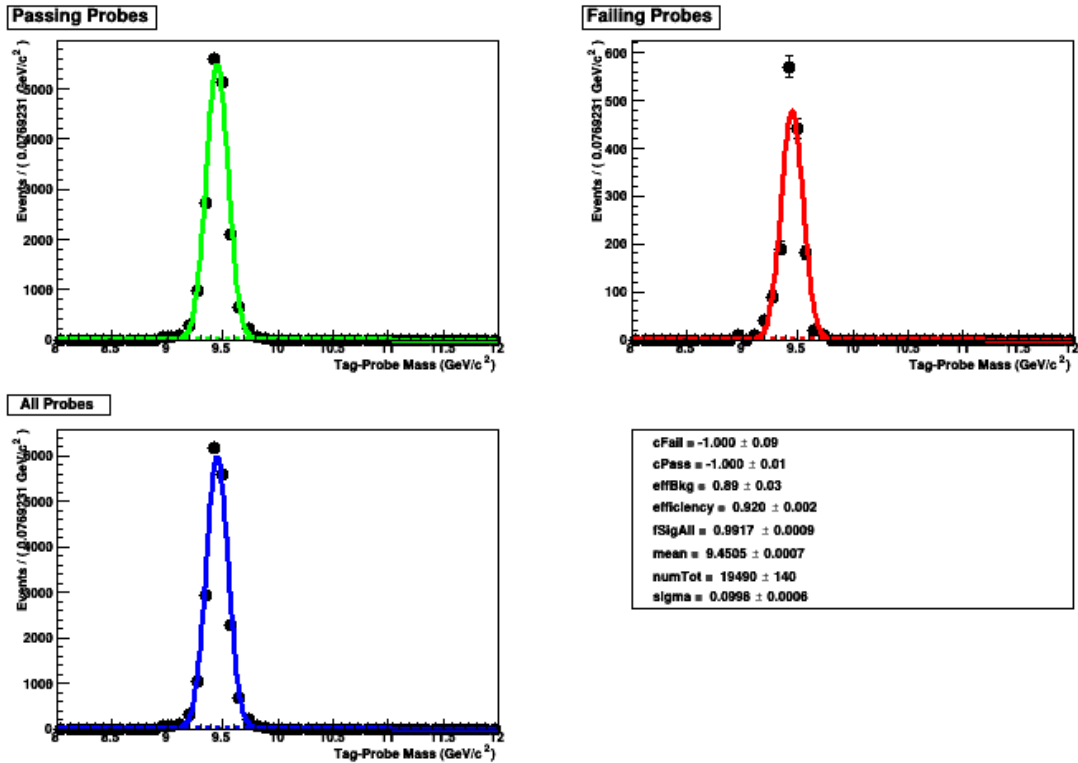


Figure 6.3: Tag-and-probe mass fit for trigger efficiency for MC.

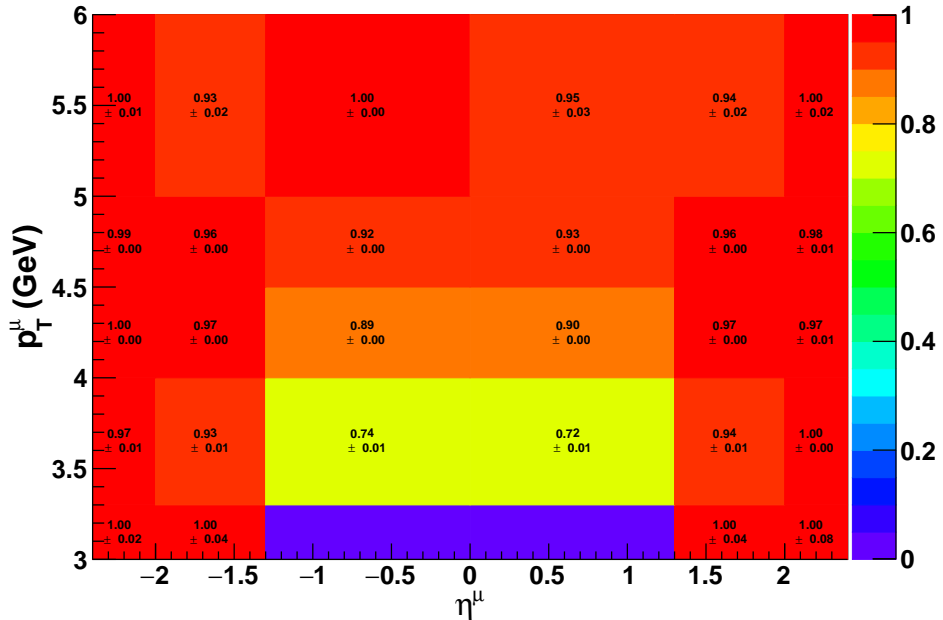


Figure 6.4: Trigger efficiency for MC as a function of muon p_T^μ and η^μ estimated using Tag and Probe method.

- Probe: tracker muon
- Passing Probe: any muon that is matched to the probe muon and passed the softID criteria.

On top of the above cuts, muons with $p_T > 3$ GeV are considered.

Fig. 6.5 shows the Muon ID efficiency as a function of muon p_T and η estimated with the Tag and Probe method. Fig. 6.6 shows the example data invariant mass fits for passing, failing and all probes used for Muon ID efficiency measurement in a given p_T and η bin. Fig. 6.7 shows a similar invariant mass fit for MC. In Fig. 6.6-6.7, the signal is fitted with a Crystal Ball (CB) [77] function and the background is fitted with a linear function in the dimuon invariant mass range $2.6 < m_{\mu^+\mu^-} < 3.6$ GeV. After that, we evaluated Muon ID efficiency using extracted values of $N_{All\ Probes}$, $N_{Passing\ Probes}$, and $N_{Failing\ Probes}$ from the fits and using Eq. 6.1.

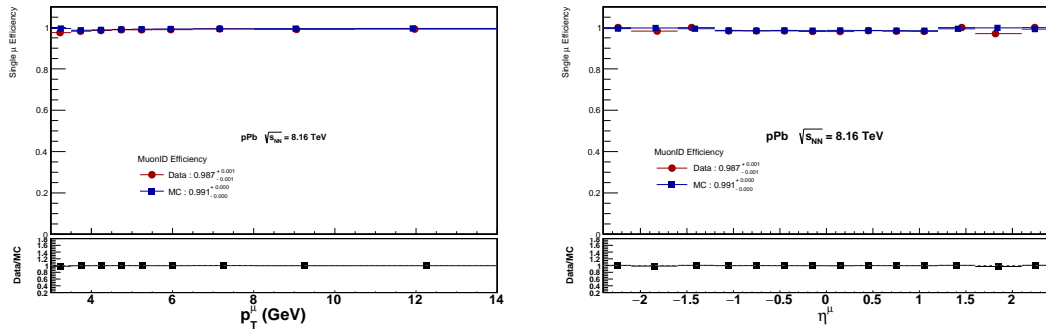


Figure 6.5: Muon ID efficiency as a function of muon p_T and η estimated with the Tag and Probe method.

6.3 Tracking efficiency

The tag, probe, and passing probe criteria for measuring tracker muon efficiency are listed below.

- Tag: tracker muon which passed softID criteria & matching to single muon trigger (HLT_PAL3Mu3(5,712,15), HLT_PAL2Mu12, HLT_PAL2Mu15)
- Probe: muon having a general track

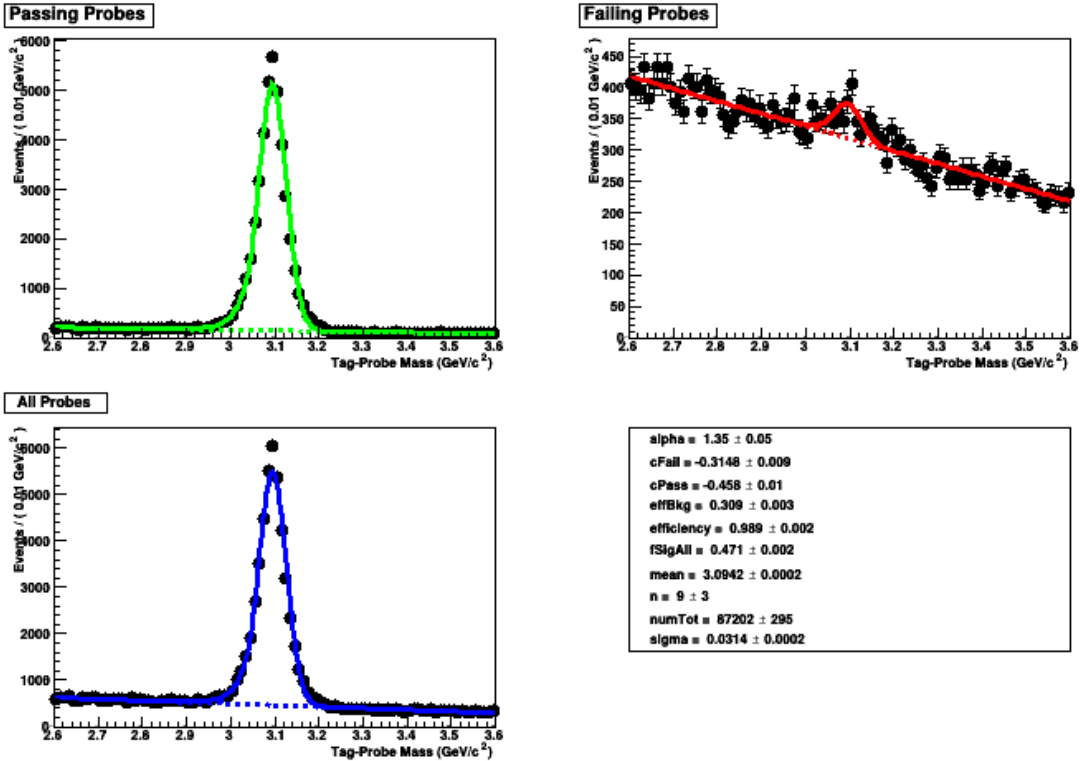


Figure 6.6: Tag-and-probe mass fit for Muon ID efficiency for data.

- Passing Probe: any muon that is matched to the probe muon and is a tracker muon.

On top of the above cuts, muons with $p_T > 3$ GeV are considered.

Fig. 6.8 shows the tracker muon efficiency as a function of muon p_T and η estimated with the Tag and Probe method. Fig. 6.9 shows the example data invariant mass fits for passing, failing and all probes used for tracking efficiency measurement in a given p_T and η bin. Fig. 6.10 shows a similar invariant mass fit for MC. In Fig. 6.9-6.10, the signal is fitted with a combination of CB [77]+Gaussian function and the background is fitted with an exponential function in the dimuon invariant mass range $2.6 < m_{\mu^+\mu^-} < 3.6$ GeV. Then, using the extracted values of $N_{All\ Probes}$, $N_{Passing\ Probes}$, and $N_{Failing\ Probes}$ from the fits and using Eq. 6.1, we estimated tracker muon efficiency.

We can see that the efficiency is more than 90% in the region $p_T^\mu > 3$ GeV and $|\eta_\mu| < 2.4$. But we can detect muon in barrel region ($|\eta| < 1.3$) if it has $p_T > 3.3$ GeV. So, we have chosen $p_T > 3.3$ GeV for symmetric selection of muon through out the entire η region. Hence, we used this as kinematic cuts for Υ selection. Estimated Scale factors (SF) are used for efficiency

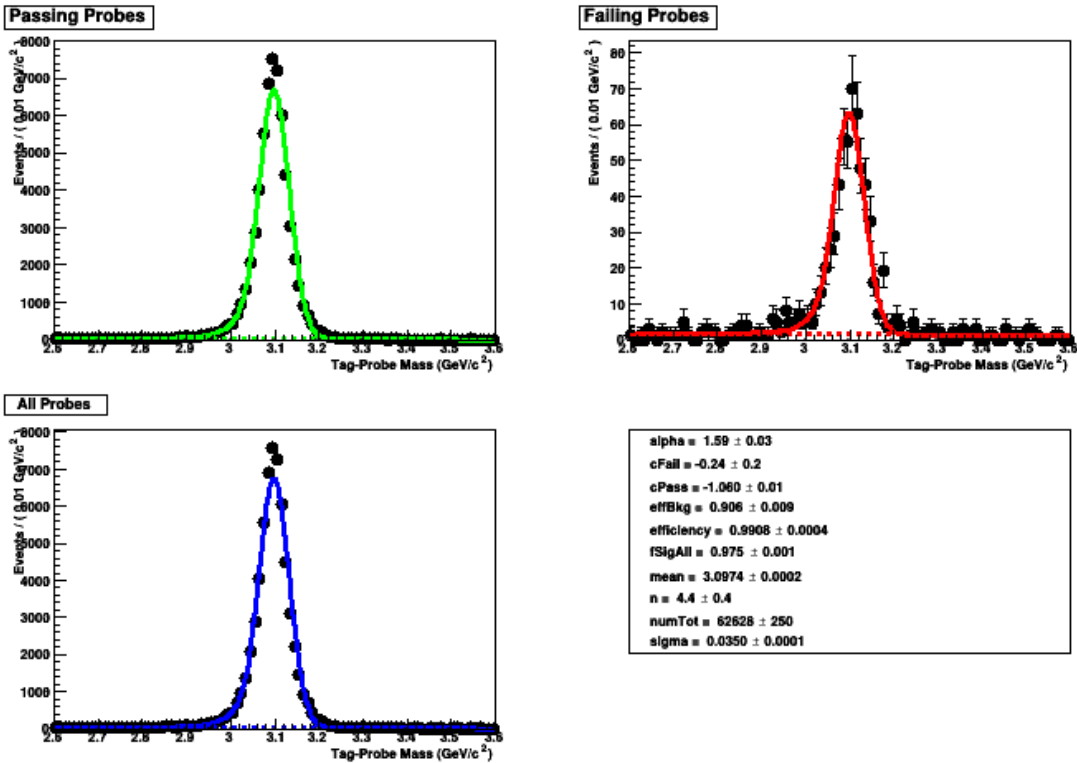


Figure 6.7: Tag-and-probe mass fit for Muon ID efficiency for MC.

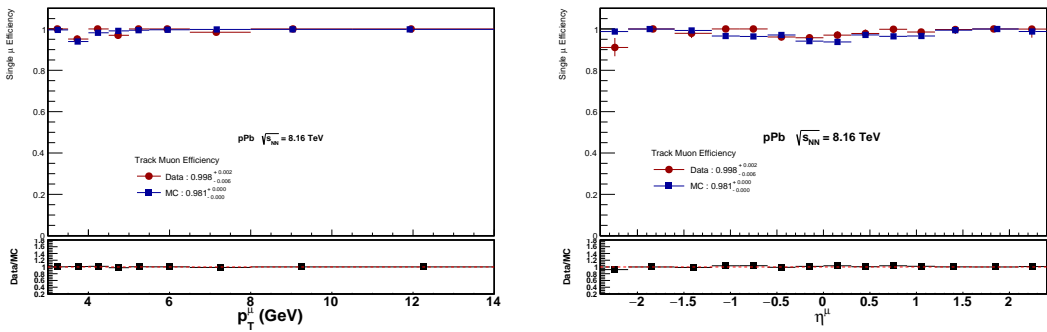


Figure 6.8: Tracker Muon efficiency as a function of muon p_T and η estimated with the Tag and Probe method.

correction (using the factor C^{SF} defined in Eq. 8.7 (in sec. 8.6))

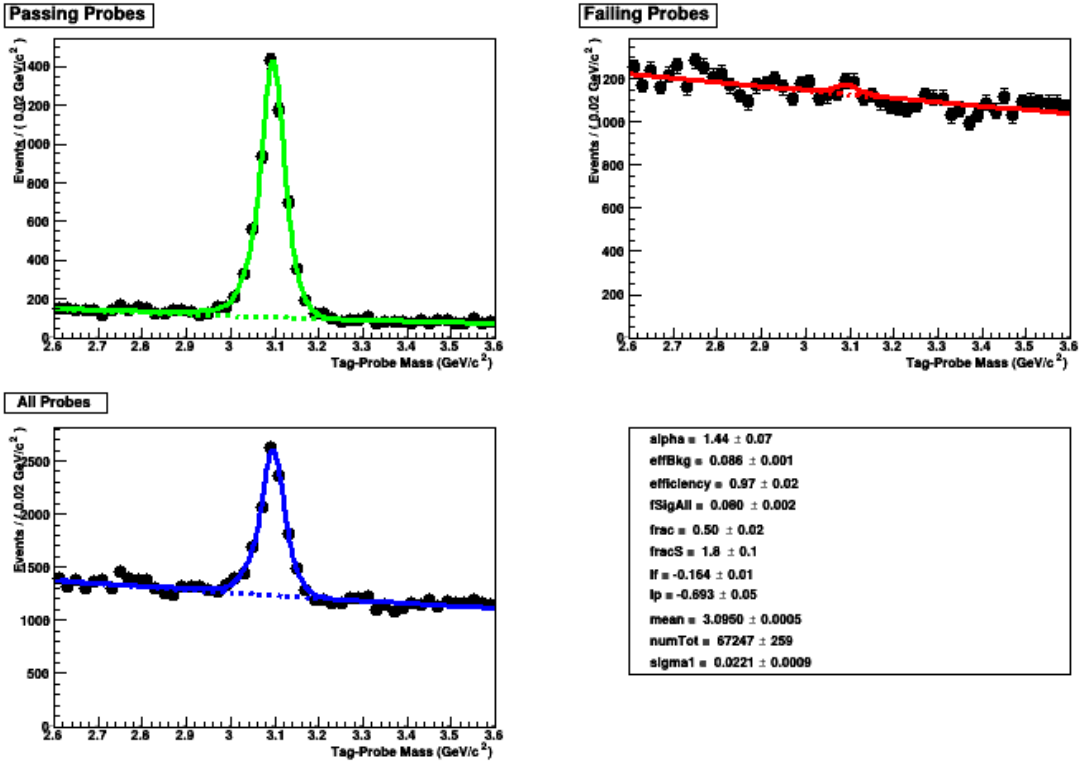


Figure 6.9: Tag-and-probe mass fit for Tracker Muon efficiency for data.

6.4 Acceptance and efficiency

Acceptance is defined as the fraction of events that pass the kinematic region (p_T, η) within which particles are potentially detectable in the detector. Acceptance of a particle is obviously not a guaranteed condition for detection because efficiency is another aspect that determines whether the detector will respond to the particle passage sufficiently to enable detection. Efficiency accounts for reconstruction and identification losses. This is why products of acceptance and efficiency as a function of kinematic variables are usually presented. Acceptance and reconstruction efficiency is estimated from the STARLIGHT MC signal of $\Upsilon(1S)$. The acceptance (A) multiplied by efficiency (ϵ_{MC}) is estimated as the following

$$\begin{aligned}
 A \times \epsilon_{MC} &= \frac{N_{GEN}(Acc(\mu^+, \mu^-), |y_{\mu^+\mu^-}| < 2.2)}{N_{GEN}(p_T^\mu > 0)} \times \frac{N_{RECO}(Acc(\mu^+, \mu^-), \text{quality cut, trigger}, |y_{\mu^+\mu^-}| < 2.2)}{N_{GEN}(Acc(\mu^+, \mu^-), |y_{\mu^+\mu^-}| < 2.2)} \\
 &= \frac{N_{RECO}(Acc(\mu^+, \mu^-), \text{quality cut, trigger}, |y_{\mu^+\mu^-}| < 2.2)}{N_{GEN}(p_T^\mu > 0)},
 \end{aligned} \tag{6.3}$$

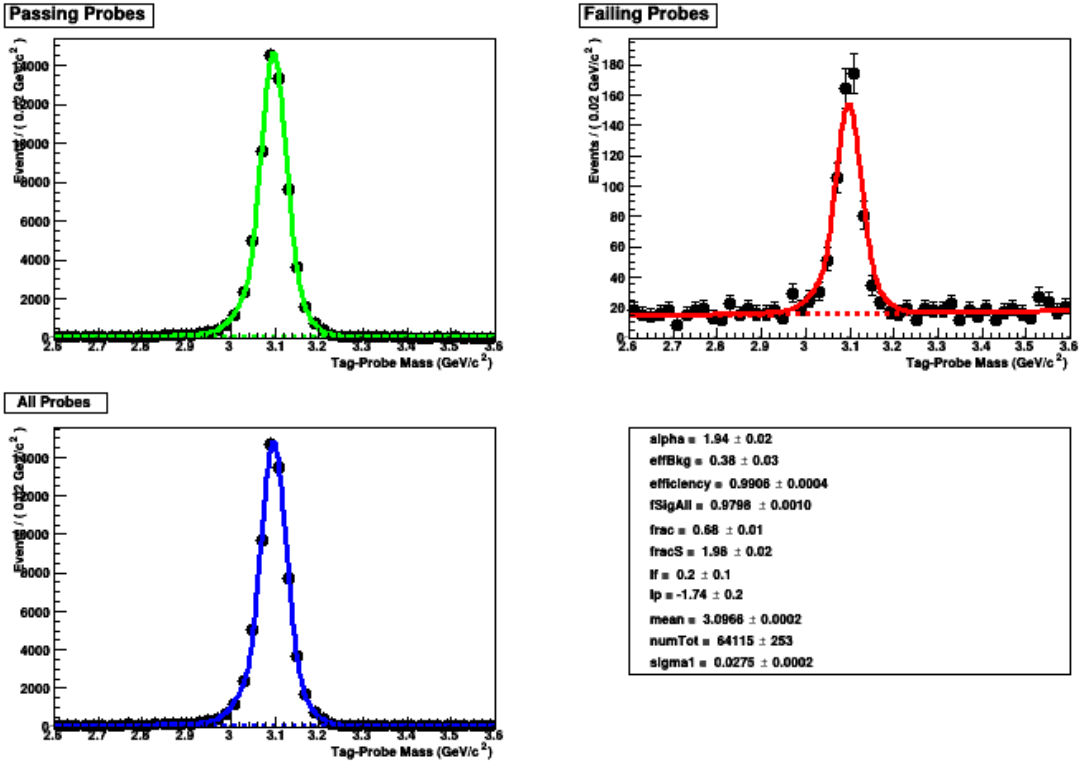


Figure 6.10: Tag-and-probe mass fit for Tracker Muon efficiency for MC.

where N_{RECO} is the number of reconstructed events in a given $(p_T^2(\mu^+\mu^-), y_{\mu^+\mu^-})$ dimuon bin for $\Upsilon(1S)$. N_{GEN} represents all generated dimuons in a given $(p_T^2(\mu^+\mu^-), y_{\mu^+\mu^-})$ bin for $\Upsilon(1S)$. Reconstructed events (N_{RECO}) are passed through the single muon acceptance ($Acc(\mu^+, \mu^-)$), quality cuts (section 5.2), HLT_PASingleMuOpen_HFOneTowerVeto_v1 trigger and $|y_{\mu^+\mu^-}| < 2.2$ criteria. We have applied here $|\eta_\mu| < 2.2$ and $p_T^\mu > 3.3$ GeV as single muon acceptance ($Acc(\mu^+, \mu^-)$) cut. Similarly, generated events are also passed through the kinematic cuts, which are written within parentheses corresponding to the parameter N_{GEN} in Eq. (6.3).

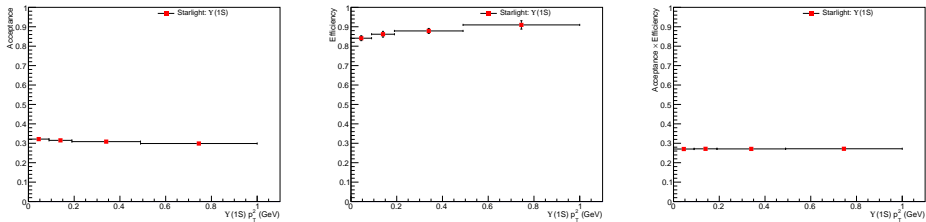


Figure 6.11: Acceptance (left), Efficiency (middle) and Acceptance × Efficiency (right) distributions with $\Upsilon(1S)$ p_T^2 from STARLIGHT MC sample.

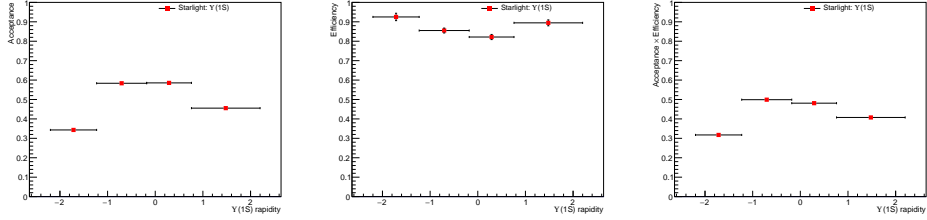


Figure 6.12: Acceptance (left), Efficiency (middle) and Acceptance \times Efficiency (right) distributions with $\Upsilon(1S)$ y from STARLIGHT MC sample.

The Acceptance \times Efficiency of $\Upsilon(1S)$ with $p_T^2(\mu^+\mu^-)$ is given in Fig. 6.11 and with dimuon rapidity is shown in Fig. 6.12. The efficiency includes triggering efficiency, tracking efficiency as well as muon identification efficiency. Table 6.1 shows the acceptance and efficiency in different $p_T^2(\mu^+\mu^-)$ and rapidity bins of $\Upsilon(1S)$.

Table 6.1: Acceptance \times Efficiency of $\Upsilon(1S)$ from STARLIGHT MC.

$p_T^2(\mu^+\mu^-)$ bin (GeV^2)	$A \times \epsilon_{MC}$	$y_{\mu^+\mu^-}$ bin	$A \times \epsilon_{MC}$
(0.00, 0.09)	0.27 ± 0.003	(-2.2, -1.23)	0.32 ± 0.005
(0.09, 0.19)	0.27 ± 0.004	(-1.23, -0.18)	0.50 ± 0.007
(0.19, 0.49)	0.27 ± 0.003	(-0.18, 0.76)	0.48 ± 0.007
(0.49, 1.00)	0.27 ± 0.005	(0.76, 2.2)	0.41 ± 0.006

Chapter 7

Invariant mass fitting

The invariant mass distribution of $\mu^+\mu^-$ pairs in the range between 8 and 12 GeV, satisfying the selection criteria described above, are shown in Figs. 7.1-7.6. A fit to the spectrum is performed using ROOFIT [78] with a linear or Error \times Exponential (Err \times Exp) function to describe the QED $\gamma\gamma \rightarrow \mu^+\mu^-$ continuum background, combined with three Gaussians for the three Υ signal peaks. Mathematically, the Err \times Exp function for background fitting (B) can be written as

$$B(m_{\mu^+\mu^-}; \mu, \sigma, \tau) = \frac{1 + \text{Err}(\frac{m_{\mu^+\mu^-} - \mu}{\sqrt{2}\sigma})}{2} \times \exp(\tau m_{\mu^+\mu^-}). \quad (7.1)$$

Fig. 7.1-7.3 show the fitting of invariant mass distribution of muon pairs from $\Upsilon(1S)$, $\Upsilon(2S)$, and $\Upsilon(3S)$ mesons and two-photon QED generated by the STARLIGHT MC event generator. The details are given in Table 7.1. Fig. 7.5 shows the global fitting of invariant mass distribution of muon pairs from data. Fig. 7.4 and Fig. 7.6 show the invariant mass fitting of muon pairs of data in different $y_{\mu^+\mu^-}$ and $p_T^2(\mu^+\mu^-)$ bins respectively. We have taken assymetric $y_{\mu^+\mu^-}$ and $p_T^2(\mu^+\mu^-)$ bins such a way that the fitting is stable and each bin has almost equal statistics. Invariant mass fitting is done in the 4-rapidity ranges $-2.2 < y_{\mu^+\mu^-} < -1.23$,

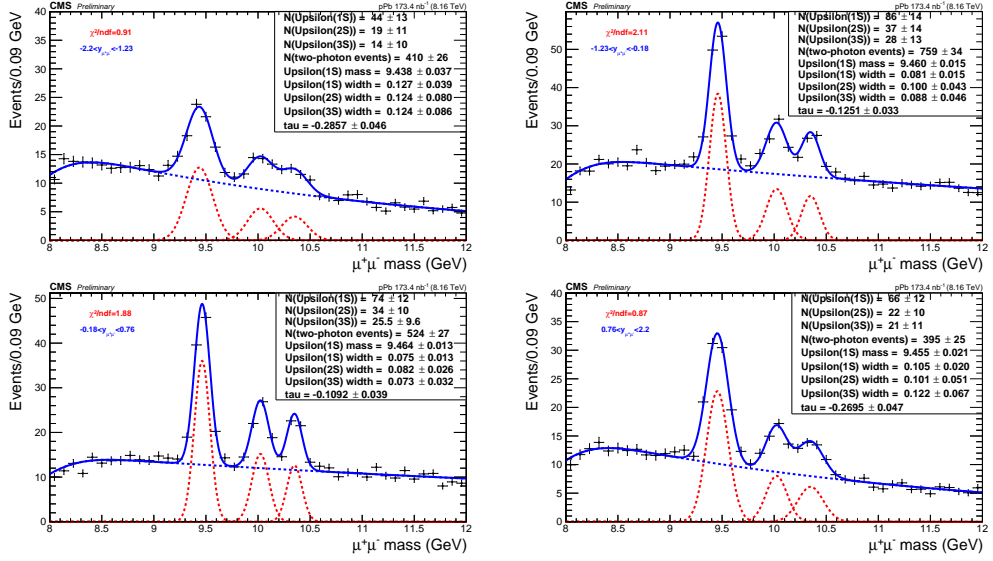


Figure 7.1: Invariant mass distribution of exclusive muon pair candidates in four asymmetric rapidity bins that pass all the selection criteria from STARLIGHT MC, fitted to a Err \times Exp function for the two-photon QED continuum (blue dashed curve) plus three Gaussian distributions corresponding to the $\Upsilon(1S)$, $\Upsilon(2S)$, and $\Upsilon(3S)$ mesons (red dotted curves). Invariant mass fitting is done in the following 4-rapidity range: (a) $-2.2 < y_{\mu^+\mu^-} < -1.23$ (upper left plot), (b) $-1.23 < y_{\mu^+\mu^-} < -0.18$ (upper right plot), (c) $-0.18 < y_{\mu^+\mu^-} < 0.76$ (lower left plot), and (d) $0.76 < y_{\mu^+\mu^-} < 2.2$ (lower right plot). Details are given in the Table 7.1.

$-1.23 < y_{\mu^+\mu^-} < -0.18$, $-0.18 < y_{\mu^+\mu^-} < 0.76$, and $0.76 < y_{\mu^+\mu^-} < 2.2$. Similarly dimuon invariant mass fitting is done in the 4- p_T^2 bins $0 < p_T^2(\mu^+\mu^-) < 0.09$, $0.09 < p_T^2(\mu^+\mu^-) < 0.19$, $0.19 < p_T^2(\mu^+\mu^-) < 0.49$, and $0.49 < p_T^2(\mu^+\mu^-) < 1.0$. For the invariant mass fitting of STARLIGHT MC in different $y_{\mu^+\mu^-}$ and $p_T^2(\mu^+\mu^-)$ bins (Fig. 7.1-7.3), the free parameters are Mass ($M_{\Upsilon(1S)}$), Width ($W_{\Upsilon(1S,2S,3S)}$), $N_{\Upsilon(1S)}$, $N_{\Upsilon(2S)}$, $N_{\Upsilon(3S)}$, N_{QED} and slope τ of Err \times Exp function. In Fig. 7.1-7.3, the fixed parameters are the mass of $\Upsilon(2S)$ and $\Upsilon(3S)$ to their PDG values [79]. In case of data fitting in different $y_{\mu^+\mu^-}$ bins (Fig. 7.4-7.5), the free parameters are Mass ($M_{\Upsilon(1S)}$), Width ($W_{\Upsilon(1S)}$), $N_{\Upsilon(1S)}$, N_{QED} and slope τ of Err \times Exp function. In Fig. 7.4-7.5, the fixed parameters are the number of $\Upsilon(2S)$ and $\Upsilon(3S)$. The number of $\Upsilon(2S)$ and $\Upsilon(3S)$ are expressed in terms of the number of $\Upsilon(1S)$ times the ratio of their masses ($M_{\Upsilon(2S,3S)}/M_{\Upsilon(1S)}$). If we don't apply this constraint, we see an unnatural increase of $N_{\Upsilon(3S)}$ relative to $N_{\Upsilon(2S)}$ in a very forward rapidity bin due to low statistics in case of data fitting. For invariant mass fitting of data

in different $p_T^2(\mu^+\mu^-)$ bins (Fig. 7.6), the free parameters are Mass ($M_{\Upsilon(1S)}$), Width ($W_{\Upsilon(1S)}$), $N_{\Upsilon(1S)}$, $N_{\Upsilon(2S)}$, $N_{\Upsilon(3S)}$, N_{QED} and slope of linear function. In Fig. 7.6, the fixed parameters are the mass differences of $M_{\Upsilon(2S,3S)} - M_{\Upsilon(1S)}$ to the PDG value [79], and the widths of $\Upsilon(2S)$ and $\Upsilon(3S)$. The widths of $\Upsilon(2S)$ and $\Upsilon(3S)$ are expressed in terms of the $\Upsilon(1S)$ width scaled by the ratio of their masses ($M_{\Upsilon(2S,3S)}/M_{\Upsilon(1S)}$), to make the fitting stable for such low statistics data. Details are given in Table 7.1-7.2.

We have chosen a background fit function based on the goodness of fit, i.e., χ^2/ndf . If χ^2/ndf is better (i.e. closed to 1) for Err \times Exp function relative to linear, we have taken Err \times Exp function for background fitting and vice versa. Figures 7.1-7.5 are fitted with a background fit function Err \times Exp as a kink is present around dimuon mass 8.2 GeV. The error function takes care of that kink part.

Fig. 7.1-7.6 show clear signatures of three distinct peaks of $\Upsilon(1S)$, $\Upsilon(2S)$ and $\Upsilon(3S)$. Both MC (Fig. 7.1) and data (Fig. 7.4) show different widths of $\Upsilon(1S)$ in different rapidity regions as the detector resolution is not the same throughout the entire rapidity region. Using the extracted number of $\Upsilon(1S)$ from the invariant mass fitting in data, we can estimate the number of exclusive $\Upsilon(1S)$, i.e. $N_{\Upsilon(1S)}^{exc}$, and details of it are discussed in chapter 8.6.

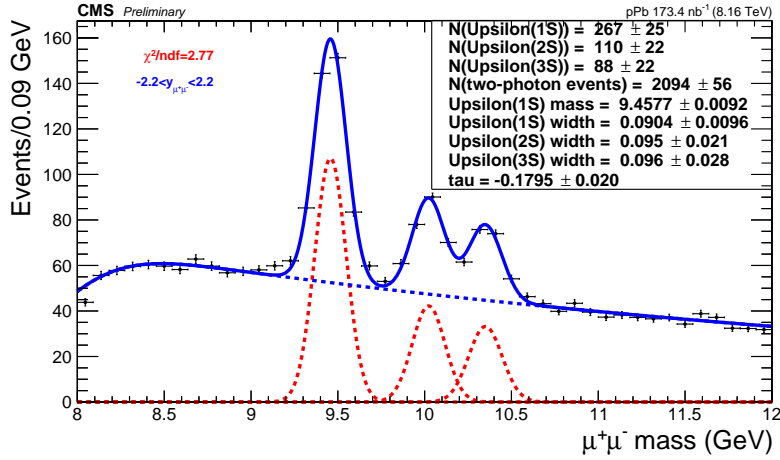


Figure 7.2: Invariant mass distribution of exclusive muon pair candidates in the rapidity interval $|y_{\mu^+\mu^-}| < 2.2$ that pass all the selection criteria from STARLIGHT MC, fitted to an Err \times Exp function for the two-photon QED continuum (blue dashed curve) plus three Gaussian distributions corresponding to the $\Upsilon(1S)$, $\Upsilon(2S)$, and $\Upsilon(3S)$ mesons (red dotted curves). Details are given in Table 7.1.

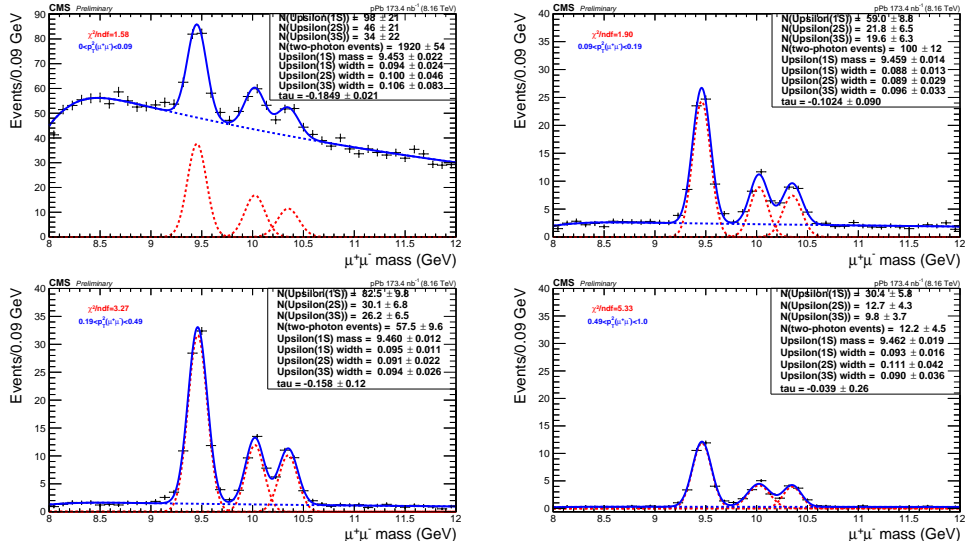


Figure 7.3: Invariant mass distribution of exclusive muon pair candidates of STARLIGHT MC in four asymmetric $p_T^2(\mu^+\mu^-)$ bins that pass all the selection criteria, fitted to a Err \times Exp function for the two-photon QED continuum (blue dashed curve) plus three Gaussian distributions corresponding to the $\Upsilon(1S)$, $\Upsilon(2S)$, and $\Upsilon(3S)$ mesons (red dotted curves). Invariant mass fitting is done in the following 4- p_T^2 range: (a) $0 < p_T^2(\mu^+\mu^-) < 0.09$ (upper left plot), (b) $0.09 < p_T^2(\mu^+\mu^-) < 0.19$ (upper right plot), (c) $0.19 < p_T^2(\mu^+\mu^-) < 0.49$ (lower left plot), and (d) $0.49 < p_T^2(\mu^+\mu^-) < 1.0$ (lower right plot). The details are given in Table 7.1.

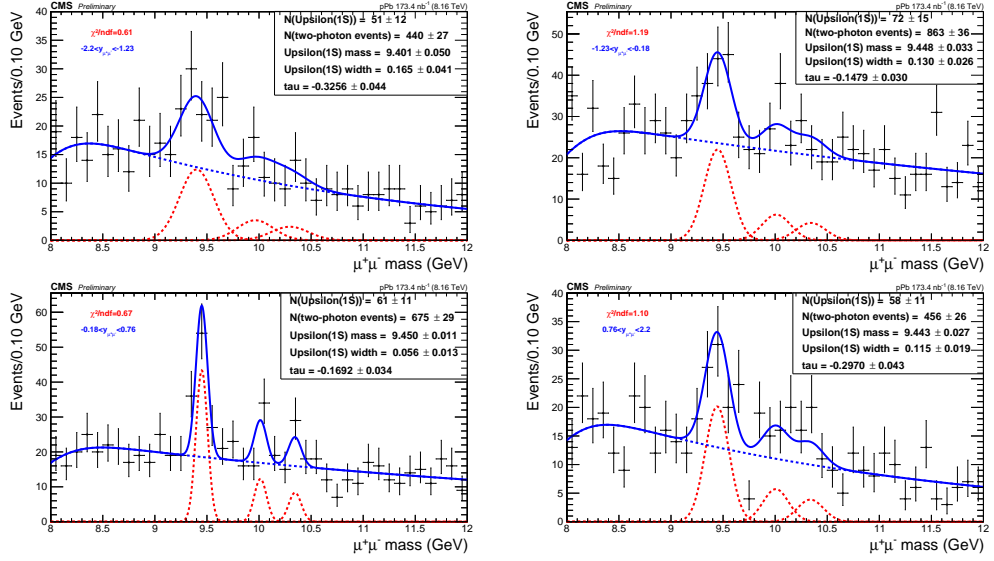


Figure 7.4: Invariant mass distribution of exclusive muon pair candidates of data in four asymmetric rapidity bins that pass all the selection criteria, fitted to a Err \times Exp function for the two-photon QED continuum (blue dashed curve) plus three Gaussian distributions corresponding to the $\Upsilon(1S)$, $\Upsilon(2S)$, and $\Upsilon(3S)$ mesons (red dotted curves). Invariant mass fitting is done in the following 4-rapidity range: (a) $-2.2 < y_{\mu^+\mu^-} < -1.23$ (upper left plot), (b) $-1.23 < y_{\mu^+\mu^-} < -0.18$ (upper right plot), (c) $-0.18 < y_{\mu^+\mu^-} < 0.76$ (lower left plot), and (d) $0.76 < y_{\mu^+\mu^-} < 2.2$ (lower right plot). The details are given in Table 7.2.

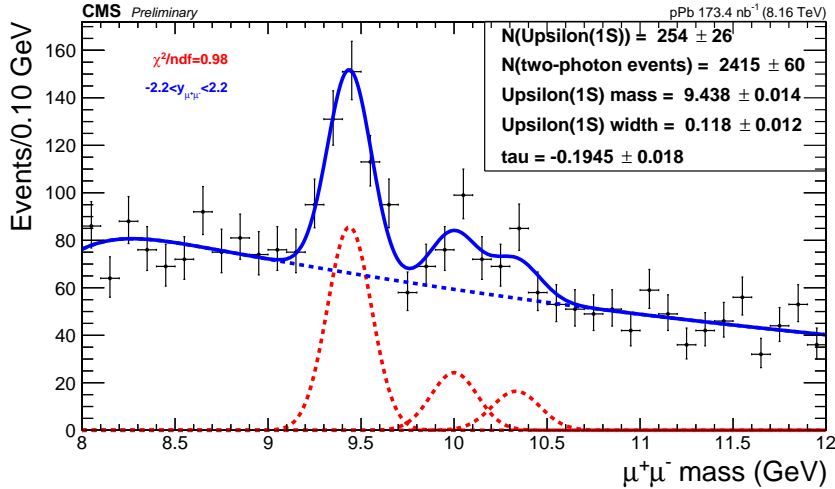


Figure 7.5: Invariant mass distribution of exclusive muon pair candidates of data in the rapidity interval $|y_{\mu^+\mu^-}| < 2.2$ that pass all the selection criteria, fitted to an Err \times Exp function for the two-photon QED continuum (blue dashed curve) plus three Gaussian distributions corresponding to the $\Upsilon(1S)$, $\Upsilon(2S)$, and $\Upsilon(3S)$ mesons (red dotted curves). The details are given in Table 7.2.

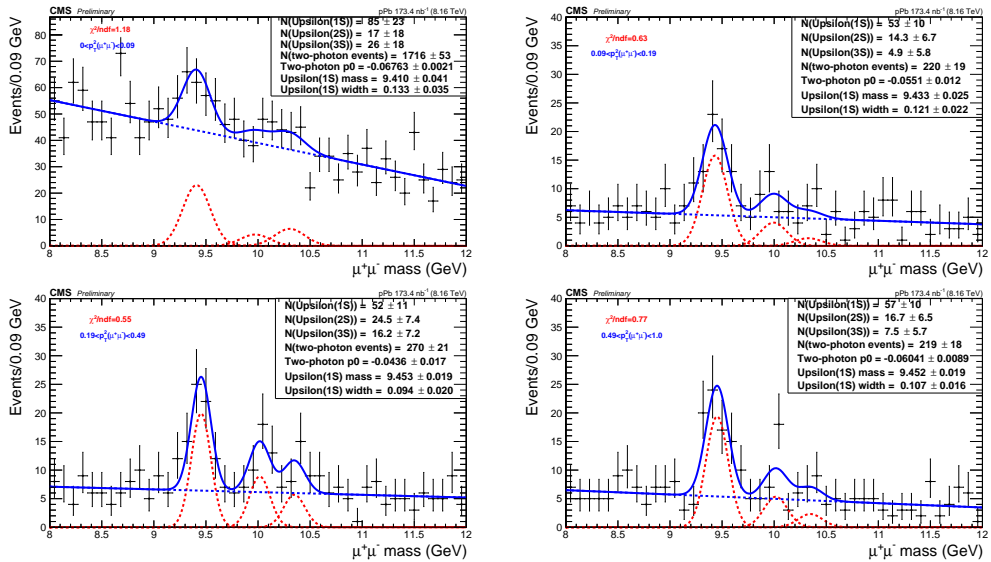


Figure 7.6: Invariant mass distribution of exclusive muon pair candidates of data in four asymmetric $p_T^2(\mu^+\mu^-)$ bins that pass all the selection criteria, fitted to a linear function for the two-photon QED continuum (blue dashed curve) plus three Gaussian distributions corresponding to the $\Upsilon(1S)$, $\Upsilon(2S)$, and $\Upsilon(3S)$ mesons (red dotted curves). Invariant mass fitting is done in the following 4- p_T^2 range: (a) $0 < p_T^2(\mu^+\mu^-) < 0.09$ (upper left plot), (b) $0.09 < p_T^2(\mu^+\mu^-) < 0.19$ (upper right plot), (c) $0.19 < p_T^2(\mu^+\mu^-) < 0.49$ (lower left plot), and (d) $0.49 < p_T^2(\mu^+\mu^-) < 1.0$ (lower right plot). The details are given in Table 7.2.

Table 7.1: Summary of different fitting of invariant mass distribution of muon pairs from STARLIGHT MC.

Kinematic region	Fitting	No. of $\Upsilon(nS)$ and QED	χ^2/ndf
Dimuon invmass in different rapidity bins			
$y \in [-2.2, -1.23]$	Gaussian (Signal) + Err \times Exp (QED) bkg. Free param.: Mass(1S), Width(1S,2S,3S), $N_{\Upsilon(1S)}, N_{\Upsilon(2S)}, N_{\Upsilon(3S)}, N_{QED}$ Err \times Exp, 9 free par, Fixed par: PDG Mass(2S,3S)	$N_{\Upsilon(1S)} = 44 \pm 13$ $N_{\Upsilon(2S)} = 19 \pm 11$ $N_{\Upsilon(3S)} = 14 \pm 10$ $N_{QED} = 410 \pm 26$	0.91
$y \in [-1.23, -0.18]$	Gaussian (Signal) + Err \times Exp (QED) bkg. Free param.: Mass(1S), Width(1S,2S,3S), $N_{\Upsilon(1S)}, N_{\Upsilon(2S)}, N_{\Upsilon(3S)}, N_{QED}$ Err \times Exp, 9 free par, Fixed par: PDG Mass(2S,3S)	$N_{\Upsilon(1S)} = 86 \pm 14$ $N_{\Upsilon(2S)} = 37 \pm 14$ $N_{\Upsilon(3S)} = 28 \pm 13$ $N_{QED} = 759 \pm 34$	2.11
$y \in [-0.18, 0.76]$	Gaussian (Signal) + Err \times Exp (QED) bkg. Free param.: Mass(1S), Width(1S,2S,3S), $N_{\Upsilon(1S)}, N_{\Upsilon(2S)}, N_{\Upsilon(3S)}, N_{QED}$ Err \times Exp, 9 free par, Fixed par: PDG Mass(2S,3S)	$N_{\Upsilon(1S)} = 74 \pm 12$ $N_{\Upsilon(2S)} = 34 \pm 10$ $N_{\Upsilon(3S)} = 26 \pm 10$ $N_{QED} = 524 \pm 27$	1.88
$y \in [-0.18, 0.76]$	Gaussian (Signal) + Err \times Exp (QED) bkg. Free param.: Mass(1S), Width(1S,2S,3S), $N_{\Upsilon(1S)}, N_{\Upsilon(2S)}, N_{\Upsilon(3S)}, N_{QED}$ Err \times Exp, 9 free par, Fixed par: PDG Mass(2S,3S)	$N_{\Upsilon(1S)} = 66 \pm 12$ $N_{\Upsilon(2S)} = 22 \pm 10$ $N_{\Upsilon(3S)} = 21 \pm 11$ $N_{QED} = 395 \pm 25$	0.87
$y \in [-2.2, 2.2]$	Gaussian (Signal) + Err \times Exp (QED) bkg. Free param.: Mass(1S), Width(1S,2S,3S), $N_{\Upsilon(1S)}, N_{\Upsilon(2S)}, N_{\Upsilon(3S)}, N_{QED}$ Err \times Exp, 9 free par, Fixed par: PDG Mass(2S,3S)	$N_{\Upsilon(1S)} = 267 \pm 25$ $N_{\Upsilon(2S)} = 110 \pm 22$ $N_{\Upsilon(3S)} = 88 \pm 22$ $N_{QED} = 2094 \pm 56$	2.77
Dimuon invmass in different p_T^2 bins			
$p_T^2 \in [0.0, 0.09] \text{ GeV}$	Gaussian (Signal) + Err \times Exp (QED) bkg. Free param.: Mass(1S), Width(1S,2S,3S), $N_{\Upsilon(1S)}, N_{\Upsilon(2S)}, N_{\Upsilon(3S)}, N_{QED}$ Err \times Exp, 9 free par, Fixed par: PDG Mass(2S,3S)	$N_{\Upsilon(1S)} = 98 \pm 21$ $N_{\Upsilon(2S)} = 46 \pm 21$ $N_{\Upsilon(3S)} = 34 \pm 22$ $N_{QED} = 1920 \pm 54$	1.58
$p_T^2 \in [0.09, 0.19] \text{ GeV}$	Gaussian (Signal) + Err \times Exp (QED) bkg. Free param.: Mass(1S), Width(1S,2S,3S), $N_{\Upsilon(1S)}, N_{\Upsilon(2S)}, N_{\Upsilon(3S)}, N_{QED}$ Err \times Exp, 9 free par, Fixed par: PDG Mass(2S,3S)	$N_{\Upsilon(1S)} = 59 \pm 9$ $N_{\Upsilon(2S)} = 22 \pm 7$ $N_{\Upsilon(3S)} = 20 \pm 6$ $N_{QED} = 100 \pm 12$	1.9
$p_T^2 \in [0.19, 0.49] \text{ GeV}$	Gaussian (Signal) + Err \times Exp (QED) bkg. Free param.: Mass(1S), Width(1S,2S,3S), $N_{\Upsilon(1S)}, N_{\Upsilon(2S)}, N_{\Upsilon(3S)}, N_{QED}$ Err \times Exp, 9 free par, Fixed par: PDG Mass(2S,3S)	$N_{\Upsilon(1S)} = 83 \pm 10$ $N_{\Upsilon(2S)} = 30 \pm 7$ $N_{\Upsilon(3S)} = 26 \pm 7$ $N_{QED} = 58 \pm 10$	3.27
$p_T^2 \in [0.49, 1.0] \text{ GeV}$	Gaussian (Signal) + Err \times Exp (QED) bkg. Free param.: Mass(1S), Width(1S,2S,3S), $N_{\Upsilon(1S)}, N_{\Upsilon(2S)}, N_{\Upsilon(3S)}, N_{QED}$ Err \times Exp, 9 free par, Fixed par: PDG Mass(2S,3S)	$N_{\Upsilon(1S)} = 30 \pm 6$ $N_{\Upsilon(2S)} = 13 \pm 4$ $N_{\Upsilon(3S)} = 10 \pm 4$ $N_{QED} = 12 \pm 5$	5.33

Table 7.2: Summary of different fitting of invariant mass distribution of data.

Kinematic region	Fitting	No. of Υ and QED	χ^2/ndf
Dimuon invariant mass in different rapidity bins			
$y \in [-2.2, -1.23]$	Gaussian (Signal) + Err \times Exp (QED) bkg. Free param.: Mass(1S), Width(1S), $N_{\Upsilon(1S)}$, N_{QED} , Err \times Exp, 5 free par Fixed par: $N_{\Upsilon(1S)} \times M_{\Upsilon(2S,3S)} / M_{\Upsilon(1S)}$	$N_{\Upsilon(1S)} = 51 \pm 12$ $N_{QED} = 440 \pm 27$ $W_{\Upsilon(1S)} = 0.17 \pm 0.04$ Slope $\tau = 0.33 \pm 0.04$	0.61
$y \in [-1.23, -0.18]$	Gaussian (Signal) + Err \times Exp (QED) bkg. Free param.: Mass(1S), Width(1S), $N_{\Upsilon(1S)}$, N_{QED} , Err \times Exp, 5 free par Fixed par: $N_{\Upsilon(1S)} \times M_{\Upsilon(2S,3S)} / M_{\Upsilon(1S)}$	$N_{\Upsilon(1S)} = 72 \pm 15$ $N_{QED} = 863 \pm 36$ $W_{\Upsilon(1S)} = 0.13 \pm 0.03$ Slope $\tau = 0.15 \pm 0.03$	1.19
$y \in [-0.18, -0.76]$	Gaussian (Signal) + Err \times Exp (QED) bkg. Free param.: Mass(1S), Width(1S), $N_{\Upsilon(1S)}$, N_{QED} , Err \times Exp, 5 free par Fixed par: $N_{\Upsilon(1S)} \times M_{\Upsilon(2S,3S)} / M_{\Upsilon(1S)}$	$N_{\Upsilon(1S)} = 61 \pm 11$ $N_{QED} = 675 \pm 29$ $W_{\Upsilon(1S)} = 0.06 \pm 0.01$ Slope $\tau = 0.17 \pm 0.03$	0.67
$y \in [0.76, -2.2]$	Gaussian (Signal) + Err \times Exp (QED) bkg. Free param.: Mass(1S), Width(1S), $N_{\Upsilon(1S)}$, N_{QED} , Err \times Exp, 5 free par Fixed par: $N_{\Upsilon(1S)} \times M_{\Upsilon(2S,3S)} / M_{\Upsilon(1S)}$	$N_{\Upsilon(1S)} = 58 \pm 11$ $N_{QED} = 456 \pm 26$ $W_{\Upsilon(1S)} = 0.12 \pm 0.02$ Slope $\tau = 0.30 \pm 0.04$	1.10
$y \in [-2.2, -2.2]$	Gaussian (Signal) + Err \times Exp (QED) bkg. Free param.: Mass(1S), Width(1S), $N_{\Upsilon(1S)}$, N_{QED} , Err \times Exp, 5 free par Fixed par: $N_{\Upsilon(1S)} \times M_{\Upsilon(2S,3S)} / M_{\Upsilon(1S)}$	$N_{\Upsilon(1S)} = 254 \pm 26$ $N_{QED} = 2415 \pm 60$ $W_{\Upsilon(1S)} = 0.12 \pm 0.01$ Slope $\tau = 0.19 \pm 0.02$	0.98
Dimuon invmass in different p_T^2 bins			
$p_T^2 \in [0.0, 0.09] \text{ GeV}$	Gaussian (Signal) + pol1 (QED) bkg. Free param.: Mass(1S), Width(1S), $N_{\Upsilon(1S)}$, $N_{\Upsilon(2S)}$, $N_{\Upsilon(3S)}$, N_{QED} , pol1, 7 free par, Fixed par: $M_{\Upsilon(2S,3S)} - M_{\Upsilon(1S)}$, $W_{\Upsilon(2S,3S)} = W_{\Upsilon(1S)} \times M_{\Upsilon(2S,3S)} / M_{\Upsilon(1S)}$	$N_{\Upsilon(1S)} = 85 \pm 23$ $N_{\Upsilon(2S)} = 17 \pm 18$ $N_{\Upsilon(3S)} = 26 \pm 18$ $N_{QED} = 1716 \pm 53$	1.18
$p_T^2 \in [0.09, 0.19] \text{ GeV}$	Gaussian (Signal) + pol1 (QED) bkg. Free param.: Mass(1S), Width(1S), $N_{\Upsilon(1S)}$, $N_{\Upsilon(2S)}$, $N_{\Upsilon(3S)}$, N_{QED} , pol1, 7 free par, Fixed par: $M_{\Upsilon(2S,3S)} - M_{\Upsilon(1S)}$, $W_{\Upsilon(2S,3S)} = W_{\Upsilon(1S)} \times M_{\Upsilon(2S,3S)} / M_{\Upsilon(1S)}$	$N_{\Upsilon(1S)} = 53 \pm 10$ $N_{\Upsilon(2S)} = 14 \pm 7$ $N_{\Upsilon(3S)} = 5 \pm 6$ $N_{QED} = 220 \pm 19$	0.63
$p_T^2 \in [0.19, 0.49] \text{ GeV}$	Gaussian (Signal) + pol1 (QED) bkg. Free param.: Mass(1S), Width(1S), $N_{\Upsilon(1S)}$, $N_{\Upsilon(2S)}$, $N_{\Upsilon(3S)}$, N_{QED} , pol1, 7 free par, Fixed par: $M_{\Upsilon(2S,3S)} - M_{\Upsilon(1S)}$, $W_{\Upsilon(2S,3S)} = W_{\Upsilon(1S)} \times M_{\Upsilon(2S,3S)} / M_{\Upsilon(1S)}$	$N_{\Upsilon(1S)} = 52 \pm 11$ $N_{\Upsilon(2S)} = 25 \pm 7$ $N_{\Upsilon(3S)} = 16 \pm 7$ $N_{QED} = 270 \pm 21$	0.55
$p_T^2 \in [0.49, 1.0] \text{ GeV}$	Gaussian (Signal) + pol1 (QED) bkg. Free param.: Mass(1S), Width(1S), $N_{\Upsilon(1S)}$, $N_{\Upsilon(2S)}$, $N_{\Upsilon(3S)}$, N_{QED} , pol1, 7 free par, Fixed par: $M_{\Upsilon(2S,3S)} - M_{\Upsilon(1S)}$, $W_{\Upsilon(2S,3S)} = W_{\Upsilon(1S)} \times M_{\Upsilon(2S,3S)} / M_{\Upsilon(1S)}$	$N_{\Upsilon(1S)} = 57 \pm 10$ $N_{\Upsilon(2S)} = 17 \pm 7$ $N_{\Upsilon(3S)} = 8 \pm 6$ $N_{QED} = 219 \pm 18$	0.77

Chapter 8

Background estimation and extraction of cross-sections

8.1 QED background

In order to extract the exclusive $\gamma p \rightarrow \Upsilon(\mu^+ \mu^-) p$ signal events, the exclusive QED and the non-exclusive backgrounds need to be subtracted. QED events are rejected in data by fitting the dimuon invariant mass with the Err \times Exp function or linear function. The data and QED from STARLIGHT MC are compared in the side-band region, dimuon invariant mass $8 < m_{\mu^+ \mu^-} < 9$ and $11 < m_{\mu^+ \mu^-} < 20$ GeV with dimuon $p_T(\mu^+ \mu^-) < 0.15$ GeV and shown in Fig. 8.1. The region away from the signal resonance is known as the side-band region. In this region, one can find backgrounds only and no signal contribution. The ratio of the data yield and the STARLIGHT QED MC integrated over these regions is measured to be 0.88 ± 0.02 , confirming that this event generator reproduces the data well, as observed previously in pPb and PbPb collisions at the LHC [80–82].

The absolute prediction of the cross-section from this generator is cross-checked by com-

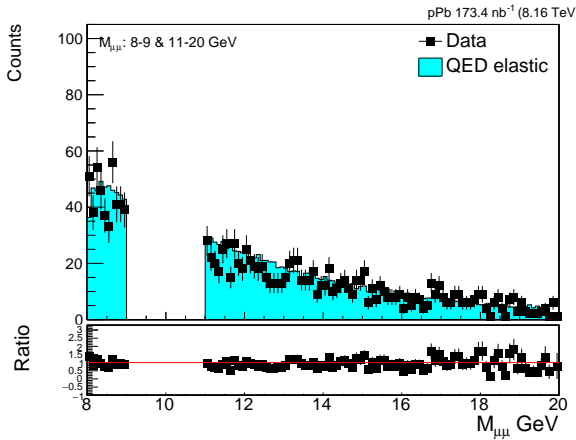


Figure 8.1: Invariant mass distribution of data and MC in the sideband region ($8 < m_{\mu^+\mu^-} < 9$ GeV and $11 < m_{\mu^+\mu^-} < 20$ GeV) and $p_T(\mu^+\mu^-) < 0.15$ GeV where data is dominated by QED.

paring data and simulation in regions away from the Υ resonances, $11 < m_{\mu^+\mu^-} < 20$ GeV. We have applied the following event selection criteria to select QED events. Events are passed through the "HLT_PASingleMuOpen_HFOneTowerVeto_v1" trigger. In addition, we have applied kinematic cuts similar to the Υ selection. Muon kinematic cuts are $p_T^\mu > 3.3$ GeV, $|\eta_\mu| < 2.2$, $p_T(\mu^+\mu^-) < 0.15$ GeV and $|y_{\mu^+\mu^-}| < 2.2$. The MC is normalized by integrated luminosity to compare with the data.

The QED cross-section from data is estimated by subtracting the non-exclusive background from the fit of the acoplanarity distribution of muons. Fig. 8.2 shows that the QED and non-exclusive background are very distinct. Hence this distribution is very helpful to extract exclusive QED process in the data compared to the other kinematic distribution. The acoplanarity distributions of QED from STARLIGHT MC is fitted with two exponential distribution

$$dN/dAco = f_1 \exp(a_1 \cdot Aco) + f_2 \exp(a_2 \cdot Aco) \quad (8.1)$$

where $Aco=1 - |\Delta\phi|/\pi$ of μ^+ and μ^- . The data is fitted with three exponentials, assuming the non-exclusive contribution behaves like an exponential in acoplanarity, and the elastic or exclusive part is given by two exponentials as given by Eq. 8.1. The form of the fitted function of data is given below where a_1 and a_2 parameters are taken from the fit of STARLIGHT MC

(Eq. 8.1),

$$dN/dAco = g_1 \exp(a_1 \cdot Aco) + g_2 \exp(a_2 \cdot Aco) + g_3 \exp(a_3 \cdot Aco). \quad (8.2)$$

The non-exclusive contribution is estimated from the integral of the third exponential of Eq. 8.2, and subtracted from data to get the exclusive (elastic) contribution N^{exc} . The QED cross-section thus estimated from N^{exc} by the following way,

$$\frac{d\sigma}{dy} = \frac{N^{\text{exc}}}{L_{\text{int}} \Delta y (A \times \epsilon_{MC}) \times C^{SF}}, \quad (8.3)$$

where $A \times \epsilon_{MC}$ is estimated from Starlight MC, $L_{\text{int}} = 173.4 \text{ nb}^{-1}$, $\Delta y = 4.4$. Details of $A \times \epsilon_{MC}$ and C^{SF} are given in Section 6.4 and Section 8.6 respectively. The comparison of the QED cross-section estimated from data and STARLIGHT MC is given in Table 8.1. The cross-section from data is found to be consistent with the cross-section from STARLIGHT MC.

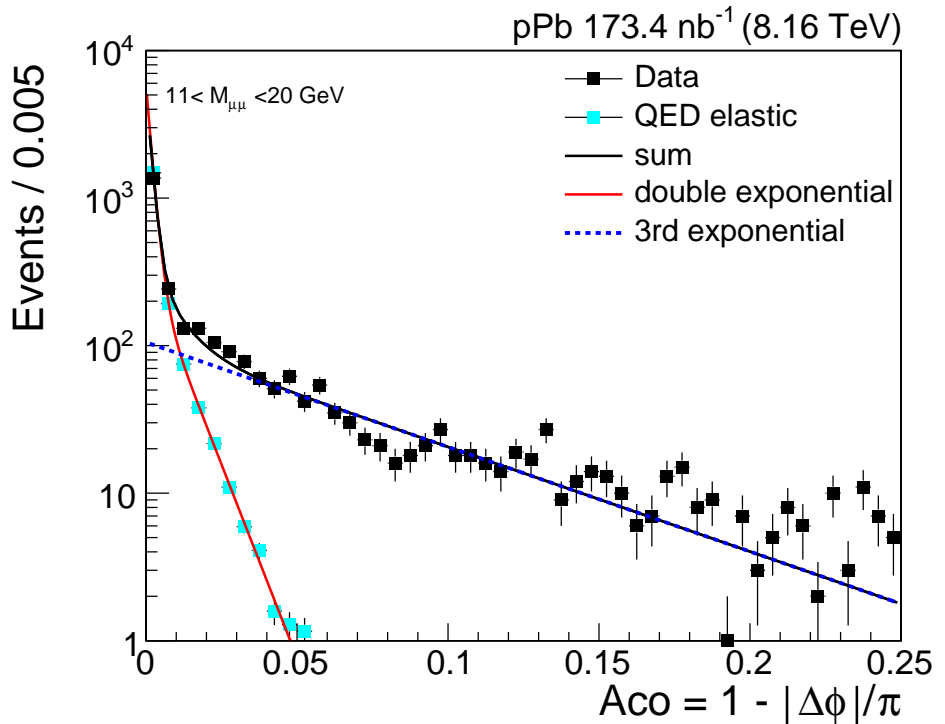


Figure 8.2: Acoplanarity distribution of dimuons for pPb added with the Pbp run flipped leading to integrated luminosity of 173.4 nb^{-1} for the sideband region, $11 < M_{\mu^+\mu^-} < 20 \text{ GeV}$. Data is compared with the simulated sample from STARLIGHT considering QED $\gamma\gamma \rightarrow \mu^+\mu^-$.

Table 8.1: QED cross-section from Data and MC in the dimuon rapidity region $|y| < 2.2$.

Run	N_{exc}	$A \times \varepsilon_{MC}$	Data $d\sigma/dy(\text{nb})$	STARLIGHT $d\sigma/dy (\text{nb})$
pPb+Pbp	1814 ± 43	0.135 ± 0.001	16.92 ± 0.39	17.5

8.2 γPb background

Additional background in this analysis originates from a small contribution of exclusive $\gamma\text{Pb} \rightarrow \Upsilon\text{Pb}$ events. It is estimated using the STARLIGHT Υ MC sample, details are given in Table 8.3 and Table 8.4. It has a 24% contribution relative to the data in the lowest dimuon p_T bin.

8.3 Non-exclusive background

We have also taken into account the contribution of semi-exclusive background (proton-dissociation) and inclusive background in the dimuon mass region $9.1 < M_{\mu^+\mu^-} < 9.7 \text{ GeV}$. In this process, particles are produced outside the CMS detector acceptance (in particular along the beam direction) and have additional hadronic activity below the detection thresholds. A proton-dissociation dominated template is constructed using events with only two muon tracks in the tracker and HF activity above 10 GeV [76] in the direction of the outgoing proton. We have considered a data-driven template for the inclusive process that satisfies the kinematic selection criteria, but with more than two tracks having track $p_T^\mu > 0.5 \text{ GeV}$. To measure the non-exclusive background contribution, a sum of the following distributions is fitted to the reconstructed data $p_T(\mu^+\mu^-)$ distribution, up to $p_T(\mu^+\mu^-) = 5 \text{ GeV}$: the exclusive $\Upsilon(1S)$ signal and QED ($\gamma\gamma \rightarrow \mu^+\mu^-$) continuum from STARLIGHT MC, the proton-dissociation and inclusive template from data-driven background. The fit determines the normalization of each of these components. The result of the fit is shown in Fig. 8.3 and Fig. 8.4. The normalized proton-dissociation template describes well the region of high dimuon $p_T(\mu^+\mu^-)$ in the data. The fractional proton-dissociation background contribution (f_{PD}) is estimated in all four bins

of $p_T(\mu^+\mu^-)$ and $y_{\mu^+\mu^-}$ and used for the signal cross-section extraction. The details are given in Table 8.2.

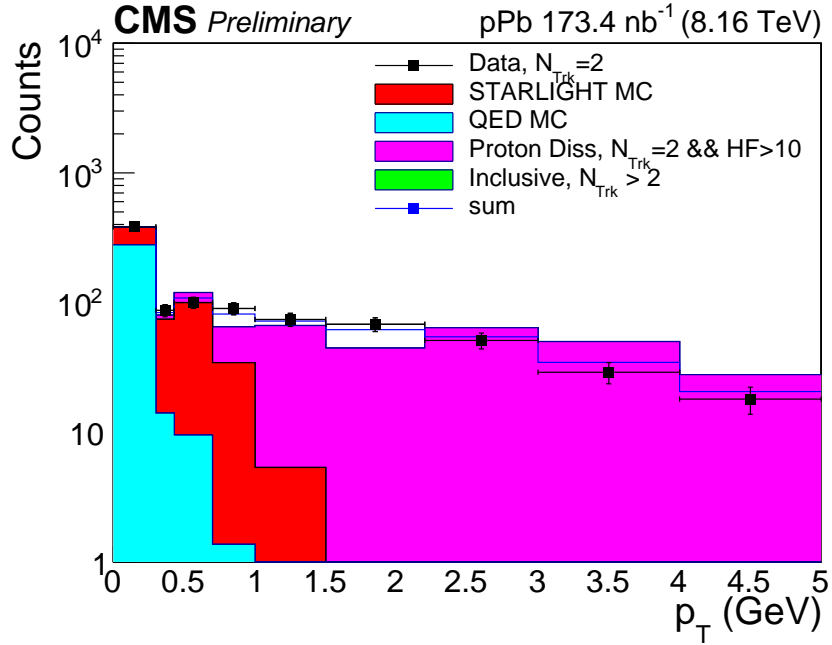


Figure 8.3: Simultaneous fitting of proton-dissociation and inclusive background template within the rapidity range $|y_{\mu^+\mu^-}| < 2.2$ using TFraction fitter [83] function. Here first 4- $p_T(\mu^+\mu^-)$ bins are chosen corresponding to the bins used for the signal cross-section extraction

Table 8.2: Proton-dissociation contribution in signal region

$p_T(\mu^+\mu^-)$ bin	f_{PD}	rapidity bin	f_{PD}
0.0,0.3	0.00 ± 0.00	-2.2, -1.23	0.09 ± 0.04
0.3,0.43	0.06 ± 0.04	-1.23,-0.18	0.11 ± 0.04
0.43,0.7	0.19 ± 0.08	-0.18, 0.76	0.06 ± 0.03
0.7,1.0	0.34 ± 0.11	0.76, 2.2	0.11 ± 0.05

From Fig. 8.3, we can see that the proton-dissociation contribution is increasing gradually with dimuon p_T as expected. As a result of the fit, there is no inclusive contribution found in the signal region. We used the TFraction fitter [83] function (incorporated in ROOT analysis program) for individual normalization of MC samples and data driven templates. Details of the TFraction fitter are discussed below.

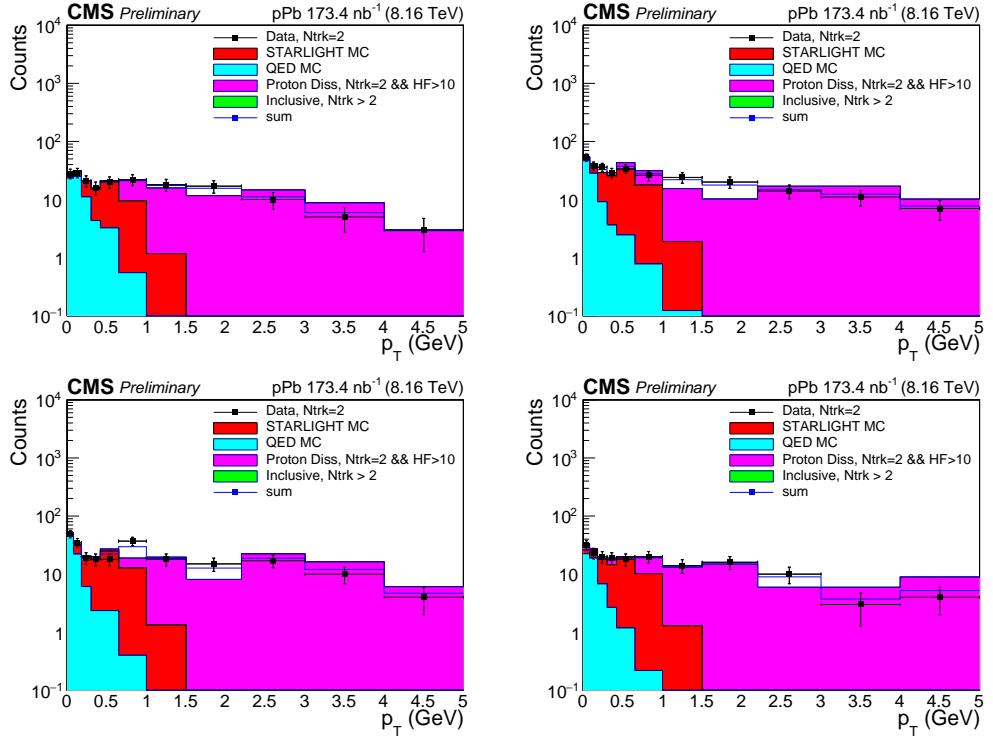


Figure 8.4: Simultaneous fitting of proton-dissociation and inclusive background template using TFraction fitter [83] function. Fitting is done in the following 4-rapidity range: (a) $-2.2 < y_{\mu^+\mu^-} < -1.23$ (upper left plot), (b) $-1.23 < y_{\mu^+\mu^-} < -0.18$ (upper right plot), $-0.18 < y_{\mu^+\mu^-} < 0.76$ (lower left plot), $0.76 < y_{\mu^+\mu^-} < 2.2$ (lower right plot)

TFraction fitter: Data should match with the MC templates if the shape of the individual templates is appropriately modeled and normalized. The number of predicted MC events in bin j is given by

$$f_j = \sum_i P_i A_{ij}. \quad (8.4)$$

Where i represents the 4-histogram templates, A_{ij} is the expected no. of events in bin j of histogram i and P_i is the histogram scaling factor, which we evaluate from the fitting. The observed number of events is represented by a_{ij} for each A_{ij} . The probability of the observed data (n_j) and observed MC (a_{ij}) is now the total likelihood.

$$\ln \mathcal{L} = \sum_j [(n_j \ln f_j - f_j) + \sum_i (a_{ij} \ln A_{ij} - A_{ij})]. \quad (8.5)$$

The value of P_j and A_{ij} are estimated by maximizing this likelihood.

8.4 Feed-down background

Feed-down is a transition from a higher energy state to a lower energy state, and the transition is allowed in quantum mechanics. In this analysis, we will talk about the feed-down of the $\Upsilon(2S)$ state. The $\Upsilon(2S)$ feed-down background in $\Upsilon(1S)$ selection is estimated using MC simulation. Initial p_T and y distributions of $\Upsilon(2S)$ are taken from the STARLIGHT generator and shown in Fig. 8.5. They are given input to PYTHIA and decayed to $\Upsilon(1S) + \pi^+ \pi^-$ with branching ratio 0.189 and to $\Upsilon(1S) + \pi^0 \pi^0$ with branching ratio 0.086. $\Upsilon(1S)$ then decayed to $\mu^+ \mu^-$ and simulated and reconstructed through CMS detector using CMSSW framework. After applying all selection cuts, the number of dimuons from feed down from $\Upsilon(2S)$ are found to be 7% of the exclusive signal $\Upsilon(1S)$. The contribution from feed-down of exclusive χ_b states was neglected, as these double-pomeron processes (or $\gamma\gamma \rightarrow \chi_b \chi_b$ processes, with very small cross-sections) are expected to be strongly suppressed in proton-nucleus collisions [84, 85]. Also, We didn't check the $\Upsilon(3S) \rightarrow \Upsilon(2S) \rightarrow \Upsilon(1S)$ decay process as the branching function (BR) of this decay process is very low ($BR \sim 10^{-4}$). Hence, the feed-down contribution of this decay process is negligible. We can understand it better if we look into branching fraction of individual sub-decay process listed below: $\Upsilon(3S) \rightarrow \Upsilon(2S) + \text{anything}$, BR: 10.6%; $\Upsilon(2S) \rightarrow \Upsilon(1S) + X$ (where, $X = \pi^+ \pi^-$ or $\pi^0 \pi^0$), BR: (17.9+8.6)%; $\Upsilon(1S) \rightarrow \mu^+ \mu^-$, BR: 2.48%. So, the branching fraction of this decay process is about $BR = (10.6\% \times 26.5\% \times 2.48\%) = 7 \times 10^{-4}$.

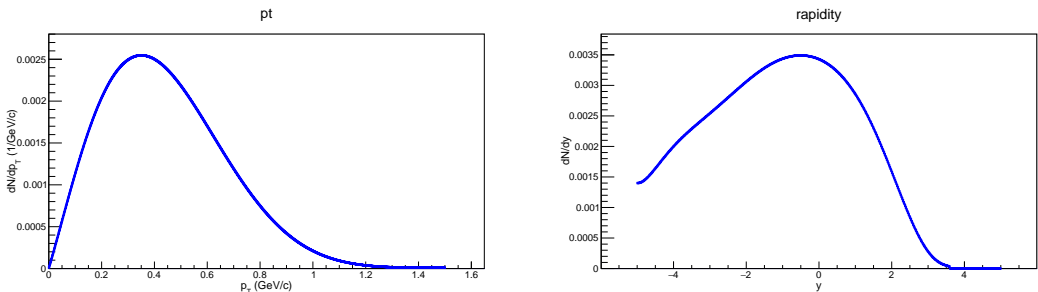


Figure 8.5: Input distribution of signal $\Upsilon(2S)$ from STARLIGHT MC, which are being decayed with PYTHIA as $\Upsilon(2S) \rightarrow \Upsilon(1S) + X$ ($\pi^+ \pi^-$ or $\pi^0 \pi^0$).

8.5 Background subtraction

Initially, we have obtained the number of $\Upsilon(1S)$ from the invariant mass fitting of data in the dimuon p_T region $p_T(\mu^+\mu^-) < 1.0$ GeV. The extracted number of $\Upsilon(1S)$ includes a mix of exclusive and non-exclusive $\Upsilon(1S)$ candidates, giving $N_{\Upsilon(1S)}^{fit}$. Thereafter, the non-exclusive contributions and γPb were subtracted from the $N_{\Upsilon(1S)}^{fit}$ candidates. The background subtracted number of $\Upsilon(1S)$ coming from γp interactions can be written as $N_{\Upsilon(1S)}^{bkg-sub} = N_{\Upsilon(1S)}^{fit} \times (1 - f_{PD}) - N_{\Upsilon(1S)}^{\gamma Pb}$. All these contributions are listed in Table 8.3 and Table 8.4.

Table 8.3: Number of events in $p_T^2(\mu^+\mu^-)$ bins for data and all backgrounds

$p_T^2(\mu^+\mu^-)$ bin	Data	PD	γPb	Bkg sub Data
0.0,0.09	85	0	20	65
0.09,0.19	53	3	1	49
0.19,0.49	52	10	1	42
0.49,1.00	57	19	0	38

Table 8.4: Number of events in rapidity bins for data and all backgrounds

rapidity bin	Data	PD	γPb	Bkg sub Data
-2.2,-1.23	51	5	4	42
-1.23,-0.18	72	8	7	57
-0.18,0.76	61	4	6	51
0.76,2.2	58	6	6	46

8.6 Extraction of cross-sections

The number of exclusive $\Upsilon(1S)$ ($N_{\Upsilon(1S)}^{exc}$) coming from γp interactions is extracted as

$$N_{\Upsilon(1S)}^{exc} = \frac{N_{\Upsilon(1S)}^{bkg-sub}}{(1 + f_{FD}) \times (A \times \varepsilon_{MC}) \times C^{SF}} \quad (8.6)$$

where f_{FD} is the feed-down fraction for the decay of $\Upsilon(2S)$ to $\Upsilon(1S)$ mesons and C^{SF} defined as follows

$$C^{SF} = (SF^{Trig.})^2 (SF^{muonID})^2 (SF^{Track})^2 \quad (8.7)$$

Where the scale factor (SF) is the ratio of efficiency from data and MC, $SF = \frac{\varepsilon_{Data}}{\varepsilon_{MC}}$. The obtained values of the scale factors from single muon trigger, muonID and tracker muon are 1.01 ± 0.013 , 0.99 ± 0.001 and 1.02 ± 0.002 respectively. The $|t|$ - and y -differential cross sections are extracted for the $\Upsilon(1S)$ state as follows

$$\frac{d\sigma_{\Upsilon(1S)}}{d|t|} \mathcal{B}_{\Upsilon(1S) \rightarrow \mu^+ \mu^-} = \frac{N_{\Upsilon(1S)}^{\text{exc}}}{\mathcal{L} \times \Delta|t|}, \quad \text{and} \quad (8.8)$$

$$\frac{d\sigma_{\Upsilon(1S)}}{dy} = \frac{N_{\Upsilon(1S)}^{\text{exc}}}{\mathcal{B}_{\Upsilon(1S) \rightarrow \mu^+ \mu^-} \times \mathcal{L} \times \Delta y}, \quad (8.9)$$

where $N_{\Upsilon(1S)}^{\text{exc}}$ denotes the background-subtracted, feed-down and $A \times \varepsilon_{MC}$ corrected number of signal events in each $|t|$ and y bin, \mathcal{L} is the integrated luminosity, $\Delta|t|$ and Δy are the widths of each $|t|$ and y bins, and $\mathcal{B}_{\Upsilon(1S) \rightarrow \mu^+ \mu^-}$ the dimuon branching fraction. The $|t|$ - and y -differential cross sections are measured without branching fraction correction so that we can compare with the 5.02 TeV cross-section [45].

Finally, the exclusive $\Upsilon(1S)$ photo-production cross section as a function of photon-proton center-of-mass energy $W_{\gamma p} = \sqrt{2E_p M_\Upsilon \exp(y)}$, is obtained from the $d\sigma_{\Upsilon(1S)}/dy$ cross section through the relation

$$\sigma_{\gamma p \rightarrow \Upsilon(1S)p}(W_{\gamma p}^2) = \frac{1}{\Phi} \frac{d\sigma_{\Upsilon(1S)}}{dy}, \quad (8.10)$$

where each one of the four rapidity bins, $-2.2 < y_{\mu^+ \mu^-} < -1.23$, $-1.23 < y_{\mu^+ \mu^-} < -0.18$, $-0.18 < y_{\mu^+ \mu^-} < 0.76$ and $0.76 < y_{\mu^+ \mu^-} < 2.2$ considered, corresponds to a given $W_{\gamma p}$ interval: $117 < W_{\gamma p} < 213$, $213 < W_{\gamma p} < 351$, $351 < W_{\gamma p} < 498$, and $498 < W_{\gamma p} < 1054$ GeV respectively. The cross sections are given at the value W_0 , which corresponds to the average pseudorapidity over a bin, $\langle y \rangle$. The photon flux Φ in Eq. (8.10), evaluated at $\langle y \rangle$, is obtained from STARLIGHT

and calculated in the impact parameter space requiring the pPb separation to be larger than the sum of their radii.

Chapter 9

Systematic uncertainties

Systematic uncertainties are connected with the nature of the measuring instrument, assumptions made by the researcher, or the model used to make predictions. It's crucial to measure as the source of systematic uncertainties differs from experiment to experiment. Several sources of systematic uncertainty are considered. The uncertainty in the measurements of all differential and total Υ meson production cross-sections, as well as for the extraction of the exponential slope b of the $|t|$ spectrum is discussed below and summarized in Table 9.1.

- The muon reconstruction and selection efficiency have uncertainties from three sources: the efficiency to find a track in the inner tracker, the efficiency to pass the track quality requirements, and the probability of passing the HLT selection. These efficiencies are estimated using the "tag-and-probe" method. The associated systematic uncertainty is estimated from the difference in efficiencies obtained from the data and simulation. It leads to a 6% uncertainty in the normalization of the cross-sections but no effect on the b measurement.
- To estimate the systematic uncertainty due to the model dependence of the product of the detector acceptance and efficiency ($A \times \epsilon_{MC}$) correction, the parameters b and δ of the simulated STARLIGHT spectra are changed by $\pm 30\%$ (chosen conservatively by the

uncertainties of the corresponding fits to the data), and the resulting MC distributions are used for the determination of the factor $A \times \epsilon_{\text{MC}}$, resulting in 1.9–14.8% changes in the measured observables.

- The uncertainty associated with the nonexclusive background contributions is estimated by varying the HF energy threshold by ± 1 GeV. The resulting uncertainties of the observables vary between 1.7% and 10.7%.
- The uncertainty introduced by the $\Upsilon(2S) \rightarrow \Upsilon(1S) + X$ feed-down is estimated by modifying the values of the b and δ parameters of the $\Upsilon(2S)$ spectra in the STARLIGHT MC simulation to match with the data. This resulted in a $\pm 0.5\%$ variation of the $\Upsilon(1S)$ cross-sections.
- The $\Upsilon(1S) \rightarrow \mu^+ \mu^-$ branching fraction is taken from the PDG world average [79]. It contributes 2% uncertainties on the measurement of the $\Upsilon(1S)$ cross-sections.
- The theoretical uncertainty in the photon flux is estimated by changing the Pb radius by ± 0.5 fm, corresponding to the nuclear skin thickness [86]. This only affects the total cross-section $\sigma_{\gamma p \rightarrow \Upsilon(1S)p}$. It amounts to 1.7, 2.2, 3.3, and 6.3% in the four $W_{\gamma p}$ bins, respectively. The photon flux is estimated in impact parameter space, with the probability of no hadronic interactions convolved. The photon flux uncertainty (listed in the bottom row of Table 12.2) is more prominent for higher photon energies since smaller impact parameters dominate them. Specifically, it reduces the probability of no hadronic interactions with the impact parameters close to the Pb radius.
- The uncertainty in the integrated luminosity determined by the van der Meer scan is $\pm 3.5\%$ [87]. It impacts the normalization of differential and total cross-sections but does not affect the b slope uncertainty.

Systematic plots are shown in Fig. 1-6 of Appendix .1. The dominant sources are the muon reconstruction efficiency, Acceptance \times efficiency, and the nonexclusive backgrounds' modelling. The total uncertainty is calculated by adding in quadrature the individual contributions, and varies between $\pm 10.9\%$ for the b slope to $\pm 9\%$ for $\sigma_{\gamma p \rightarrow \Upsilon(1S)p}$. Given the limited integrated luminosity available, the measurements are dominated by statistical uncertainties. Details of minimum and maximum systematic error per source is given in Table 9.2. We haven't

Table 9.1: Relative systematic uncertainties in the measurements of $\mathcal{B}_{\Upsilon(1S) \rightarrow \mu^+ \mu^-} d\sigma_{\Upsilon(1S)} / d|t|$, the exponential b slope of the $|t|$ spectrum, $d\sigma_{\Upsilon(1S)} / dy$, and $\sigma_{\gamma p \rightarrow \Upsilon(1S)p}$. Individual contributions, as well as total systematic uncertainties added in quadrature, are presented. For the $|t|$ - and y -differential cross-sections, the values averaged over all bins are shown.

Source	$\mathcal{B}_{\Upsilon \rightarrow \mu^+ \mu^-} d\sigma/d t $	b	$d\sigma_{\Upsilon(1S)}/dy$	$\sigma_{\gamma p \rightarrow \Upsilon(1S)p}$
Muon efficiency	$\pm 6\%$	–	$\pm 6\%$	$\pm 6\%$
Acceptance \times efficiency	$\pm 14.8\%$	$\pm 1.9\%$	$\pm 3.8\%$	$\pm 3.8\%$
Nonexclusive background	$\pm 3.5\%$	$\pm 10.7\%$	$\pm 1.7\%$	$\pm 1.7\%$
Integrated luminosity	$\pm 3.5\%$	–	$\pm 3.5\%$	$\pm 3.5\%$
Feed-down	–	–	$\pm 0.5\%$	$\pm 0.5\%$
Branching fraction $\mathcal{B}_{\Upsilon(1S) \rightarrow \mu^+ \mu^-}$	–	–	$\pm 2.0\%$	$\pm 2.0\%$
Photon flux Φ	–	–	–	$\pm 3.4\%$
Total	$\pm 16.7\%$	$\pm 10.9\%$	$\pm 8.4\%$	$\pm 9.0\%$

Table 9.2: Relative systematic uncertainties in the measurements of $\mathcal{B}_{\Upsilon(1S) \rightarrow \mu^+ \mu^-} d\sigma_{\Upsilon(1S)} / d|t|$, the exponential b slope of the $|t|$ spectrum, $d\sigma_{\Upsilon(1S)} / dy$, and $\sigma_{\gamma p \rightarrow \Upsilon(1S)p}$. Minimum and maximum systematic error per source, as well as total systematic uncertainties added in quadrature, are presented. For the $|t|$ - and y -differential cross-sections, the values averaged over all bins are shown.

Source	$\mathcal{B}_{\Upsilon \rightarrow \mu^+ \mu^-} d\sigma/d t $		b		$d\sigma_{\Upsilon(1S)}/dy$		$\sigma_{\gamma p \rightarrow \Upsilon(1S)p}$	
Source	Max	Min	Max	Min	Max	Min	Max	Min
Muon efficiency	$\pm 6\%$	$\pm 6\%$	–	–	$\pm 6\%$	$\pm 6\%$	$\pm 6\%$	$\pm 6\%$
Acceptance \times efficiency	$\pm 17.4\%$	$\pm 12.2\%$	$\pm 3.7\%$	$\pm 0.1\%$	$\pm 5.9\%$	$\pm 1.8\%$	$\pm 5.9\%$	$\pm 1.8\%$
Nonexclusive background	$\pm 4.8\%$	$\pm 2.1\%$	$\pm 18.4\%$	$\pm 3.1\%$	$\pm 2.2\%$	$\pm 1.1\%$	$\pm 2.2\%$	$\pm 1.1\%$
Integrated luminosity	$\pm 3.7\%$	$\pm 3.3\%$	–	–	$\pm 3.6\%$	$\pm 3.4\%$	$\pm 3.6\%$	$\pm 3.4\%$
Feed-down	–	–	–	–	$\pm 0.5\%$	$\pm 0.5\%$	$\pm 0.5\%$	$\pm 0.5\%$
Branching fraction $\mathcal{B}_{\Upsilon(1S) \rightarrow \mu^+ \mu^-}$	–	–	–	–	$\pm 2.1\%$	$\pm 1.9\%$	$\pm 2.1\%$	$\pm 1.9\%$
Photon flux Φ	–	–	–	–	–	–	$\pm 3.9\%$	$\pm 2.9\%$
Total	$\pm 19.4\%$	$\pm 14.1\%$	$\pm 18.8\%$	$\pm 3.1\%$	$\pm 9.7\%$	$\pm 7.5\%$	$\pm 10.4\%$	$\pm 8.0\%$

use asymmetric errors as we have taken average of minimum and maximum systematic error contribution in each bin of a variable(Ex. $|t|$, y and $W_{\gamma p}$).

Chapter 10

Results

10.1 Differential cross-section as a function of $|t|$ and y

The differential cross-sections for exclusive $\Upsilon(1S)$ photo-production, $\mathcal{B}_{\Upsilon(1S) \rightarrow \mu^+ \mu^-} d\sigma_{\Upsilon(1S)}/d|t|$ and $d\sigma_{\Upsilon(1S)}/dy$, measured in the range $|y| < 2.2$ are tabulated in Table 10.1. The $|t|$ -differential cross-section is fitted with an exponential function of the form $e^{-b|t|}$ in the region $p_T^2 < 1.0 \text{ GeV}^2$, using a χ^2 goodness-of-fit minimization method. The result of the fit for $\Upsilon(1S)$ is shown in Fig. 10.1. We have obtained the slope value to be $b = 3.99 \pm 1.25(\text{stat}) \pm 0.43(\text{syst}) \text{ GeV}^{-2}$. In Fig. 10.1, the errors displayed in the legend is just a fit error after adding systematic error along with statistical error of differential cross-section for $\Upsilon(1S)$ in each p_T^2 bin. The slope parameter value is $b = 3.99 \pm 1.25 \text{ GeV}^{-2}$ before taking account the systematic contribution. Both ZEUS and CMS extracted the slope parameter in previous measurements using the same exponential fit and they found the value of the slope $b = 4.3^{+2.0}_{-1.3}(\text{stat})^{+0.5}_{-0.6}(\text{syst}) \text{ GeV}^{-2}$ [42] and $b = 6.0 \pm 2.1(\text{stat}) \pm 0.3(\text{syst}) \text{ GeV}^{-2}$ [45], respectively. This result is in good agreement with the ZEUS [42] and CMS (5.02 TeV) [45] experimental results and with the predictions of pQCD-based models [29]. In the pQCD model, the value of slope parameter b is approximately

4.63 GeV^{-2} .

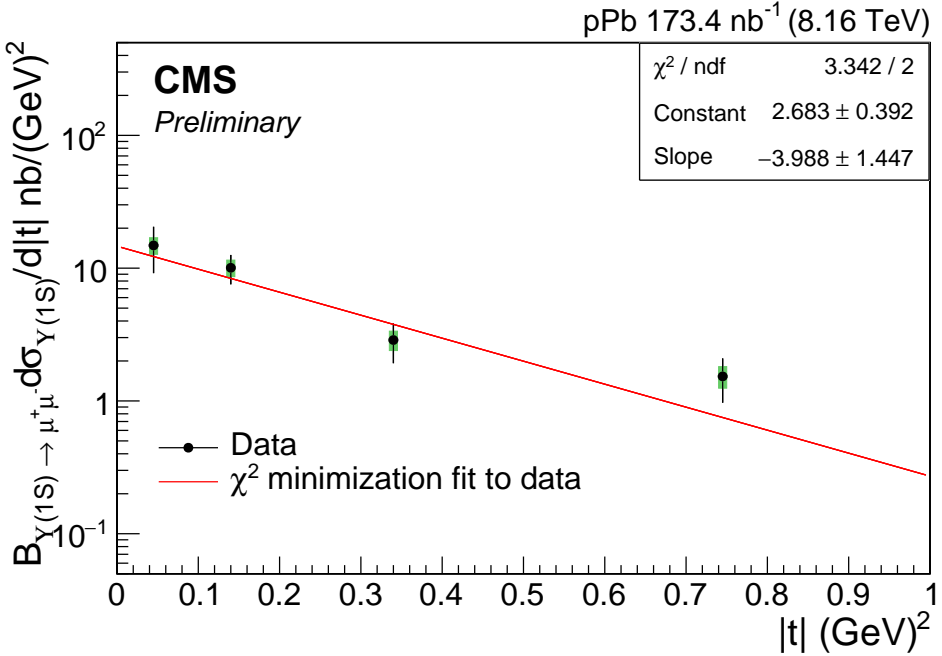


Figure 10.1: Differential $\Upsilon(1\text{S}) \rightarrow \mu^+\mu^-$ photo-production cross-section as a function of $|t|$ measured in pPb collisions at $\sqrt{s_{\text{NN}}} = 8.16 \text{ TeV}$. In this plot, the data points are placed along the abscissa following the prescription of [88], and the solid line is an exponential fit of the form $e^{-b|t|}$. The vertical bars represent the statistical and systematic uncertainties added in quadrature and the boxes represent the systematic uncertainties.

Figure 10.2 shows the differential cross-section of $\Upsilon(1\text{S})$ with rapidity. The $\Upsilon(1\text{S})$ cross-section is obtained using the Eq. (8.9) in the four rapidity bins. The relevant input parameters to Eq. (8.9) are listed in Table 10.2. We compared the CMS results to the following theoretical predictions:

- The factorized impact parameter saturation model, fIPsat, with an eikonalized gluon distribution function that uses the colour glass condensate (CGC) formalism to incorporate gluon saturation at low- x [36, 37]. CGC is a dense gluonic state (density of gluons saturate) in hadrons which universally appear in the high energy limit of scattering;
- The Iancu, Itakura and Munier (IIM) colour dipole formalism [89] with two sets of meson wave functions, boosted Gaussian (BG) and light-cone Gaussian (LCG), which also

Table 10.1: Differential exclusive $\Upsilon(1S) \rightarrow \mu^+ \mu^-$ photo-production cross-sections in four $|t|$ and y bins. The first and second uncertainties correspond to statistical and systematic components, respectively.

$ t $ bin (GeV^2)	$\mathcal{B}_{\Upsilon(1S) \rightarrow \mu^+ \mu^-} d\sigma_{\Upsilon}/d t $ (nb/ GeV^2)	y bin	$d\sigma_{\Upsilon(1S)}/dy$ (nb)
(0.00, 0.09)	$14.8 \pm 5.3 \pm 2.11$	(-2.2, -1.23)	$28.28 \pm 8.08 \pm 2.39$
(0.09, 0.19)	$10.1 \pm 2.1 \pm 1.44$	(-1.23, -0.18)	$22.69 \pm 5.97 \pm 1.31$
(0.19, 0.49)	$2.9 \pm 0.8 \pm 0.48$	(-0.18, 0.76)	$23.62 \pm 5.09 \pm 1.41$
(0.49, 1.00)	$1.5 \pm 0.5 \pm 0.29$	(0.76, 2.2)	$16.28 \pm 3.89 \pm 0.90$

incorporate saturation effects [34, 35]. The colour dipole framework is based on the factorization of the high energy scattering amplitude into an initial and final state wave function and scattering amplitude of color dipole (i.e. $q\bar{q}$ pair). In this model, the gluon saturation effect is incorporated in the dipole cross-section term.

As shown in Fig. 10.2, the IIM-BG and IIM-LCG theoretical predictions are consistent with the data, within the relatively large experimental uncertainties.

10.2 Cross-section as a function of $W_{\gamma p}$

Fig. 10.3 shows the $\sigma_{\gamma p \rightarrow \Upsilon(1S)p}$ cross-section as a function of $W_{\gamma p}$ obtained using Eq. (8.10). The measured cross-sections are compared with the previous measurements from H1 [40], ZEUS [39, 41], LHCb [44] and CMS [45], and the three model predictions described in the previous section. The CMS results (listed in Table 10.2) cover the range of energies between HERA and LHCb data. As $\sigma(W_{\gamma p})$, to first approximation is proportional to the square of the gluon density of the proton, and since the gluon distribution at low Bjorken- x is well described by a power law, the cross-section also follows a power-law energy dependence. A fit of the extracted CMS $\sigma_{\gamma p \rightarrow \Upsilon(1S)p}$ cross-section with a function of the form $A (W_{\gamma p} [\text{GeV}] / 400)^{\delta}$ (with the constant A corresponding to the cross-section at the middle value, $W_{\gamma p} = 400 \text{ GeV}$, over the range of energies covered) gives $\delta = 0.63 \pm 0.25$ and $A = 381 \pm 51 \text{ pb}$ (red solid line in Fig 10.3), consistent with the value $\delta = 1.2 \pm 0.8$ obtained by ZEUS [41]. A similar fit to the CMS (8.16 TeV), CMS (5.02 TeV) [45], H1 [40], ZEUS [41], and including the higher-

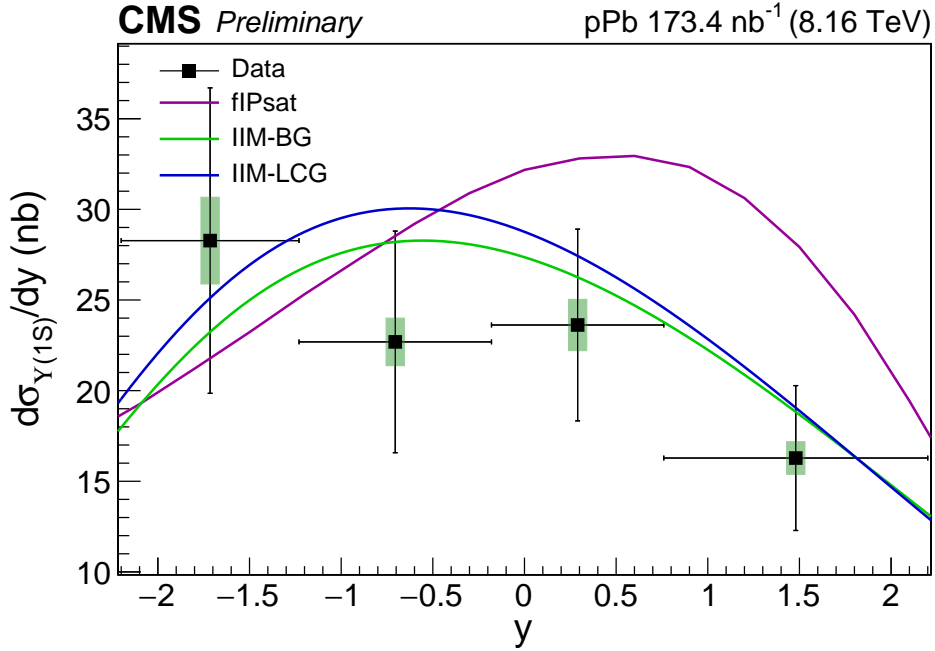


Figure 10.2: Differential $\Upsilon(1S)$ photo-production cross-section as a function of rapidity measured in pPb collisions at $\sqrt{s_{\text{NN}}} = 8.16$ TeV in the dimuon rapidity region $|y| < 2.2$, compared to various theoretical predictions [29, 34–38]. The horizontal bars are plotted to indicate the width of each y bin. The vertical bars represent the statistical and systematic uncertainties added in quadrature and the boxes represent the systematic uncertainties.

$W_{\gamma p}$ LHCb data together gives $\delta = 0.74 \pm 0.14$, in good agreement with the results of the fit to the CMS data alone. Also, the fit parameter $\delta = 0.63 \pm 0.25$ from CMS (8.16 TeV) data is consistent with the value $\delta = 0.68 \pm 0.06$ measured in the ALICE [80] experiment for J/ψ photo-production.

Figure 10.3 also shows theoretical predictions from the fIPsat, and IIM models. The IIM-LCG calculations are consistent with the CMS measurement. But the fIPsat model predicts a higher cross-section than that measured by LHCb and in this thesis. These results put a new constraint for the evolution of the gluon density at low Bjorken- x in the proton.

Table 10.2: Values of the $\Upsilon(1S)$ photo-production cross-section in four rapidity y bins, corresponding to four photon-proton $W_{\gamma p}$ centre-of-mass energy ranges (with central W_0 value obtained following [88]), in pPb collisions at $\sqrt{s_{NN}} = 8.16 \text{ TeV}$. The symbols $N_{\Upsilon(1S)}^{\text{back-sub}}$, and $N_{\Upsilon(1S)}^{\text{exc}}$ represent the numbers of $N_{\Upsilon(1S)}$ candidates after background subtraction, and Acceptance \times Efficiency corrected factor, respectively; $N_{\Upsilon(1S)}$ is the extracted number of $\Upsilon(1S)$ mesons, and Φ is the theoretical effective photon flux (see text). The first (second, if given) uncertainty quoted corresponds to the statistical (systematic) component.

y range	(-2.2,-1.23)	(-1.23,-0.18)	(-0.18,0.76)	(0.76,2.2)
$N_{\Upsilon(1S)}^{\text{back-sub}}$	42 ± 12	57 ± 15	51 ± 11	46 ± 11
$A \times \epsilon_{MC}$	0.32 ± 0.005	0.50 ± 0.007	0.48 ± 0.007	0.41 ± 0.006
$N_{\Upsilon(1S)}^{\text{exc}}$	$123 \pm 35 \pm 1$	$107 \pm 28 \pm 2$	$99 \pm 21 \pm 2$	$105 \pm 25 \pm 1$
$W_{\gamma p}$ range (GeV)	117–190	190–321	321–513	513–1054
W_0 (GeV)	149	247	405	735
Photon flux (Φ)	125.7 ± 2.1	94.3 ± 2.2	63.6 ± 2.2	29.2 ± 1.8
$\sigma_{\gamma p \rightarrow \Upsilon(1S)p}$ (pb)	$225 \pm 64 \pm 19$	$240 \pm 63 \pm 15$	$371 \pm 80 \pm 26$	$558 \pm 133 \pm 47$

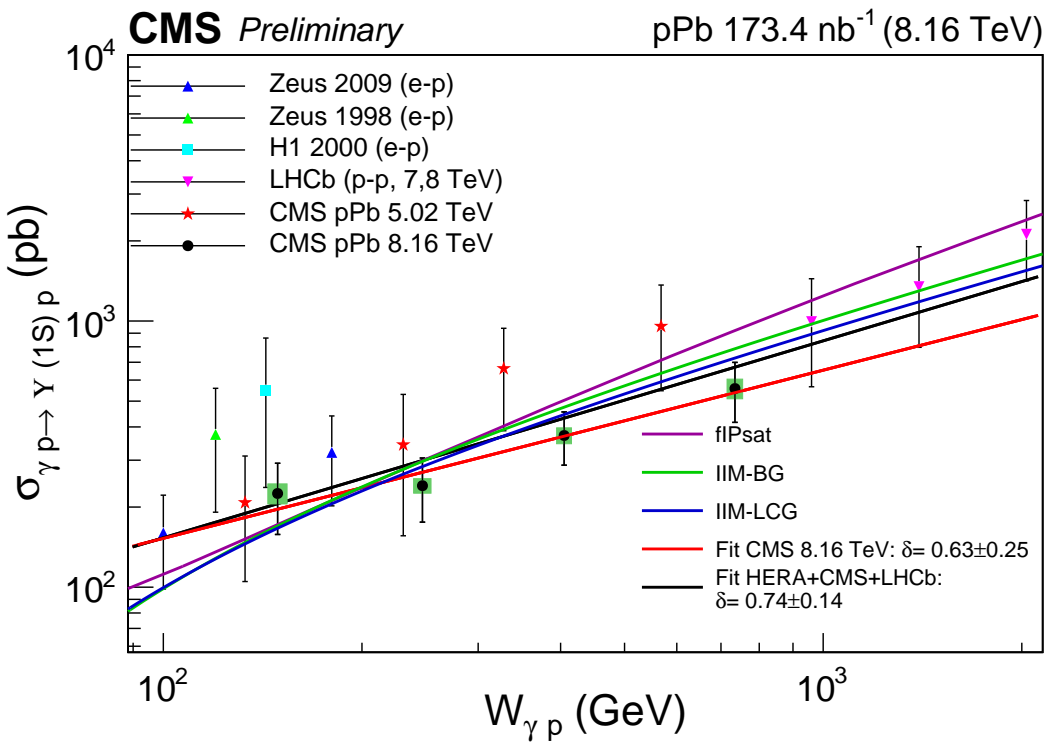


Figure 10.3: Cross-section for exclusive $\Upsilon(1S)$ photo-production, $\gamma p \rightarrow \Upsilon(1S)p$, as a function of photon-proton centre-of-mass energy, $W_{\gamma p}$, compared to previous HERA [39–41] and LHCb [44] data as well as to various theoretical predictions [29, 34–38]. The vertical bars represent the statistical and systematic uncertainties added in quadrature and the boxes represent the systematic uncertainties.

Chapter 11

Summary

This thesis reports the photo-production of exclusive $\Upsilon(1S)$ in ultra-peripheral pPb collisions at $\sqrt{s_{NN}} = 8.16$ TeV. Initially, we generated exclusive Υ events using the STARLIGHT MC generator and reconstructed those events using the CMSSW framework. It gives us an overview of the kinematics of generated and reconstructed exclusive Υ events. From a T&P study, we have seen that the single muon efficiency is good in the region $p_T^\mu > 3$ GeV and $|\eta_\mu| < 2.4$. The estimated single muon efficiency from T&P was then used to measure the scale factor (SF) that we further used to correct the efficiency measured from STARLIGHT MC. We looked into the data and estimated the number of $\Upsilon(1S)$ (i.e. $N_\Upsilon^{fit}(1S)$) from invariant mass fitting. $N_\Upsilon^{fit}(1S)$ consists of both exclusive and non-exclusive (proton-dissociation) contributions. We observed that the proton-dissociation contribution increases with p_T . We have measured the differential cross-section $\frac{d\sigma}{d|t|}$ and $\frac{d\sigma}{dy}$ of $\Upsilon(1S)$ within the detector acceptance $y < 2.2$. The $|t|$ spectrum is well described by an exponential function. We extracted the slope-parameter value $b = 3.99 \pm 1.25(\text{stat}) \pm 0.43(\text{syst})$ GeV $^{-2}$ of the exponential function. The result is consistent with the slope measurement at other centre-of-mass energies. We couldn't look into the energy dependency of the slope-parameter as the Υ yield is limited by statistics. But it's possible with the ongoing J/Ψ analysis at 8.16 TeV, which has more statistics. The

differential cross-section is in good agreement with the predictions of IIM-BG and IIM-LCG models [34, 35]. It implies that the choice of dipole cross-sections with incorporated gluon saturation effects, the wave function of the projectile and the outgoing state together describe it well. We measure the total cross-section $\sigma(W_{\gamma p})$ of $\Upsilon(1S)$ in the photon-proton centre-of-mass energy $117 < W_{\gamma p} < 1054$ GeV and the cross-section follows a power law ($\sigma \propto W_{\gamma p}^\delta$). The extracted value of $\delta = 0.63 \pm 0.25$ from the fit is in good agreement with the ZEUS result [41]. Thus the range of $W_{\gamma p}$ used in this measurement probes the low- x parton momentum fraction $x \approx 10^{-4} - 10^{-2}$ in the target proton. So, one can use these results for gluon PDF improvements. We look forward to the upcoming vector meson analysis with Run-3 data, which will have higher statistics.

.1 Appendix 1

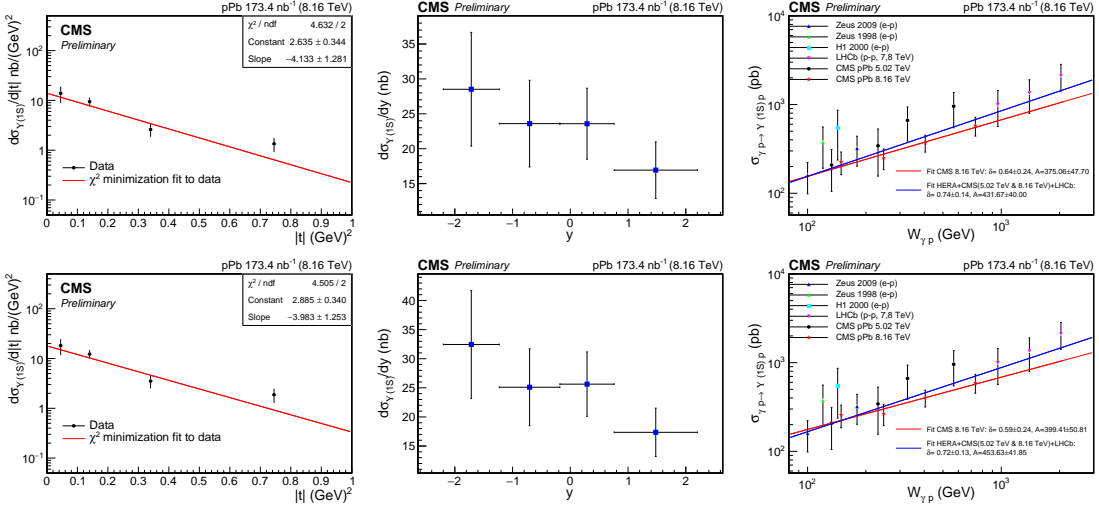


Figure 1: Differential cross-sections of $\Upsilon(1S)$ as a function of $|t|$ and y are shown in the left and the middle figure, respectively. The right figure shows the total cross-section of $\Upsilon(1S)$ as a function of $W_{\gamma p}$. The upper panel shows the cross-section corresponding to the +30% change of the parameters b and δ of the simulated STARLIGHT spectra. Similarly, the lower panel shows the cross-section corresponding to the -30% change of the parameters b and δ of the simulated STARLIGHT spectra. These plots are made to estimate systematic contribution corresponding to the model dependence of the product of the detector acceptance and efficiency.

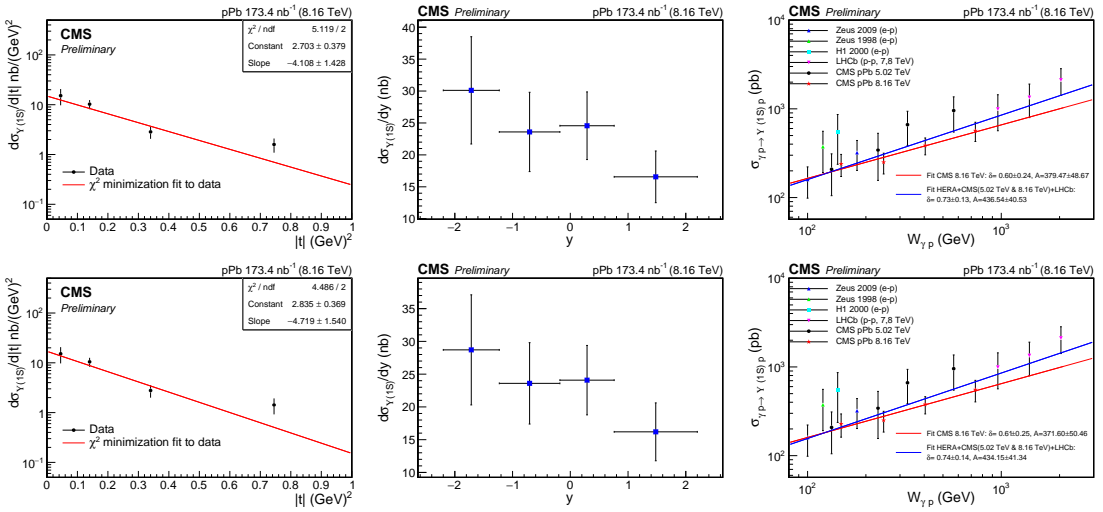


Figure 2: Differential cross-sections of $\Upsilon(1S)$ as a function of $|t|$ and y are shown in the left and the middle figure, respectively. The right figure shows the total cross-section of $\Upsilon(1S)$ as a function of $W_{\gamma p}$. The upper panel shows the cross-section corresponding to the +10% change of the HF threshold. Similarly, the lower panel shows the cross-section corresponding to the -10% change of the HF threshold. These plots are made to estimate systematic contribution corresponding to non-exclusive data driven template.

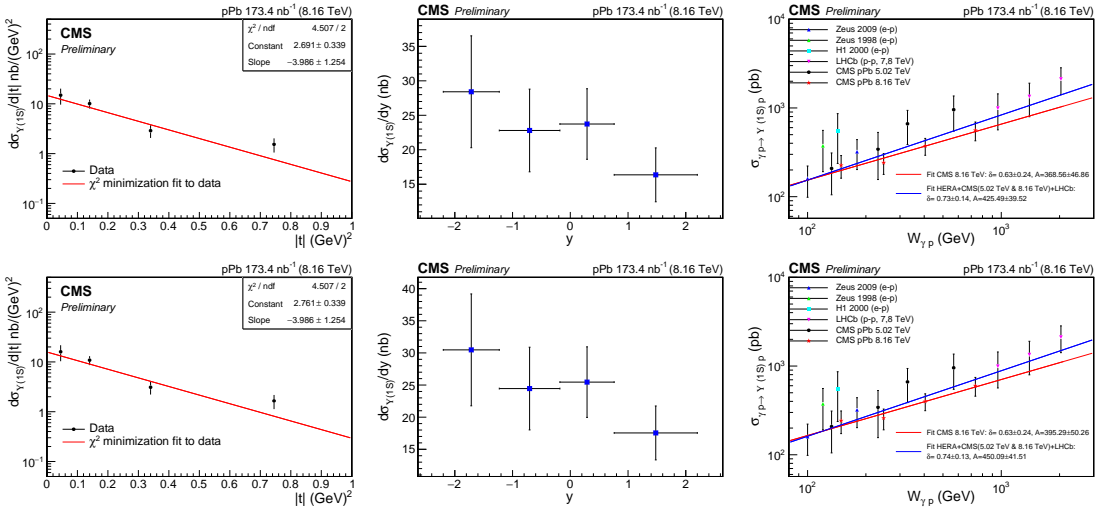


Figure 3: Differential cross-sections of $\Upsilon(1S)$ as a function of $|t|$ and y are shown in the left and the middle figure, respectively. The right figure shows the total cross-section of $\Upsilon(1S)$ as a function of $W_{\gamma p}$. The upper panel shows the cross-section corresponding to the +3.5% change of luminosity. Similarly, the lower panel shows the cross-section corresponding to the -3.5% change of luminosity. These plots are made to estimate systematic contributions corresponding to the luminosity.

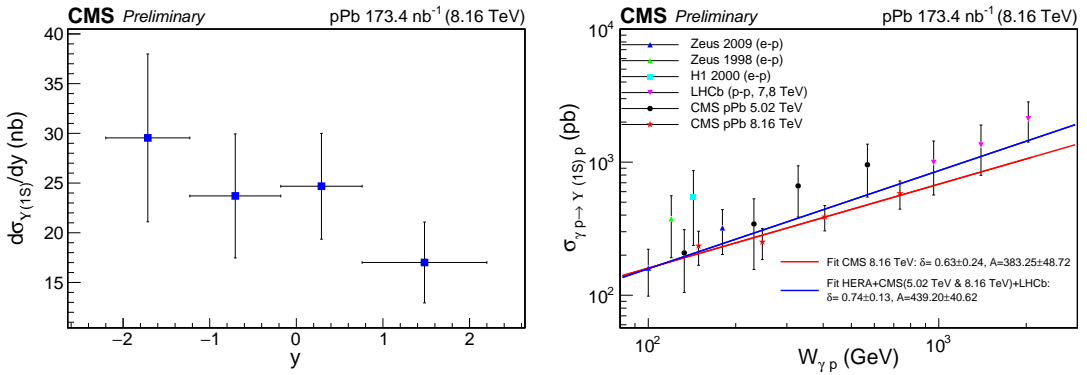


Figure 4: A differential cross-section of $\Upsilon(1S)$ as a function of y is shown left figure. The right figure shows the total cross-section of $\Upsilon(1S)$ as a function of $W_{\gamma p}$. These plots are made to estimate systematic contribution corresponding to the feed-down.

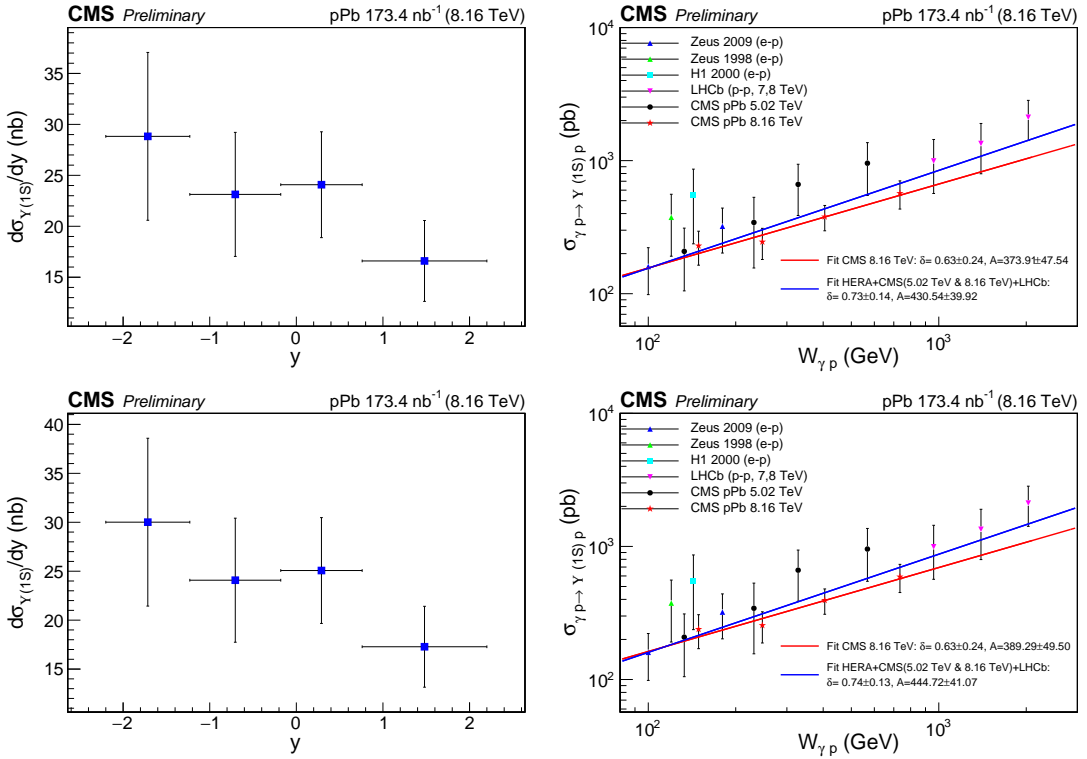


Figure 5: The differential cross-section of $\Upsilon(1S)$ as a function of y is shown in the left figure. The right figure shows the total cross-section of $\Upsilon(1S)$ as a function of $W_{\gamma p}$. The upper panel shows the cross-section corresponding to the $+0.05\%$ change of the BR fraction taken from PDG. Similarly, the lower panel shows the cross-section corresponding to the -0.05% change of the BR fraction.

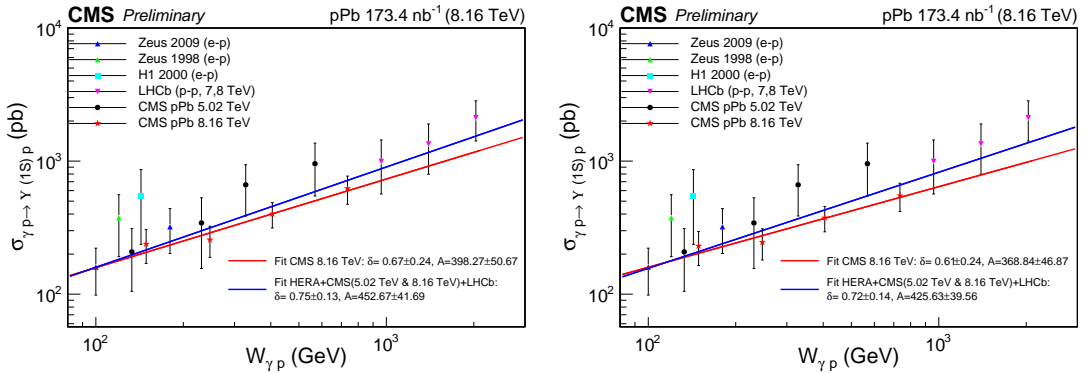


Figure 6: These figures show the total cross-section of $\Upsilon(1S)$ as a function of $W_{\gamma p}$. The left figure shows the cross-section corresponding to the $+5\%$ change of the lead ion radius in the STARLIGHT MC sample. Similarly, the right figure shows the cross-section corresponding to the -5% change of the lead ion radius.

Bibliography

- [1] A. Purcell. “Go on a particle quest at the first CERN webfest. Le premier webfest du CERN se lance à la conquête des particules” (Aug. 2012), p. 10.
- [2] H. Yukawa. “On the interaction of elementary particles. I”. *Proceedings of the Physico-Mathematical Society of Japan. 3rd Series* 17 (1935), pp. 48–57.
- [3] M. Gell-Mann. “A schematic model of baryons and mesons”. *Physics Letters* 8.3 (1964), pp. 214–215.
- [4] G. Zweig. “An SU _3 model for strong interaction symmetry and its breaking”. *CERN Report CM-P00042884* (1964).
- [5] S. W. Herb et al. “Observation of a Dimuon Resonance at 9.5-GeV in 400-GeV Proton-Nucleus Collisions”. *Phys. Rev. Lett.* 39 (1977), pp. 252–255.
- [6] M. Thomson. *Modern particle physics*. New York: Cambridge University Press, 2013.
- [7] F. Englert and R. Brout. “Broken Symmetry and the Mass of Gauge Vector Mesons”. *Phys. Rev. Lett.* 13 (1964). Ed. by J. C. Taylor, pp. 321–323.
- [8] P. W. Higgs. “Broken Symmetries and the Masses of Gauge Bosons”. *Phys. Rev. Lett.* 13 (1964). Ed. by J. C. Taylor, pp. 508–509.
- [9] S. Chatrchyan et al. “Observation of a New Boson at a Mass of 125 GeV with the CMS Experiment at the LHC”. *Phys. Lett. B* 716 (2012), pp. 30–61. arXiv: [1207.7235](https://arxiv.org/abs/1207.7235) [hep-ex].

- [10] G. Aad et al. “Observation of a new particle in the search for the Standard Model Higgs boson with the ATLAS detector at the LHC”. *Phys. Lett. B* 716 (2012), pp. 1–29. arXiv: [1207.7214 \[hep-ex\]](#).
- [11] S. Mele. “Measurements of the running of the electromagnetic coupling at LEP”. *26th International Symposium on Physics in Collision (PIC 2006)*. Oct. 2006. arXiv: [hep-ex/0610037](#).
- [12] S. Bethke. “Experimental tests of asymptotic freedom”. *Prog. Part. Nucl. Phys.* 58 (2007), pp. 351–386. arXiv: [hep-ex/0606035](#).
- [13] R. Misra and S. Ahmad. “Gauge unification of fundamental forces: The story of success” (1993).
- [14] L. Kumar and D. Keane. “Experimental studies of the quantum chromodynamics phase diagram at the STAR experiment”. *Pramana* 84.5 (2015), pp. 773–786.
- [15] S. Chatrchyan et al. “Exclusive photon-photon production of muon pairs in proton-proton collisions at $\sqrt{s} = 7$ TeV”. *JHEP* 1201 (2012), p. 052. arXiv: [1111.5536 \[hep-ex\]](#).
- [16] B. I. Abelev et al. “Azimuthal Charged-Particle Correlations and Possible Local Strong Parity Violation”. *Phys. Rev. Lett.* 103 (2009), p. 251601. arXiv: [0909.1739 \[nucl-ex\]](#).
- [17] P. Foka and M. A. Janik. “An overview of experimental results from ultra-relativistic heavy-ion collisions at the CERN LHC: Hard probes”. *Reviews in Physics* 1 (2016), pp. 172–194.
- [18] J. C. Collins, D. E. Soper, and G. F. Sterman. “Factorization of Hard Processes in QCD”. *Adv. Ser. Direct. High Energy Phys.* 5 (1989), pp. 1–91. arXiv: [hep-ph/0409313](#).
- [19] D. M. South and M. Turcato. “Review of Searches for Rare Processes and Physics Beyond the Standard Model at HERA”. *Eur. Phys. J. C* 76.6 (2016), p. 336. arXiv: [1605.03459 \[hep-ex\]](#).
- [20] A. J. Baltz et al. “The Physics of Ultraperipheral Collisions at the LHC”. *Phys. Rep.* 458 (2008), p. 1. arXiv: [0706.3356 \[nucl-ex\]](#).
- [21] D. J. Griffiths. *Introduction to electrodynamics*. American Association of Physics Teachers, 2005.

- [22] S. R. Klein et al. “STARlight: A Monte Carlo simulation program for ultra-peripheral collisions of relativistic ions”. *Comput. Phys. Commun.* 212 (2017), pp. 258–268. arXiv: [1607.03838 \[hep-ph\]](#).
- [23] S. Klein and J. Nystrand. “Exclusive vector meson production in relativistic heavy ion collisions”. *Phys. Rev.* C60 (1999), p. 014903. arXiv: [hep-ph/9902259 \[hep-ph\]](#).
- [24] D. d’Enterria. “Quarkonia photoproduction at nucleus colliders”. *Nucl. Phys. Proc. Suppl.* 184 (2008), pp. 158–162. arXiv: [0711.1123 \[nucl-ex\]](#).
- [25] C. A. Salgado et al. “Proton-Nucleus Collisions at the LHC: Scientific Opportunities and Requirements”. *J. Phys.* G39 (2012), p. 015010. arXiv: [1105.3919 \[hep-ph\]](#).
- [26] L. L. Frankfurt, A. Freund, and M. Strikman. “Diffractive exclusive photoproduction in DIS at HERA”. *Phys. Rev.* D58 (1998). [Erratum: *Phys. Rev.* D59 (1999) 119901], p. 114001. arXiv: [hep-ph/9710356 \[hep-ph\]](#).
- [27] L. Frankfurt, M. McDermott, and M. Strikman. “A Fresh look at diffractive J/ψ photoproduction at HERA, with predictions for THERA”. *JHEP* 03 (2001), p. 045. arXiv: [hep-ph/0009086 \[hep-ph\]](#).
- [28] A. D. Martin et al. “Small x gluon from exclusive J/ψ production”. *Phys. Lett. B* 662 (2008), p. 252. arXiv: [0709.4406 \[hep-ph\]](#).
- [29] P. Jones et al. “Probes of the small x gluon via exclusive J/ψ and Υ production at HERA and LHC”. *JHEP* 11 (2013), p. 085. arXiv: [1307.7099 \[hep-ph\]](#).
- [30] A. Adeluyi, C. A. Bertulani, and M. J. Murray. “Nuclear effects in photoproduction of heavy quarks and vector mesons in ultraperipheral PbPb and pPb collisions at the LHC”. *Phys. Rev. C* 86 (2012), p. 047901. arXiv: [1208.6258 \[nucl-th\]](#).
- [31] A. Adeluyi and T. Nguyen. “Coherent photoproduction of ψ and Υ mesons in ultraperipheral pPb and PbPb collisions at the CERN LHC”. *Phys. Rev. C* 87 (2013), p. 027901. arXiv: [1302.4288 \[nucl-th\]](#).
- [32] V. Guzey and M. Zhalov. “Exclusive J/ψ production in ultraperipheral collisions at the LHC: constrains on the gluon distributions in the proton and nuclei”. *JHEP* 10 (2013), p. 207. arXiv: [1307.4526 \[hep-ph\]](#).

- [33] V. Guzey et al. “Evidence for nuclear gluon shadowing from the ALICE measurements of PbPb ultraperipheral exclusive J/ψ production”. *Phys. Lett. B* 726 (2013), p. 290. arXiv: [1307.1754 \[hep-ph\]](#).
- [34] G. Sampaio dos Santos and M. V. T. Machado. “Exclusive photoproduction of quarkonium in proton-nucleus collisions at the CERN Large Hadron Collider”. *Phys. Rev. C* 89 (2014), p. 025201. arXiv: [1312.0770 \[hep-ph\]](#).
- [35] G. Sampaio dos Santos and M. V. T. Machado. “On theoretical uncertainty of color dipole phenomenology in the J/ψ and Υ photoproduction in pA and AA collisions at the CERN Large Hadron Collider”. *J. Phys. G* 42 (2015), p. 105001. arXiv: [1411.7918 \[hep-ph\]](#).
- [36] T. Lappi and H. Mantysaari. “Incoherent diffractive J/ψ production in high energy nuclear DIS”. *Phys. Rev. C* 83 (2011), p. 065202. arXiv: [1011.1988 \[hep-ph\]](#).
- [37] T. Lappi and H. Mantysaari. “ J/ψ production in ultraperipheral Pb+Pb and p+Pb collisions at energies available at the CERN Large Hadron Collider”. *Phys. Rev. C* 87 (2013), p. 032201. arXiv: [1301.4095 \[hep-ph\]](#).
- [38] V. P. Goncalves, B. D. Moreira, and F. S. Navarra. “Exclusive heavy vector meson photoproduction in hadronic collisions at LHC: predictions of the Color Glass Condensate model for Run 2 energies”. *Phys. Rev. D* 95 (2017), p. 054011. arXiv: [1612.06254 \[hep-ph\]](#).
- [39] S. Chekanov et al. “Measurement of Elastic Υ Photoproduction at HERA”. *Phys. Lett. B* 437 (1998), p. 432. eprint: [hep-ex/9807020](#) (hep-ex).
- [40] A. Atkas et al. “Elastic photoproduction of J/ψ and Υ mesons at HERA”. *Phys. Lett. B* 483 (2000), p. 23. arXiv: [hep-ex/0003020 \[hep-ex\]](#).
- [41] S. Chekanov et al. “Exclusive photoproduction of Υ mesons at HERA”. *Phys. Lett. B* 680 (2009), p. 4. arXiv: [0903.4205 \[hep-ex\]](#).
- [42] S. Chekanov et al. “Measurement of the t dependence in exclusive photoproduction of $\Upsilon(1S)$ mesons at HERA”. *Phys. Lett. B* 708 (2012), p. 14. arXiv: [1111.2133 \[hep-ex\]](#).
- [43] R. Aaij et al. “Exclusive J/ψ and $\psi(2S)$ production in pp collisions at $\sqrt{s} = 7$ TeV”. *J. Phys. G* 40 (2013), p. 045001. arXiv: [1301.7084 \[hep-ex\]](#).
- [44] R. Aaij et al. “Measurement of the exclusive Υ production cross section in pp collisions at $\sqrt{s} = 7$ TeV and 8 TeV”. *JHEP* 09 (2015), p. 084. arXiv: [1505.08139 \[hep-ex\]](#).

- [45] A. M. Sirunyan et al. “Measurement of exclusive Υ photoproduction from protons in pPb collisions at $\sqrt{s_{\text{NN}}} = 5.02$ TeV”. *Eur. Phys. J. C* 79.3 (2019), p. 277. arXiv: [1809.11080 \[hep-ex\]](#).
- [46] S. J. Brodsky et al. “The QCD pomeron with optimal renormalization”. *JETP* 70 (1999), p. 155. arXiv: [hep-ph/9901229 \[hep-ph\]](#).
- [47] S. P. Jones et al. “Predictions of exclusive $\psi(2S)$ production at the LHC”. *J. Phys. G* 41 (2014), p. 055009. arXiv: [1312.6795 \[hep-ph\]](#).
- [48] V. Guzey and M. Zhalov. “Exclusive J/ψ production in ultraperipheral collisions at the LHC: constraints on the gluon distributions in the proton and nuclei”. *JHEP* 10 (2013), p. 207. arXiv: [1307.4526 \[hep-ph\]](#).
- [49] L. V. Gribov, E. M. Levin, and M. G. Ryskin. “Semihard Processes in QCD”. *Phys. Rept.* 100 (1983), p. 1.
- [50] A. H. Mueller and J.-W. Qiu. “Gluon Recombination and Shadowing at Small Values of x ”. *Nucl. Phys. B* 268 (1986), p. 427.
- [51] L. D. McLerran and R. Venugopalan. “Gluon distribution functions for very large nuclei at small transverse momentum”. *Phys. Rev. D* 49 (1994), p. 3552.
- [52] B. Z. Kopeliovich et al. “Nonperturbative Gluon Radiation and Energy Dependence of Elastic Scattering”. *Phys. Rev. Lett.* 85 (3 July 2000), pp. 507–510.
- [53] W. R. Leo. *Techniques for nuclear and particle physics experiments: a how-to approach; 2nd ed.* Berlin: Springer, 1994.
- [54] H. Bethe. “Theory of the Passage of Fast Corpuscular Rays Through Matter”. *Annalen Phys.* 5 (1930), pp. 325–400.
- [55] S. M. Erina. “Charging-up Behaviour of MicroPattern Gaseous Detectors”. PhD thesis. Nov. 2020.
- [56] B. R. Martin and G. Shaw. *Particle physics*. 2008.
- [57] G. Charpak and F. Sauli. “MULTIWIRE PROPORTIONAL CHAMBERS AND DRIFT CHAMBERS”. *Nucl. Instrum. Meth.* 162 (1979), pp. 405–428.
- [58] A. Oed. “Position Sensitive Detector with Microstrip Anode for electron Multiplication with Gases”. *Nucl. Instrum. Meth. A* 263 (1988). Ed. by A. Smith, pp. 351–359.

- [59] F. Sauli. “The gas electron multiplier (GEM): Operating principles and applications”. *Nucl. Instrum. Meth. A* 805 (2016), pp. 2–24.
- [60] C. Grupen and I. Buvat, eds. *Handbook of particle detection and imaging, vol. 1 and vol.2*. Berlin, Germany: Springer, 2012.
- [61] R. Assmann, M. Lamont, and S. Myers. “A brief history of the LEP collider”. *Nucl. Phys. B Proc. Suppl.* 109 (2002). Ed. by F. L. Navarria, M. Paganoni, and P. G. Pelfer, pp. 17–31.
- [62] M. Tanabashi et al. “Review of Particle Physics”. *Phys. Rev. D* 98.3 (2018), p. 030001.
- [63] T. Sakuma. “Cutaway diagrams of CMS detector” (May 2019).
- [64] S. Chatrchyan et al. “Performance of the CMS drift-tube chamber local trigger with cosmic rays”. *JINST* 5 (Nov. 2009), T03003. 31 p. arXiv: [0911.4893](#).
- [65] S. Chatrchyan et al. “The CMS Experiment at the CERN LHC”. *JINST* 3 (2008), S08004.
- [66] M. S. Kim. “CMS reconstruction improvement for the muon tracking by the RPC chambers”. *PoS RPC2012* (Sept. 2012). Presented by Minsuk Kim at the XI workshop on Resistive Plate Chambers and Related Detectors - RPC2012, INFN Laboratori Nazionali di Frascati Italy, February 5-10, 2012, 045. 9 p. arXiv: [1209.2646](#).
- [67] V. Khachatryan et al. “The very forward CASTOR calorimeter of the CMS experiment”. *JINST* 16.02 (2021), P02010. arXiv: [2011.01185 \[physics.ins-det\]](#).
- [68] V. Khachatryan et al. “The CMS trigger system”. *JINST* 12.01 (2017), P01020. arXiv: [1609.02366 \[physics.ins-det\]](#).
- [69] S. R. Klein and J. Nystrand. “Photoproduction of quarkonium in proton proton and nucleus nucleus collisions”. *Phys. Rev. Lett.* 92 (2004), p. 142003. arXiv: [hep-ex/0311164 \[hep-ph\]](#).
- [70] J. Nystrand. “Photons and Exclusive Processes at Hadron Colliders” (). arXiv: [1001.4746 \[hep-ph\]](#).
- [71] C. F. v. Weizsäcker. “Radiation emitted in collisions of very fast electrons”. *Z.Phys.* 88 (1934), p. 612.
- [72] E. J. Williams. “Nature of the high-energy particles of penetrating radiation and status of ionization and radiation formulae”. *Phys. Rev.* 45 (1934), p. 729.

- [73] GEANT4 Collaboration. “GEANT4: A simulation toolkit”. *Nucl. Instrum. Meth. A* 506 (2003), p. 250.
- [74] N. Adam et al. “Generic tag and probe tool for measuring efficiency at cms with early data”. 111 (2009), p. 2009.
- [75] T. C. collaboration. “Performance of CMS muon reconstruction in pp collision events at $\sqrt{s} = 7 \text{ TeV}$ ”. *Journal of Instrumentation* 7.10 (Oct. 2012), P10002–P10002.
- [76] “Search for elliptic azimuthal anisotropies in γp interactions within ultra-peripheral pPb collisions at $\sqrt{s_{NN}} = 8.16 \text{ TeV}$ ” (2020).
- [77] T. Skwarnicki. “A study of the radiative CASCADE transitions between the Upsilon-Prime and Upsilon resonances” (1986).
- [78] W. Verkerke and D. P. Kirkby. “The RooFit toolkit for data modeling”. *eConf* C0303241 (2003), MOLT007. arXiv: [physics/0306116 \[physics\]](#).
- [79] C. Patrignani et al. “Review of Particle Physics”. *Chin. Phys. C* 40.10 (2016), p. 100001.
- [80] B. B. Abelev et al. “Exclusive J/ψ photoproduction off protons in ultra-peripheral p-Pb collisions at $\sqrt{s_{NN}} = 5.02 \text{ TeV}$ ”. *Phys. Rev. Lett.* 113 (2014), p. 232504. arXiv: [1406.7819 \[nucl-ex\]](#).
- [81] B. Ablev et al. “Coherent J/ψ photoproduction in ultra-peripheral Pb-Pb collisions at $\sqrt{s_{NN}} = 2.76 \text{ TeV}$ ”. *Phys. Lett. B* 718 (2013), p. 1273. arXiv: [1209.3715 \[nucl-ex\]](#).
- [82] E. Abbas et al. “Charmonium and e^+e^- pair photoproduction at mid-rapidity in ultra-peripheral Pb-Pb collisions at $\sqrt{s_{NN}} = 2.76 \text{ TeV}$ ”. *Eur. Phys. J. C* 73 (2013), p. 2617. arXiv: [1305.1467 \[nucl-ex\]](#).
- [83] R. J. Barlow and C. Beeston. “Fitting using finite Monte Carlo samples”. *Comput. Phys. Commun.* 77 (1993), pp. 219–228.
- [84] A. J. Schramm and D. H. Reeves. “Production of η mesons in double pomeron exchange”. *Phys. Rev. D* 55 (1997), p. 7312. arXiv: [hep-ph/961130 \[hep-ph\]](#).
- [85] L. A. Harland-Lang et al. “Standard candle central exclusive processes at the Tevatron and LHC”. *Eur. Phys. J. C* 69 (2010), p. 179. arXiv: [1005.0695 \[hep-ph\]](#).
- [86] C. Loizides, J. Kamin, and D. d’Enterria. “Improved Monte Carlo Glauber predictions at present and future nuclear colliders”. *Phys. Rev. C* 97.5 (2018). [Erratum: *Phys. Rev. C* 99, 019901 (2019)], p. 054910. arXiv: [1710.07098 \[nucl-ex\]](#).

- [87] “CMS luminosity measurement using 2016 proton-nucleus collisions at nucleon-nucleon center-of-mass energy of 8.16 TeV” (2018).
- [88] G. D. Lafferty and T. R. Wyatt. “Where to stick your data points: The treatment of measurements within wide bins”. *Nucl. Instrum. Meth. A* 355 (1995), pp. 541–547.
- [89] G. Sampaio dos Santos and M. V. T. Machado. “On theoretical uncertainty of color dipole phenomenology in the J/ψ and Υ photoproduction in pA and AA collisions at the CERN Large Hadron Collider”. *J. Phys. G* 42.10 (2015), p. 105001. arXiv: [1411.7918](https://arxiv.org/abs/1411.7918) [hep-ph].

List of Publications

- [1] K. Naskar. “Measurement of exclusive Upsilon photoproduction in pPb collisions at $\sqrt{s_{NN}} = 5.02$ TeV with the CMS”. *PoS HardProbes2018* (2019). Ed. by D. d’Enterria, A. Morsch, and P. Crochet, p. 180. arXiv: [1903.10811 \[hep-ex\]](https://arxiv.org/abs/1903.10811).
- [2] K. Naskar, D. Dutta, and P. Sarin. “Background study of Upsilon photoproduction in pPb collisions at 8.16 TeV with CMS experiment”. *DAE Symp. Nucl. Phys.* 63 (2018), pp. 958–959.
- [3] D. Dutta et al. “Study of Upsilon photoproduction in pPb collisions at 8.16 TeV with CMS experiment”. *DAE Symp. Nucl. Phys.* 62 (2017), pp. 964–965.

Acknowledgments

It has been a wonderful journey at IIT Bombay which comes at its end. I am always thankful to some people who directly and indirectly helped me during this journey. In this platform, I would like to acknowledge them.

First of all, I want to express my sincere gratitude to my co-guide **Prof. Dipanwita Dutta** (from BARC), for her valuable suggestions during the completion of this work. Without her support and guidance the work could not be performed at all.

I would like to express my deep gratitude to my guide **Prof. Pradeep Sarin**, for his valuable guidance, support & involvement throughout my research work. Due to his friendly nature I could discuss any of my problems with him and he was always there to help me.

I also thank my research progress committee members **Prof. S Uma Sankar** and **Prof. Vikram Rentala** for examining my research work progress regularly. Their comments, advice and suggestions were very helpful to improve this work. I would like to thank to my collaborators **Prof. Robert Ciesielski** (The Rockefeller University), **Prof. Kajari Mazumdar** (TIFR) for useful discussions during work.

Thanks to all my friends during PhD who made a enjoyable stay at IITB. Last but not least, I thank my parents and my all family members for their love and support.